ANALYSIS OF CONNECTIVITY BETWEEN LOCAL MULTI-VARIATE PATTERNS OF FUNCTIONAL MRI DATA

Dissertation
zur Erlangung des Doktorgrades
der Naturwissenschaften (Dr. rer. nat.)
der Fakultät für Physik
der Universität Regensburg

vorgelegt von
Volker Fischer
aus Regensburg

Januar 2011

Promotionsgesuch eingereicht am: 17.01.2011

Die Arbeit wurde durchgeführt am Institut für Biophysik und physikalische Biochemie unter Anleitung von Prof. Dr. Elmar W. Lang in Zusammenarbeit mit dem Institut für Experimentelle Psychologie unter Betreuung von Prof. Dr. Mark W. Greenlee.

Prüfungsausschuss:

Vorsitzender: Prof. Dr. Andreas Schäfer
1. Gutachter: Prof. Dr. Elmar W. Lang
2. Gutachter: Prof. Dr. Mark W. Greenlee
3. Gutachter: Prof. Dr. Josef Zweck

Acknowledgments

This dissertation would not have been possible without the guidance and the help of several individuals contributing their assistance in the preparation and completion of this thesis. First and foremost, my utmost gratitude to my supervisors Prof. Dr. Mark W. Greenlee and Prof. Dr. Elmar W. Lang. I will never forget their continuous support and encouragement to make this thesis possible. Especially I thank Prof. Dr. Mark W. Greenlee for offering me the opportunity to work with functional magnetic resonance imaging, his guidance concerning neuroscientific issues, and the financial support with which he and the Federal Ministry of Education and Research supported this project.

I owe my deepest gratitude to Dr. Ingo Keck and Dr. Anton Beer who, during countless conversations, inspired many aspects of this thesis with their ideas and knowledge.

My colleagues, Dipl.-Psych. Markus Raabe and Dr. Ference Acs, I would like to thank for their patient guidance during my first steps with functional magnetic resonance imaging and Markus Raabe especially for his help with data aquisition and providing paradigm stimuli.

I would like to thank Mariella Strehl, Maressa McConkey, and Helmut Nebl for reviewing this script and searching for the last missing comma.

I am also indebted to the numerous contributors to the "Open Source" programming community for providing the countless toolboxes and systems I have used to produce both my results and this thesis.

Last but not the least, I thank my family and friends for their moral support throughout all my studies.

Volker Fischer

Contents

1 Introduction

"Brain: an apparatus with which I think I think."
Ambrose Bierce (1842 - 1914), The Devil's Dictionary

The human brain, with its approximately 100 billion neurons and 10.000 synaptic connections per neuron [119], is known to be the central controlling organ of the human body. Studying the brain has led to numerous findings concerning important concepts, such as free will (e.g. [63] [145] [165]) and consciousness (for example [92] [61] among many more).

Many studies in the fields of medicine, biology, and psychology have demonstrated that our brain can be divided into functionally segregated regions with different specialization. In the visual domain, for example, signals originating from the retina of the eye accumulate in the primary visual cortex located at the posterior end of the brain. Information is then passed to higher areas concerned with integration and evaluation. Depending on its content the original signal can cause responses and actions governed e.g. by the motor cortex.

Information processing in different brain areas heavily relies on their interconnections and the properties of these connections. Understanding how brain areas are connected does not only lead to a deeper knowledge of how such complex human behavior arise, but can also be used to diagnose neuronal disorders and injuries [3] [149]. Investigating neuronal connectivity between brain areas has therefore become a very important interdisciplinary field of neuroscience.

Aim of this thesis is to introduce, illustrate, and discuss a new way of investigating connections between brain areas using non-invasive imaging techniques.

During the last century, many innovations in medicine, chemistry, and physics allowed a deeper insight into organization and functionality of the brain. One of the newest of these methods is functional magnetic resonance imaging (fMRI), which, compared to other techniques, achieves a high spatial resolution of about $1\,\mathrm{mm}^3$. Fig. 1.1 shows two images of the human brain obtained with MR imaging techniques.

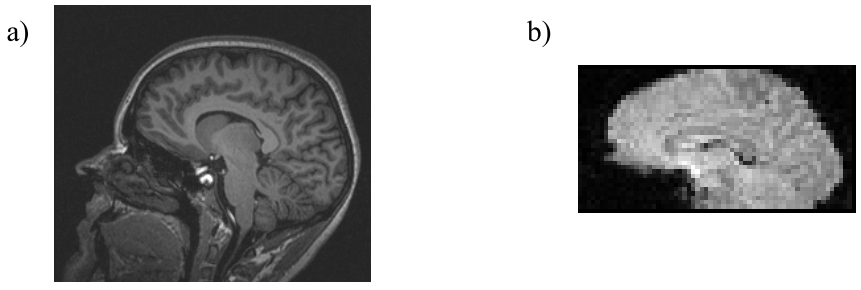

Figure 1.1: Different views of the human brain showing a) an anatomical T_1-weighted MR image, b) a functional $T_2^\star$-weighted MR image (for details about T_1- and $T_2^\star$-weighted images please see section 2.1.1).

Due to its physical nature, fMRI does not measure neuronal activity directly, but only indirectly changes in the local oxygen concentration also called blood-

oxygen-level-dependent response or short the BOLD response, which is caused by neuronal activation. In a typical fMRI experiment, neural correlates of a given task are evaluated by comparing associated activations and/or deactivations with those elicited by a control task.

FMRI has been used to study connectivity between brain areas. Accordingly the temporal behavior of a brain area is represented by the first principal component analysis (PCA) component of this region. This component is the time course that explains most variance of the region's behavior. At present, this approach is the standard way of extracting temporal information from a brain region [46] [49] [144] [172]. During the last few years, some approaches have been developed to study connectivity between brain areas on the basis of these time series and yielded important insights, for example, into pathological patterns of prodromal psychosis [3], schizophrenia [149], and aging [134].

Its high spatial resolution makes fMRI data also accessible to advanced statistical approaches to data analysis, such as support vector machines (SVM), which were developed in other research fields. Application of these techniques led to important insights, such as, for example, about conscious and unconscious perception of stimuli (e.g. [60] [61]). These methods take advantage of the fact that during different tasks and stimuli, voxels (3D equivalent of a pixel) inside an area related to the task or stimulus, form different spatial activation distributions (so-called multi-variate or multi-voxel patterns (MVP)).

The key idea of this thesis is to replace the state of the art representation of a brain region's temporal behavior by its first PCA component with time series associated to multi-variate patterns of a region. In the state of the art method each region is represented by only one time course, reflecting the area's overall (over all voxels of the area) activation. Now each region is represented by several time courses, each one associated with the activation of a multi-variate pattern of the area. Fig. 1.2 illustrates this idea.

To identify multi-voxel patterns and their activation courses, independent component analysis (ICA) was used to extract the patterns from regions of interest. The ICA decomposition identifies stochastically independent components underlying a region's activation. Those components might be associated to artifacts such as head motion, or represent the neuronally evoked patterns. After a suitable selection of independent components, which represent the patterns of interest for each region, existing connectivity analysis methods can be applied to these components. During my thesis, this concept is referred to as *pattern connectivity*, emphazising that connectivity between patterns instead of brain areas is analyzed.

Pattern connectivity states not only a generalization of the existing method, but also yields a more intuitive representation of brain regions and allows to map and study more complex behaviors of brain regions, making the information of multi-variate patterns of brain areas accessible to connectivity analysis techniques.

This thesis can be divided into two major parts. In chapter 2 existing concepts, which were important for this work, are briefly reviewed. Fundamental physics behind magnetic resonance imaging (MRI) and functional MRI, together with the used measurement protocol and preprocessing steps, are discussed in section 2.1.

Section 2.2 reviews existing connectivity analysis techniques for fMRI data and particularly describes the application of Pearson's correlation and dynamic causal modeling to study neuronal connectivity. Finally, multi-voxel pattern analysis and different matrix decompositions are described in section 2.3.

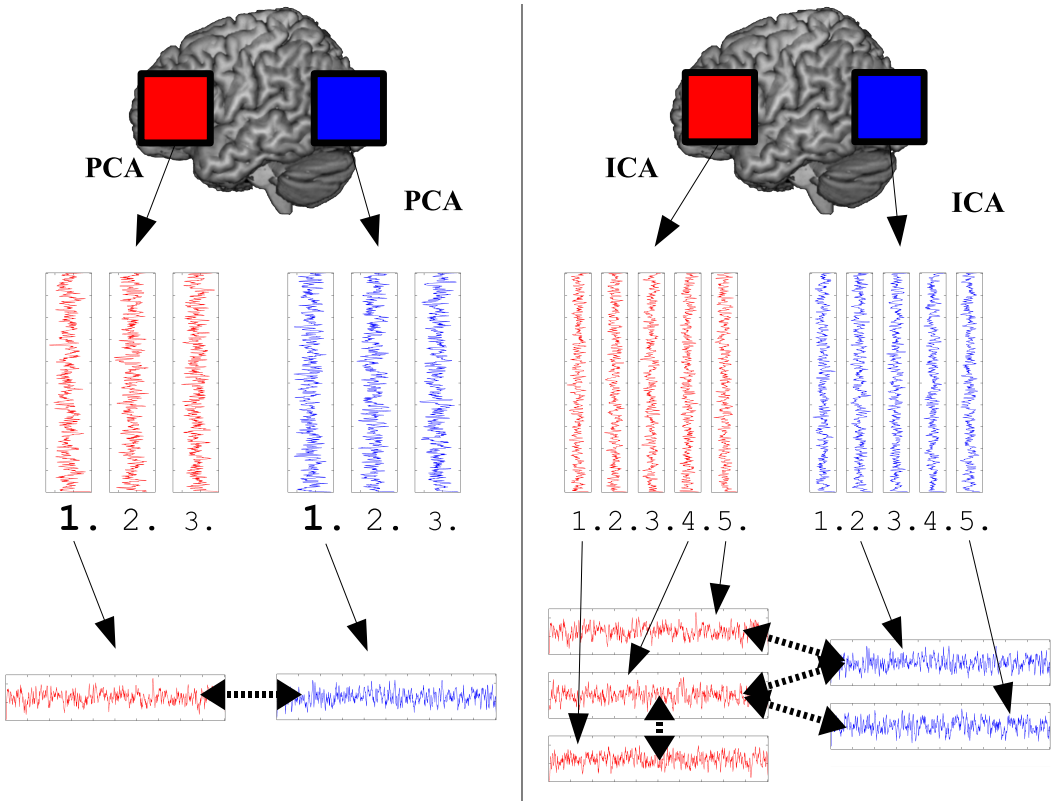

Figure 1.2: Standard method and key idea. (Left) Illustration of the standard method. The first component of a region's PCA decomposition is selected from each region for further analysis. (Right) Each region is decomposed into independent components. My key idea was to select paradigm-related components from these decompositions for further connectivity analysis and thereby enabling connectivity analysis between multi-variate patterns of fMRI data.

Chapter 3 introduces and illustrates the new concept of pattern connectivity. Firstly, the idea is described in greater detail in section 3.1 and problems arising with component selection are identified and solved. The analysis of two fMRI experiments and synthetic fMRI data illustrates the proposed method. The first experiment, which is described in section 3.2, aims to validate pattern connectivity by comparing it to the state of the art method. Here, a simple neuronal network containing two regions, each, in the scope of the experiment, representable with one time course, was chosen. In section 3.3, the second experiment in which the behavior of one of the regions can not be represented by a single time course is described. Hence, the state of the art method is not applicable for this experiment. Because the results of the second experiment, although they are very intuitive, can not be validated with the state of the art method, synthetic fMRI data was generated for which the underlying connectivity structure is known and can be compared to the one found with pattern connectivity. Aims of this second exper-

iment are to highlight advantages of pattern connectivity over the standard PCA method and to show that connectivity between multi-variate patterns of fMRI data can be analyzed.

It is not a goal of this thesis to actually reveal new insights in neuronal connectivity, but to introduce a new method, which has a great potential to lead to those insights in future applications. Thus the methodical point of view is emphasized. It is also not the aim of this work to introduce a new type of connectivity, but a new basis on which existing methods can be utilized.

The major goal of the present work is to show that, for fMRI data, it is possible to study neuronal connectivity between multi-voxel patterns instead of brain regions by providing, validating, and illustrating the new concept of pattern connectivity, and by identifying and solving problems arising with its implementation.

2 Methods

This chapter aims to give a schematic overview of the present state of science concerning neuronal connectivity studied on the basis of fMRI data and to briefly review already existing techniques and methods that are applied.

Firstly in chapter 2.1.1, a short introduction into the physical foundations of MRI data acquisition is given, followed by a more detailed discussion of the BOLD response, which is measured with functional MRI (chapter 2.1.2).

Chapter 2.2.1 gives a survey over the theory of neuronal connectivity, including an outline of the most important techniques used to study it. Section 2.2.2 descibes the sophisticated approach of dynamic causal modeling to analyse neuronal connectivity.

Furthermore the usage of multi-variate patterns is motivated by giving some of the most important examples from literature for the information MVPs hold and which can not be obtained by studying brain areas as a whole (chapter 2.3.1). Finally in chapters 2.3.4 and 2.3.5, a review of principal and independent component analysis together with the general linear model (PCA, ICA, and GLM) and their applications onto fMRI data is given.

2.1 Functional magnetic resonance imaging

In the last forty years, magnetic resonance imaging has become one of the most important medical imaging techniques. It delivers insights into the structure of almost every part of the human body (see 1.1a)) down to below $1\,\mathrm{mm}^3$ of spatial resolution without the exposure of participants to destructive radiation like X-ray tomography. During the last fifteen years, besides MRI, *functional* MRI yielded information about the structure and operational mode of the brain. MRI and functional MRI are the result of ongoing research in various fields, all the way from physics to chemistry to biology to medicine. MRI has its roots in the beginning of the 20th century, when quantum mechanics was discovered.

2.1.1 MRI physics

The foundations for MR imaging techniques were laid with the experimental discovery of the spin of electrons by Otto Stern and Walther Gerlach in 1922 [51], followed by the theoretical work of Wolfgang Pauli [115] [116] and Paul Dirac [36]. They showed that elementary particles or atoms possess an intrinsic quantum state similar to the angular momentum of classically spinning objects. This intrinsic angular momentum is called *spin* $\vec{I}$ and causes a magnetic moment $\vec{\mu}$ proportional to $\vec{I}$:

$$\vec{\mu} = \gamma \vec{I}, \tag{1}$$

where γ is the gyromagnetic ratio. The idea of MR techniques is to briefly stimulate the nuclear spins. After stimulation, the nuclei radiate the absorbed energy back until they reach equilibrium again. This property is called *nuclear magnetic resonance* (NMR) and was first described and tested by Isidor Rabi in

1938 [128] with molecular beams, and later independently generalized by Felix Bloch [14] and Edward Mills Purcell [126] onto liquids and solids.

The spin has a quantized size $I = \hbar\sqrt{s(s+1)}$, where $\hbar$ is the reduced Planck's constant and $s = 0, \frac{1}{2}, 1, 1\frac{1}{2}, \ldots$ the spin quantum number. For each particle type, the spin quantum number is fixed and cannot change. A proton has a spin $s = \frac{1}{2}$, a neutron $s = 0$, and an atomic nucleus $s = \frac{1}{2}$ if the number of protons in the nucleus is odd and $s = 0$ if it is even. From Form. 1 one sees that only nuclei with $s \neq 0$ result in a detectable magnetic moment. Therefore only atomic nuclei with an odd number of protons can be used for signal generation. The most important nuclei of this type are hydrogen ^{1}H and carbon-13 ^{13}C. Considering a small sample tissue, the contained nuclei with non-vanishing spin can be thought of as randomly aligned magnetic moments, so that the overall magnetic moment of the sample as sum of the single moments is zero.

Considering a static homogeneous magnetic field in z-direction $\vec{B}_0 = (0,\, 0,\, B_0)^t$, on the one hand this field exerts a torque $\vec{\mu} \times \vec{B}_0$, which leads to a precession of $\vec{\mu}$ around $\vec{B}_0$ with the so-called *Larmor frequency* ω_L:

$$\omega_L = -\gamma B_0 \tag{2}$$

On the other hand, for spins $s = \frac{1}{2}$, the field leads to a quantization of the spin orientation $I_z = \pm\frac{\hbar}{2}$. Those two states have different energy levels with $\Delta E = \hbar\gamma B_0$. Hence, changes between the two levels can be achieved by stimulation or emission of $\hbar\omega_L$. Due to local inhomogenities inside an ensemble of many nuclear spins, the actual Larmor frequency of a single nuclear spin varies slightly from ω_L.

According to the Bolzmann statistic, these two energy levels are not equally occupied. There are a few more up spins than down spins, which results in a small macroscopic longitudinal magnetization $\vec{M}_0 = (0,\, 0,\, M_0)^t$ of the sample in the direction of the magnetic field. For example, at room temperature and with a magnetic field of 1 T, there are only 6 ppm surplus up spins.

Using Ehrenfest's theorem [39], single spins can be integrated to macroscopic spin ensembles. Nuclear magnetization as a function of time for these ensembles is described by Bloch's equations [14].

To generate a measureable signal, nuclei are stimulated with an electro-magnetic, circularly polarized, radio frequency pulse (RF-pulse)

$$\vec{B}_1(t) = (B_1 \cos(\omega t),\, B_1 \sin(\omega t),\, 0), \tag{3}$$

which is transverse to the homogeneous magnetic field $\vec{B}_0$, lasting for a time τ. Due to the resonance condition, only nuclei with the Larmor frequency $\omega_L = \omega$ are resonant to the RF-pulse. So, by varying the frequency of the RF-pulse, different types of nuclei can be focused on. Together with the static field $\vec{B}_0$ the pulses sum up to a magnetic field $\vec{B}(t) = \vec{B}_0 + \vec{B}_1(t)$. Depending on the duration τ of the RF-pulse and its strength B_1, the macroscopic longitudinal magnetization is flipped about an angle α (called the *flip angle*) out of the z-direction into the xy-plane:

$$\alpha = \gamma B_1 \tau. \tag{4}$$

During and after the RF-pulse, nuclear spins perceive the field $\vec{B}_0$ and therefore

precess around the z-axis. For example, after a RF-pulse with $\alpha = 90°$, the longitudinal magnetization M_z is zero and one can measure a transverse magnetizion rotating around $\vec{B}_0$ with frequency ω_L, resulting from the phase-coherent spin ensembles. Because the RF-pulse has a limited duration, it contains not just one frequency, but a small frequency band [41] around ω and can therefore stimulate more nuclear spins with $\omega_L \approx \omega$.

When considering a spin ensemble, one must account for interactions between spins among themselves and with their environment, which lead to a relaxation of the magnetization after the RF-pulse. This causes different effects in the z-direction and the xy-plane.

Relaxation of the longitudinal magnetization $\vec{M}_0$ is caused by nuclei's energy, gained from the RF-pulse, dissipating into the surrounding lattice, and is called *spin-lattice* or *longitudinal relaxation*. Hence, the temperature of the ensemble is slightly increased. The decay of measurable transverse magnetization is called *free induction decay* (FID). In parallel, due to spin-spin interactions, the initial phase-coherent rotating spin ensembles dephase over time. This is called *spin-spin* or *transverse relaxation*.

Both relaxations are summarized by the Bloch equations [14], describing the macroscopic magnetization $\vec{M}$:

$$\frac{d}{dt}\vec{M}(t) = \gamma\vec{M}(t) \times \vec{B}(t) - \begin{pmatrix} M_x/T_2 \\ M_y/T_2 \\ (M_z - M_0)/T_1 \end{pmatrix}. \tag{5}$$

T_1 is called *longitudinal* or *spin-lattice relaxation time*, and is the time it takes after the RF-pulse for the longitudinal magnetization to recover about 63 % of its initial value: $M_z(t) = M_0(1 - \exp(-t/T_1))$. T_1 depends on field strength B_0 and investigated tissue. For example, due to its compact lattice, fat has a shorter T_1 than water (for detailed T_1 and T_2 relaxation times of brain tissue see e.g. [146]).

Analog T_2 is called *transverse* or *spin-spin relaxation time* and is the time after which the transverse signal has decreased to about 37 % of its initial value (after the RF-pulse). In addition to the spin-spin relaxation, random inhomogenities in the local magnetic susceptibility, for example, caused by the structure of the ensemble, evoke small random variations of the precession frequency of different spins, resulting in an additional loss of the initial phase coherence. The relaxation time of this process $T_{2,inh}$ together with T_2 gives the overall transverse relaxation time $T_2^\star$:

$$\frac{1}{T_2^\star} = \frac{1}{T_2} + \frac{1}{T_{2,inh}}. \tag{6}$$

It is always the case that: $T_2^\star < T_2 < T_1$.

In 1950 Erwin Hahn invented the technique of spin echos (SE), which allow measuring T_2 [57]. Thereby, after a time τ past an initial 90° RF-pulse, an 180° RF-pulse reverses the spins orientation and the same local inhomogenities that led to the dephasing of the spins lead to rephasing of the spins and to a measureable, so-called, *spin echo* after an echo time TE=2τ. In this way, one can estimate the spin-spin relaxation time T_2.

Another important echo-generating method is the gradient echo (GRE) [109].

Here, with an additional gradient magnetic field, dephasing of the spins is synthetically accelerated and after a short time the magnetic gradient is reversed, which results in a rephasing of spins and a gradient echo. Because the influence of local inhomogenities onto the spins is not inverted, the synthetic decay and rebuilding of the FID occurs during $T_2^\star$. This makes gradient echos a faster imaging technique than spin echos.

In general, one has vastly more complex pulse sequences or gradient sequences than those described for the spin or gradient echo. The time after which a pulse sequence can be repeated is called *repetition time* (TR). This time can be rather long (about a few seconds), because spins which are not entirely dephased can alter the adjacent sequence.

Besides the MR imaging technique described so far, other NMR based techniques such as, for example, NMR spectroscopy or Earth's magnetic field NMR are intensively used and under ongoing research.

Until 1973, NMR could only be used to derive information about a single point in space having no spatial resolution. In 1973 Paul C. Lauterbur [85] [86] produced the first 2-dimensional MR image (MRI) of two tubes filled with normal water, surrounded by heavy water, using a rotable magnetic gradient field. Under the supervision of Richard Ernst, Anil Kumar in 1975 published an approach using Fourier transformation to generate 3-dimensional scans [83]. One year later Sir Peter Mansfield introduced echo planar imaging (EPI), which allowed fast imaging [98] [97]. These discoveries led to Lauterbur and Mansfield receiving the Nobel prize in 2003.

These inventions led to the first MR scan of a human wrist by Hinshaw and colleagues in 1977 [69]. A more detailed description of the physical background behind MR techniques is given in [24] [55] [148].

2.1.2 Functional MRI and the BOLD signal

The most striking discovery on MRI is that differences in the metabolic state of the brain alter the local MR signal [109] [110], enabling an indirect measurement of neuronal activation. This technique is called *functional* MRI. The following description of a model of this effect is taken from [18] and simplified, omitting the role of cerebral blood volume (CBV) and the balloon model. The interested reader can refer to [19] [18] [96] for further details.

The basic processing unit of the human brain is the neuron [78]. With its axon each neuron forms up to 10.000 connections to other neurons. These connections are called *synapses*. For a diagram of a neuron and its connection to another neuron, see Fig. 2.1. Information between neurons is transmitted over the axon via a short-lasting rapid rise and fall of electrical membrane potential of the neuron called *action potential* [78]. This spike leads to chemical reactions causing the release of neurotransmitters into the synaptic cleft between the two neurons. These neurotransmitters have an inhibitory or excitatory effect on the target neuron.

As early as in 1890, Charles S. Roy and Charles S. Sherrington discovered that neuronal activity in the means of spiking neurons and the chemical information propagation over the synapses goes along with an alteration of blood flow and oxygenation level [135] - the so-called *hemodynamics* - in the human brain. Dur-

ing activation neurons and synapses gather energy, which they need, by consuming oxygen from hemoglobin. The rate, at which oxygen is consumed, is called *cerebral metabolic rate of oxygen* ($CMRO_2$). In this process oxygenated hemoglobin (oxyhemoglobin or oxyHb), which is diamagnetic [117] and isomagnetic with respect to the surrounding tissue, becomes deoxygenated hemoglobin (deoxyhemoglobin or desHb), which is paramagnetic (also to surrounding tissue) [117] (see Fig. 2.2).

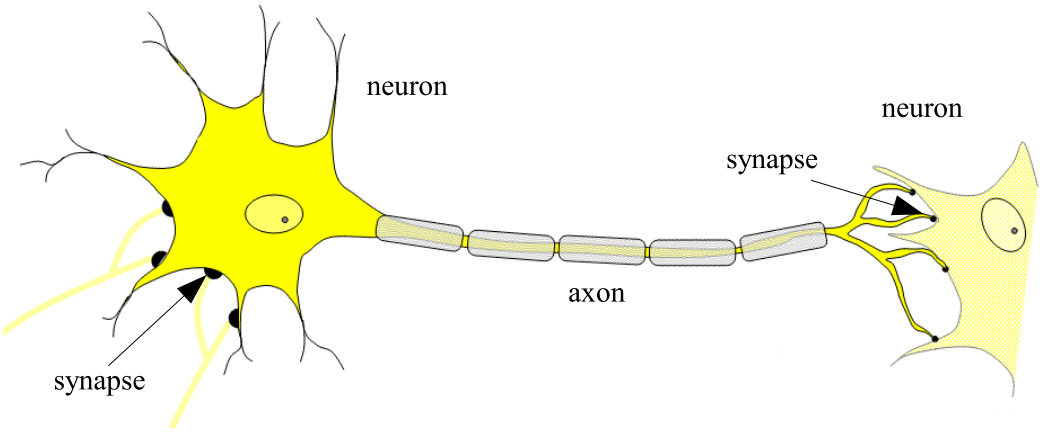

Figure 2.1: Schematic illustration of neurons and synapses. A neuron sends action potentials to other neurons over its axon. At the synapse this signal triggers chemical reactions which may lead to further activation and spiking of the target neuron (image taken and modified from http://de.wikipedia.org/wiki/Nervenzelle).

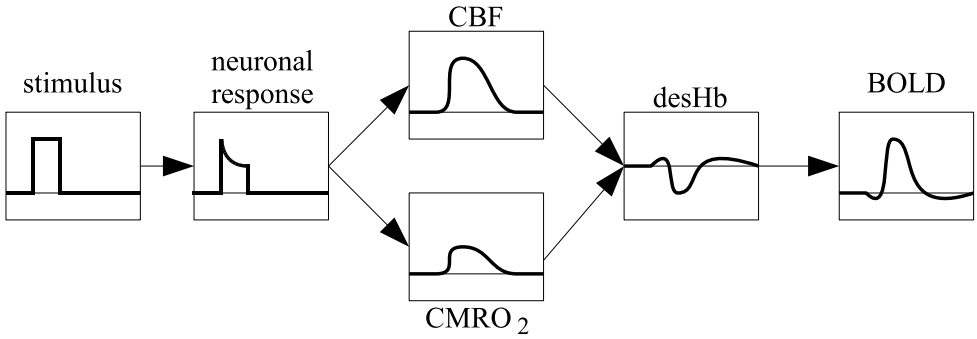

Figure 2.2: Simplified BOLD model. During the presentation of a stimulus (far left) neuronal activity rises in areas processing the stimulus (second from left). On the one hand this leads to an increase in oxygen consumption (lower center, $CMRO_2$), which would normally cause an increase of deoxygenated hemoglobin. On the other hand cerebral blood flow increases (upper center, CBF), which provides new oxygenated blood and thereby overall leads to an increase in oxygenated blood concentration, hence a decrease in deoxygenated hemoglobin concentration (second from the right). This reduced amount of paramagnetic deoxygenated hemoglobin leads to a measureable BOLD signal (far right).

Increased concentration of desoxygenated blood (desHb) would lead to a greater

local distortion of the external magnetic field through paramagnetic desHb resulting in a shorter spin-spin relaxation time T_2 and therefore shorter $T_2^\star$ [160]. But parallel to the increase of $CMRO_2$ the cerebral blood flow (CBF) also increases covering more than the actual oxygen consumption and therefore leading to an overall decrease in desHb concentration, which leads to a longer $T_2^\star$ relaxation time than during the resting state. This effect is called *blood-oxygen-level-dependent* or short *BOLD* effect. The measured signal due to the hemodynamic changes is called *hemodynamic response function* (HRF). As a measure of magnetic susceptibility the BOLD has no unit.

In 1990 Seiji Ogawa and colleagues first discovered the BOLD effect recognizing its importance for functional brain imaging [109] using gradient echos. The first fMRI study successfully measuring stimulus correlated signals was reported by John Belliveau and colleagues in 1991 [10] [84]. An example of a functional MR image is given in Fig. 1.1 b).

Since then, numerous fMRI studies have been published. However, the exact relation between neuronal activity and BOLD is still under active research (e.g. [6] [47] [94] [93]), and the difficulties and limitations arising using BOLD must be carefully accounted for.

Important properties (width, onset-delay, and time-to-peak) of the HRF vary over several parameters. BOLD studies showed intersubject and intersession variations for the shape of the HRF [101] [169] [1], implying one has to be careful with the comparison of subjects with each other and over sessions and the averaging of data. Furthermore, these parameters can vary between brain areas for one participant [136] [104] [89]. For two brain areas with similar neuronal activity but different HRF onset-delays, an interregional correlation measure depends largely on hemodynamic properties. This problem can be accounted for by using so called *block design* stimuli, which means that the stimuli are presented for a rather long time (above 8 s). This minimizes the effects of different HRF shapes. Another method is to model an individual HRF for each region of interest and correct further analyzing approaches with the estimated HRF parameters.

Despite this variability of the HRF's shape, a standardized HRF h gives an adequate approximation of the mostly unknown real HRF and has proven useful for many applications [50] (compare Fig. 2.3 left). In the present thesis the standardized hemodynamic response function provided by the SPM5 toolbox (Welcome Department of Imaging Neuroscience, London, UK) shown in Fig. 2.3 (far left) was used.

Another question, concerning the interpretation of found BOLD activation, is whether the energy consumption of spiking neurons, or of active synapses, causes the BOLD. Many studies regarding this topic have been carried out and the majority of them [4] [94] [93] [6] suggests synaptic activity and intracortical processing as the source of the BOLD response rather than the spiking rate [64] [65].

A major limitation to fMRI is its temporal resolution. On the one hand even with high magnetic fields a TR below 1 s can hardly be achieved without loss of spatial resolution and on the other hand the BOLD response itself is slow to reach its peak. This occurs about 6 s after neuronal activation [18] (compare Fig. 2.3) and makes it hard to distinguish BOLD responses of different events occurring within a short time window. FMRI paradigms must be designed accurately in

order to account for this effect.

There exist several other functional imaging techniques besides fMRI. However, all of these techniques either expose participants to radiation (e.g. positron emission tomography (PET) [158] [17] or single photon emission computed tomography (SPECT) [75]), or do not achieve the high spatial resolution of fMRI (e.g. electroencephalography (EEG) [125] or magnetoencephalography (MEG) [29]), which is necessary for multi-variate pattern analysis. That is why I used functional MRI.

A standard fMRI study consists of a paradigm lasting about half an hour, during which participants are stimulated (in most cases visually or auditorily) and perform certain tasks. Dependent on the MR scanner and measurement parameters, a 3-dimensional functional volume, covering the brain part which is of interest, is measured every TR seconds. On the basis of this functional data and the stimulus protocol, activated brain regions related to the stimulation can be identified and studied.

In general such a region of interest (ROI) can consists of any given subset of voxels. After the experiment a high resolution anatomical T_1-weighted scan is recorded for improved localization (e.g. for group analyzes) and visualization purposes.

Often, experimental conditions are compared to a so-called *baseline condition*, during which participants had no tasks to perform and perceived no stimulation.

For an fMRI experiment with $P \in \mathbb{N}$ experimental conditions, so-called *onset functions* $u_p : \mathbb{R}_0^+ \to \{0,1\}$, for $p = 1, ..., P$, can be defined for each condition. The first scan of the experiment is assumed to be measured at time $t = 0$. These functions contain information about whether, at a specific time $t \geq 0$, a stimulus is present $u_p(t) = 1$ or absent $u_p(t) = 0$, and build an important basis for further analysis. I will refer to the onset function of the baseline condition as u_B. This onset function has value 0 during stimulation or task periods and value 1 during rest periods. In general an onset function might also take values between 0 and 1 indicating, for example, the strength of a stimulus. In the scope of my thesis, this was not necessary, and therefore onset functions only took the values 0 or 1.

The convolution of an onset function u and the standard HRF h was often used and will from now on be referred to as the HRF onset function $\tilde{u} := h * u$, associated with the onset u (see Fig. 2.3).

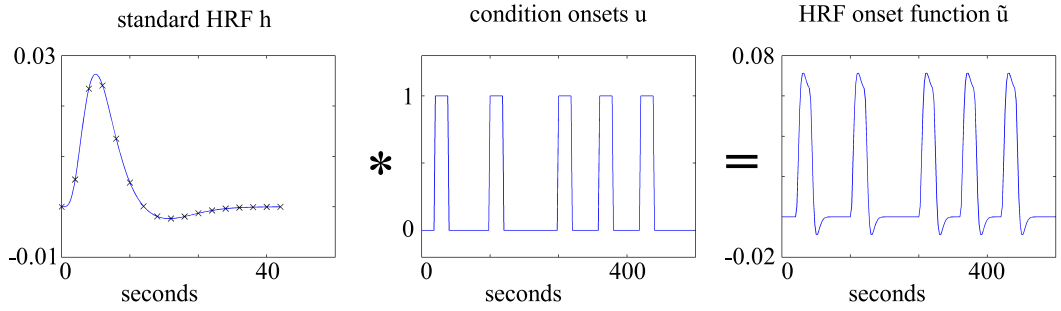

Figure 2.3: HRF onset functions. Convolution (right) of the standard HRF h (left) with an onset function u (middle) yield the HRF onset function $\tilde{u}$ associated with u. Crosses in the left graph mark measuring timepoints for TR = 2 s.

The operator $*$ here denotes the convolution of two continuous functions, both

set to 0 for $t < 0$:

$$(h * u)(t) := \int_{\mathbb{R}} h(\tau)u(t-\tau)\mathrm{d}\tau \tag{7}$$

For T measured scans, often the vector

$$\begin{pmatrix} (h*u)(0) \\ (h*u)(\mathrm{TR}) \\ (h*u)(2\ \mathrm{TR}) \\ \ldots \\ (h*u)(T\ \mathrm{TR}) \end{pmatrix} \in \mathbb{R}^T \tag{8}$$

is used which I also simply denote as $h * u$ or $\tilde{u}$.

2.1.3 Measurement protocol and preprocessing of fMRI data

Both conducted fMRI experiments used visual stimulation. As shown in Fig. 2.4, the visual stimuli were projected from a projector (JVC, DLA-G20, Yokohama, Japan, 75 Hz, 800 x 600 resolution) standing outside the magnetic field range of the scanner, onto a translucent circular screen (about $16.4° \times 21.7°$ of visual angle and 65 cm viewing distance) inside the scanner and were seen by the participants reflected in a mirror located a few centimeters above their heads.

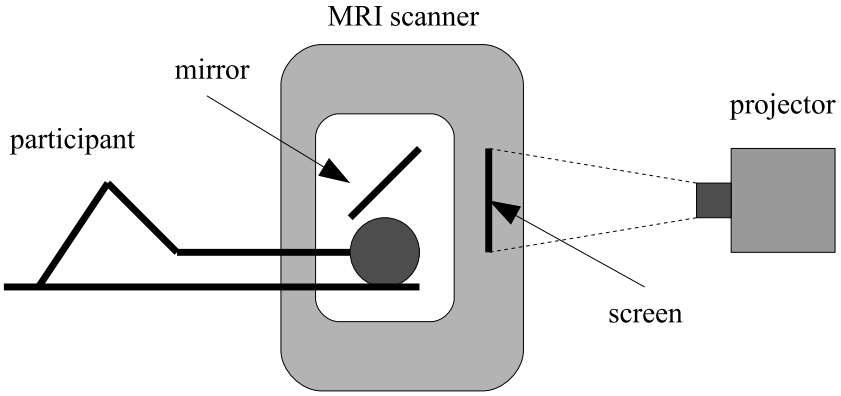

Figure 2.4: Presentation of visual stimuli inside an MR scanner. Stimuli were presented with a projector onto a screen inside the scanner and were seen by participants reflected in a mirror above their heads.

Imaging was performed using a 3-Tesla MR head scanner (Siemens Allegra, Erlangen, Germany) with a standard one-channel head coil. During the experiment, functional scans ($T_2^\star$-weighted EPI sequence; TE = 30 ms; flip angle = 90°) were acquired using a TR of 2000 ms. Each volume consisted of 34 slices (gap 13 %) with 64×64 voxels of size $3 \times 3 \times 3$ mm^3. The slice order was interleaved, that is the slices 1, 2, ..., 34 were measured in the order 2, 4, 6, ..., 34, 1, 3, ..., 33. After the experiment a high-resolution sagittal T_1-weighted scan was acquired using a magnetization prepared rapid gradient echo sequence (MPRAGE; TR = 2250 ms; TE = 2.6 ms; 1 mm isotropic voxel size), to obtain a high resolution 3D structural scan.

Before using the MRI data for further analysis, several well established preprocessing steps had been performed. The major part of the preprocessing was done using the SPM5 toolbox (Welcome Department of Imaging Neuroscience, London, UK) running under MATLAB (2007a, The MathWorks, Natick, MA).

At first, temporal artifacts were accounted for. Because two different slices of a volume are measured at different times, a delayed BOLD response is measured in different slices. A common method exists to correct these differences in image acquisition time between slices, called *slice timing*. This is done by temporally interpolating [139] the slices onto a chosen reference slice and is implemented into the SPM5 toolbox. Due to the interleaved slice order during the measurement, slice 1 was chosen as the reference slice.

After this temporal alignment, head movements caused by muscle relaxation / tension or swallowing or other motor actions affecting head position, like pressing a button or eye-movements, have to be considered. I applied the standard *realign algorithm* [50] implemented in SPM5 using a 6 parameter (rigid body) spatial transformation and a least squares approach. All participants showed sufficiently small head motion (below 3 mm and 3° respectively) for all 6 dimensions (3 translations and 3 rotations). Hence, movement distances lay within voxel-size.

In the next step, the structural scan of each participant was transformed into the coordinate space of the functional scans. This step is called *coregistration*, and is also implemented into the SPM5 toolbox. It uses a rigid body transformation maximizing normalized mutual information of a functional reference image and the structural scan [30] [156]. After this procedure the mm voxel coordinates of the functional and the structural images are in the same space, and functional voxels can be mapped onto the structural image.

In most fMRI studies investigating a group of subjects, it is necessary to fit each individual's voxel coordinates onto a standardized brain template to account for global and local anatomical differences. This is called *normalization*. Again the normalization algorithm implemented in SPM5 was used which uses the MNI template (mean structural volume over 305 subjects obtained at the Montreal Neurological Institute) also called *MNI*305 template [43] [100]. By doing so, the data undergoes a spatial smoothing, which might destroy spatial patterns of interest (compare chapter 2.3.1). Hence, the raw, non-normalized data is used for connectivity analysis, and the normalized data is only used for region of interest definition in order to validate and compare the found regions to those of other fMRI studies.

The last two preprocessing steps consisted of the removal of the temporal mean from each voxels time course and a bandpass filter using matlab's implemented fast Fourier transformation [32] [37]. The frequency band of interest for fMRI connectivity studies lays between 0.005 Hz and 0.15 Hz [138] [137], and was chosen for filtering. Figure 2.5 shows the time course of a voxel before a) and after b) these two last preprocessing steps.

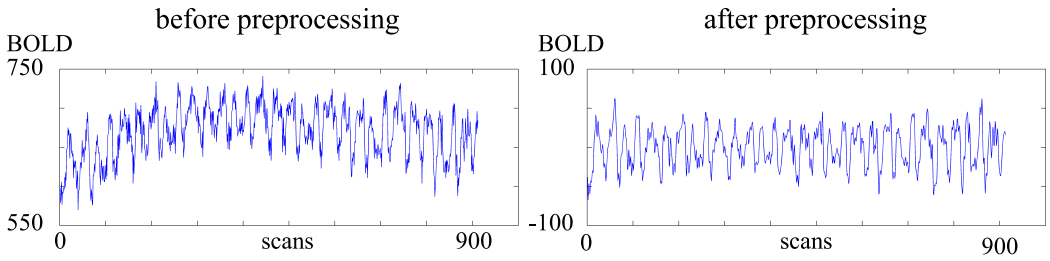

Figure 2.5: Voxel time course before and after final preprocessing. A voxel inside the visual cortex was chosen from subject 1 of the first fMRI study (compare 3.2). Both graphs show the temporal evolution of the BOLD signal of this voxel. Each point respresents the BOLD activity (y-axis) of the voxel at a specific time (x-axis). The left graph shows the time course after slice timing and realignment. Applying the final mean-removal and bandpass filtering leads to the time course shown in the right graph. The resulting time course is slightly smoother and with less of a trend through the bandpass-filter.

2.2 FMRI correlates of neuronal connectivity

When studying neuronal connectivity, one has to distinguish between two types of connectivity - one that can be directly inferred from the data, and the other underlying and causing the data. The first is referred to as *functional connectivity* and, due to Friston, reflects the *"temporal correlations between remote neurophysiological events"* [48] [46]. The second type is denoted as *effective connectivity* and represents *"the influence one neural system exerts over another"* [46]. Naturally the analysis of effective connectivity is more difficult than the analysis of functional connectivity. For example, using fMRI data one has to account for the HRF function as a filter between the measured BOLD level, in which most aspects of functional connectivity can be studied, and the underlying neuronal level, where the most important properties of effective connectivity are found.

On the basis of fMRI data, neuronal connectivity can be analyzed on several spatial levels. For example, one might be interested in the connectivity between single voxels or larger parts of the brain, or even between patterns extending across the whole brain. In my thesis I am interested in the connectivity between brain regions. In most cases, and in particular in this thesis, ROIs are given as compact (nearby voxels) sets containing about hundred voxels. But in general, a ROI might be given through any (non-empty) set of voxels. Inside a connectivity study, I assume all ROIs to be disjoint voxel sets.

This chapter is divided into two subchapters. In chapter 2.2.1 a brief overview of different aspects of connectivity and the most common techniques to study them is given. In chapter 2.2.2 an advanced technique called dynamic causal modeling (DCM), which will be of interest for later analysis, will be discussed in greater detail. As before, I limit methods to only those concerning fMRI data.

2.2.1 Neuronal connectivity

In general, a point of interest is the causal relationship between the considered brain regions. Unfortunately, existing approaches to study connectivity only reflect - but are not identical to - underlying physiological causal interactions [144] [20]. One must be sure to make a distinction between the interactions for the levels of measued BOLD signal and the underlying neuronal activations. When not otherwise specified, I refer to the BOLD level.

Several questions about interactions and interdependencies between brain areas can be of general interest. According to the particular area of interest, several approaches have been developed for fMRI and other neuro-imaging techniques in order. In the following passage, I will list the most important of these connectivity properties.

Considering two time courses, associated, for example, with two voxels or two brain areas, probably one question is whether these areas show related temporal behavior or not. In most cases *related* means that the time courses show a correlation [118] significantly different from zero. Related behavior indicates that two brain parts are involved in the processing of the same stimulus or task, and, for example, process different features of the stimulus. By definition related time courses are functionally connected.

The next question, for two brain areas, found to be related, is whether other

regions cause the similar behavior. For example, if a newly discovered functional connectivity between two areas is also effective or can be traced back to a common source. Methods, which are capable of revealing common sources of investigated signals, are called *partial*.

For any effective connection, the question arises as to which direction information travels and if one area inhibits or excites the other. In particular, if an activation increase (higher neuronal activation / BOLD) in one area goes along with an increase or decrease inside another area and how strong these influences are. An increase in BOLD activity does not necessarily imply an increase in neuronal activity (see section 2.1.2), and an excitation on the BOLD level may be caused by an inhibition on the neuronal level. Almost all connectivity analysis approaches give a measure of connection strength (compare Tab. 1).

method	intens.	direct.	part.	HRF
Pearson's correlation	X			
mutual information	X			
(PS) Granger causality	(X)	X	(X)	
(PD) coherency	X	(X)	(X)	
SEM	X	X	X	
DCM	X	X	X	X
RPC	X	X		

Table 1: Common methods to study neuronal connectivity with fMRI data. The table gives an overview of which technique (first column) can be used to investigate particular connectivity properties (intens.=intensity, direct.=direction, part.=partial, HRF=HRF). The last column indicates which of the methods explicitly include a model for the HRF response. Marks in brackets (X) indicate that a derivative of the method can be used to study this connectivity property.

During the last two decades, several techniques have been developed to study these connection properties on the basis of fMRI data. Table 1 gives an overview of the most prominent of these methods.

Some of these methods were originally developed in other scientific areas one of which is *Granger causality* [53] [52], which is based on the predictability of one time series from the previous behavior of another, and was first used in financial economics. *Coherency* [112] and *relative power contribution* (RPC) [168] analysis techniques, which compare the power spectra of time series and are related to Granger causality, were successfully applied onto fMRI data [35] [144] [99] and extended in order to cover more and more connectivity properties [7] [54] [157] [8].

Other methods were explicitly developed for fMRI data. The most prominent of these approaches is *dynamic causal modeling* (DCM) [49], which is based on *structural equation modeling* (SEM) [102]. Both algorithms compare estimated a-priori models and allow inferences about effective connectivity. Whereas SEM models the connection directly on the measured BOLD level, DCM distinguishes between the neuronal level and the hemodynamic level [122]. SEM and dynamic causal modeling have been applied onto fMRI [12] [40] [44] and EEG/MEG data [34].

In the scope of my thesis, values representing a connectivity property are denoted as *connectivity measurement*. For example, the correlation between two voxels is a connectivity measure of functional connectivity.

This thesis restricts to the methods of Pearson's correlation analysis [58] and dynamic causal modeling [49]. Before a more detailed discussion of DCM, I explain how correlation analyses was conducted.

In general, for two random variables X and Y, their correlation is defined as:

$$\mathrm{corr}(X,Y) = \frac{\mathrm{cov}(X,Y)}{\sqrt{\mathrm{var}(X)}\sqrt{\mathrm{var}(Y)}} = \frac{E((X - E(X))(Y - E(Y)))}{\sqrt{\mathrm{var}(X)}\sqrt{\mathrm{var}(Y)}}. \tag{9}$$

For two series x and y of the random variables X and Y, each containing $T \geq 2$ samples, the correlation between X and Y can be approximated using empirical correlation

$$r_{x,y} = \frac{\sum_{t=1}^{T}(x_t - \overline{x})(y_t - \overline{y})}{\sqrt{\sum_{t=1}^{T}(x_t - \overline{x})^2 \sum_{t=1}^{T}(y_t - \overline{y})^2}}, \tag{10}$$

where $\overline{x}$ and $\overline{y}$ are the empirical mean values:

$$\overline{x} = \frac{1}{T}\sum_{t=1}^{T} x_t, \quad \overline{y} = \frac{1}{T}\sum_{t=1}^{T} y_t. \tag{11}$$

In my case, $x = (x_1, ..., x_T)$ and $y = (y_1, ..., y_T)$ are time series for which each coefficient x_t (or y_t) represents BOLD activity at scan t. In addition to the empirical correlation over the entire experiment $r_{x,y}$ I will be interested in the correlation between x and y only during a specific condition $u : \mathbb{R}_0^+ \to \{0,1\}$ (compare chapter 2.1.2). Let u_B be the baseline or resting state condition during which participants rested, then I define the for u restricted correlation $r_{x,y}|_u$ between x and y as

$$r_{x,y}|_u := \frac{\sum_{t \in T_u}(x_t - \overline{x}|_u)(y_t - \overline{y}|_u)}{\sqrt{\sum_{t \in T_u}(x_t - \overline{x}|_u)^2 \sum_{t \in T_u}(y_t - \overline{y}|_u)^2}}, \tag{12}$$

where $T_u = \{t \in \{1, ..., T\} | u(t-3) = 1 \vee u_B(t-3) = 1\}$ is the index subset containing all scans from conditions u and u_B shifted by six seconds assuming TR = 2 s. Mean values $\overline{x}|_u$ and $\overline{y}|_u$ are also calculated over T_u. The shift of 6 s compensates for the delayed BOLD response of the signals. Now $r_{x,y}|_u$ is the correlation between x and y during conditions u and u_B.

If x and y contain the measured BOLD time series of two different voxels, the connectivity measure $r_{x,y}|_u \in [-1,1]$ can be interpreted as the strength of functional connectivity between x and y during condition u.

2.2.2 Dynamic causal modeling

Dynamic causal modeling (DCM) was first presented in 2003 by Friston [49] to model effective connectivity from fMRI data. Since its original publication many

studies have applied DCM (e.g. [130] [12] [153] [150] [44] [40] [88]). DCM distinguishes between two levels: neuronal and hemodynamic. Model parameters, which represent the neuronal connectivity structure, are estimated so that simulated BOLD responses, using these parameters, fit measured signals. Each region is represented with the first component of the ROI's PCA decomposition.

Neuronal activity of each region of interest is modeled as a function $z_i : \mathbb{R}_0^+ \rightarrow \mathbb{R}$ with $z_i(t)$ giving the neuronal activation of the i-th region at time t. For a model of N regions, the state vector

$$z(t) \;=\; (z_1(t),\, ...,\, z_N(t))^t \;\in\; \mathbb{R}^N \tag{13}$$

represents the state of the system at time t. Via the balloon model [19] the neuronal activation $z(t)$ can be transformed into a BOLD response $y_i = \lambda(z_i, H_i)$ for each region separately. Here the vector H_i contains 5 parameters of the balloon model. Paradigm-specific conditions u_1, ..., $u_M : \mathbb{R}_0^+ \rightarrow \{0,1\}$ forming the condition vector $u(t) = (u_1(t),\, ...,\, u_M(t))^t$ activate the model and modulate effective connectivity embedded at the neuronal level through a bilinear model:

$$\dot{z}(t) = \left(A + \sum_{i=1}^{M} u_i(t) B^i \right) z(t) + Cu(t) \tag{14}$$

Matrices A, B^1, ..., B^M, and C are model dependent parameters. Together with the $5N$ parameters $H = (H_1,\, ...,\, H_N)$ of the balloon model, these parameters form a vector $\theta = (A,\, B^1,\, ...,\, B^M,\, C,\, H)$, which defines the dynamic causal model.

The $N \times N$ dimensional matrix $A = (a_{ij})_{i,j=1..N}$ in Eq. 14 represents intrinsic connections between brain areas. Coefficient a_{ij} gives the interaction from the j-th region to the i-th region. A negative coefficient represents an inhibitory and a positive an excitatory interaction. To ensure system stability the self-connection (diagonal elements of A) for each area is set to -1 and can neither be changed in the a-priori model, nor does it vary during parameter estimation.

Matrix $B^i = (b^i_{jk})_{j,k=1..N}$ for stimulus u_i represents the modulation associated with this stimulus at the intrinsic connections. Coefficient b^i_{jk} gives the modulation of connection from region z_k to region z_j by regressor u_i.

Finally, the $N \times M$ matrix $C = (c_{ij})_{i=1..N,j=1..M}$ describes the way stimuli evoke activation in the brain areas. If c_{ij} is positive (negative), condition u_j excites (inhibits) region z_i. Fig. 2.6 illustrates the parameter matrices.

DCM parameters in A, B^1, ..., B^M, and C correspond to rate constants of the modeled neurophysiological process and are given in Hertz [49]. They represent connectivity measurements of effective connectivity obtained with DCM and yield information about partial strengths and directions of the connections between ROIs (compare Tab. 1).

To work with DCM, one needs to specify an a-priori model, which serves as a starting point for the model estimation in the space of all models. Model parameters are estimated using an EM-algorithm [49], in order to minimize the difference between measured BOLD response and the model prediction [49]. In the a-priori model one only states if a connection is present (e.g. $a_{23} = 1$) or absent (e.g. $a_{23} = 0$). Model parameters specified as zero are not varied during estimation and stay zero.

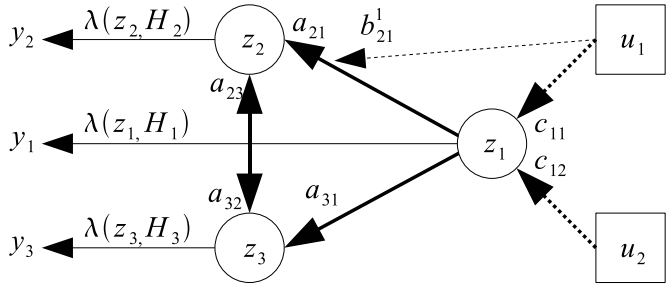

Figure 2.6: Parameters of a dynamic causal model. Example DCM with $N = 3$ regions and $M = 2$ conditions. External stimuli u_1 and u_2 excite area z_1 (most right, dotted bold arrows) with strengths c_{11} and c_{12}. Via two connections with strengths a_{21} and a_{31}, area z_1 impacts regions z_2 and z_3, which are also directly connected with strengths a_{23} and a_{32}. In addition condition u_1 modulates the connection from z_1 to z_2 with strength b^1_{21}. Finally, the neuronal activations z_1, z_2, and z_3 of the three regions can be transformed into BOLD responses y_1, y_2, and y_3 using the balloon model and region specific HRF parameters H_1, H_2, and H_3.

I used the algorithms provided by SPM5 (The Welcome Dept. of Imaging Neuroscience, London, UK) for parameter estimation and comparison of dynamic causal models.

Normally, one derives a basic a-priori model from literature and specifies more detailed variations of this basic model representing different connectivity hypotheses. Then these models are estimated and compared resulting in a favored model [121] which confirms or contradicts the a-priori stated hypothesis about connectivity.

Models are compared pairwise based on the Akaike information criterion (AIC) [2] and the Bayesian information criterion (BIC) [143]. Hereby BIC tends to favor simple models and AIC complex models [79]. During the rest of this chapter I use small indices i and j to denote dynamic causal models. For a model i I denote these information criteria as AIC_i and BIC_j, and compute associated Bayes factors for a model comparison of a model i and another model j as [79] [80]:

$$B_{ij}^{\mathrm{AIC}} := \frac{e^{\mathrm{AIC}_i}}{e^{\mathrm{AIC}_j}}, \quad B_{ij}^{\mathrm{BIC}} := \frac{e^{\mathrm{BIC}_i}}{e^{\mathrm{BIC}_j}} \tag{15}$$

Now if $B_{ij}^{\mathrm{AIC}} > 1$ then the data favors model i over model j and vice versa for $B_{ij}^{\mathrm{AIC}} < 1$. With regard to the significance level for p-values $p < 0.05$, a similar criterion was given by Raftery [129] for Bayes factors. Accordingly model i is weakly, positively, strongly, or very strongly favored over model j if (same for BIC):

$$B_{ij}^{\mathrm{AIC}} \in [1,3],\ (3,20],\ (20,150],\ \text{or}\ (150,\infty) \tag{16}$$

The Bayes factor can also be interpreted as odds ratios. A Bayes factor $B_{ij}^{\mathrm{AIC}} = 20$, for example, corresponds to odds of $20:1$, which means that given hypothesis i and j a Bayes factor $B_{ij}^{\mathrm{AIC}} = 20$ corresponds to a belief of 95 % in the statement *hypothesis i is true*. Following Raftery [129], this corresponds to strong evidence in favor of model i above j.

As in [121], I choos a conservative cutoff value and favor model i above model j only if both Bayes factors B_{ij}^{AIC} and B_{ij}^{BIC} are above 3. As in [151], this is regarded as positive evidence for model i.

In most cases, one considers more than two models and is confronted with several comparison results for different participants, which will agree or disagree to some extend. For group studies with more than two models, advanced techniques of model selection exist [152] [151]. Here, I want to follow the technique proposed by Stephan and Penny [151] [150]. In this way a *positive evidence ratio* (PER) is computed as the number of comparisons over subjects for which both criteria B_{ij}^{AIC} and B_{ij}^{BIC} passed the threshold for positive evidence. Considering, for example, 20 subjects, then the PER of the model comparison i against j may be $12:5$. Here, both criteria showed consistent evidence for model i for 12 of the subjects and model j was supported for 5 subjects. In the remaining 3 cases, criteria differed or showed no consistent evidence. Comparing model i against j I say that the PER is in favor of model i if the ratio is above 1, meaning that model i was favored for more participants than model j.

Finally considering M models, I want to determine a hierarchy between models. I begin by selecting a superior model to that model for which all PERs were in favor. Note that this may not always determine a unique superior model. In cases in which no superior model can be chosen because no model is favored by the PER against all others, I choose that model(s) as superior for which all except one (two, three, etc.) PERs are in favor. This model(s) will be noted as model(s) of first rank. Now I consider all except this superior model(s), and select the next model out of the remaining ones for the second rank. Repeating this procedure until no models are left provides a unique rank order on models, for which some models may share the same rank. An outlined example for the determination of the hierarchy on models is given in section 3.2.4 below Tab. 9 on page 65.

Depending on the DCM-model and on the time series the parameter estimation requires long computational times. This makes estimation of a large number of models, in the case of restricted information about an a-priori basic model, or the hypothesis, a time-consuming undertaking.

With a growing number of regions the number of possible models also grows. This is of particular interest for the present work because I plan to decompose regions into patterns resulting in an even larger N. Due to strong a-priori knowledge and simple models, this will not be a major problem for this thesis but might become a time-consuming step for more complex studies. I close the chapter with a citation from George E.P. Box that *"all models are wrong, but some are useful"* [16] (p.424).

2.3 Multi-variate pattern analysis and matrix decompositions

One of the most recent developments in neuroscience is the analysis of multi-voxel patterns. Since its first application onto fMRI data by James Haxby in 2001 [59] many other studies concerning multi-voxel patterns have been published (e.g. [33] [27] [77] [60] [74]).

After the introduction of some general notations which will also be used later, a short overview of multi-voxel pattern analysis (MVPA), its limitations, and its potentials will be given in section 2.3.1. Then I will state the most prominent matrix or data decompositions in sections 2.3.2, 2.3.3, 2.3.4, and 2.3.5, which will all be of interest during this thesis.

2.3.1 Multi-variate patterns

Firstly, I introduce the general notations used during the rest of this thesis: The number of scans of an fMRI experiment is denoted as T, where the time between two consecutive scans is TR= 2 s. Each measured volume is of the same dimension $\dim_x \times \dim_y \times \dim_z$ and therefore consists of $S = \dim_x \times \dim_y \times \dim_z$ voxels. For simplicity each of these 3-dimensional volumes is rearranged into a S-dimensional row vector Y_t, where $t = 1, ..., T$. For a voxel index $s = 1, ..., S$ the activity of the corresponding voxel is denoted with y_{ts}. Now the whole fMRI measurement yields a data-matrix Y of dimension $T \times S$ (compare Fig. 2.7)

$$Y = \begin{pmatrix} y_{11} & \cdots & y_{1S} \\ \vdots & & \vdots \\ y_{T1} & \cdots & y_{TS} \end{pmatrix}. \tag{17}$$

For a subset of voxel indices $I = \{i_1, ..., i_{N_I}\} \in \wp(\{1, ..., S\})$, where $\wp$ is the power set and N_I the number of voxels in the set, I define

$$Y^I := \begin{pmatrix} y_{1i_1} & \cdots & y_{1i_{N_I}} \\ \vdots & & \vdots \\ y_{Ti_1} & \cdots & y_{Ti_{N_I}} \end{pmatrix} \tag{18}$$

as the data-matrix for the voxels with index in I (compare Fig. 2.7 red colored). I may contain, for example, the indices of all voxels within a certain range from a seed voxel.

For such a region I, I define a *multi-voxel* or *multi-variate pattern* (MVP) to be a vector $C \in \mathbb{R}^{N_I}$, thus representing a spatial activation pattern of the region I (e.g. [77] [62]). Given a region I, for example, each row of Y^I being nothing else but a scan of the region represents a MVP.

Different stimuli may induce different multi-voxel patterns over the voxels of an area. One can study the discrimination degree of the area for different stimuli by analyzing how well spatial activation distributions (MVPs) can be used to predict the presented stimulus, during a scan. Clustering techniques such as *support vector machines* (SVM) are applied to distinguish the different patterns [106]. An informative introduction to MVPA for fMRI data is given in [62] or [108]. Figure 2.8 shows an hypothetic fMRI paradigm illustrating the principle of multi-variate pattern analysis.

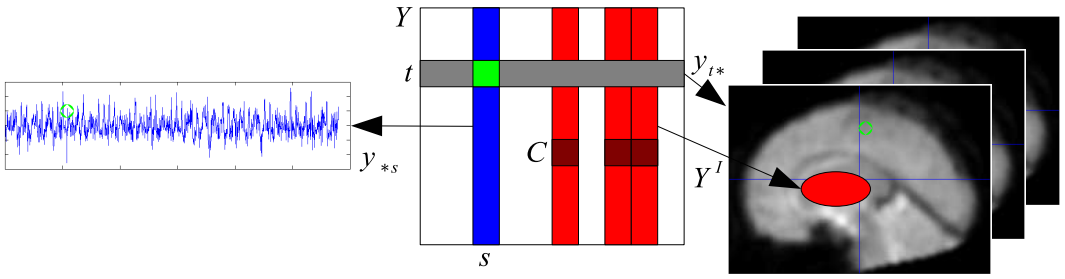

Figure 2.7: Scheme of data-matrix Y. Each row $y_{t\star}$ of Y (e.g. the gray row) represents the measured brain volume at time t and each column $y_{\star s}$ (e.g. the blue column) the time series of voxel s. The data Y^I of a ROI I and a MVP C inside I is illustrated in red / dark red. The green dots represent the activation of voxel s at time t.

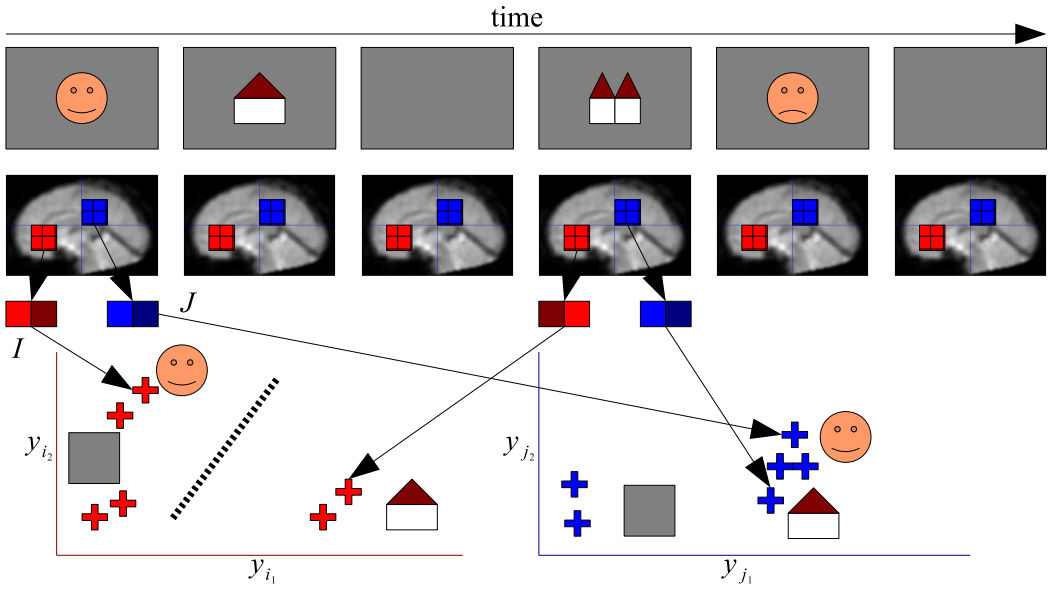

Figure 2.8: Scheme for multi-voxel patterns. During fMRI measurement, participants see faces, houses, or an empty gray screen (first row). BOLD response is measured for each stimulation. For simplicity, measured volumes are visualized through a single slice. Now let $I = \{i_1,i_2\}$ and $J = \{j_1,j_2\}$ be two index sets representing two brain areas (red and blue region), consisting both of only two voxels. For both areas, the activations of its two voxels are plotted in a graph. Different pattern vectors represent different mental states (e.g. stimulus evoked activation patterns). At first I want to look at the mean (over voxels) activation of the two areas. This is the distance between the crosses and the origin. Whereas the empty screen evokes low activation, the houses and faces evoke high activation in both areas. So both areas have information whether a stimulus (house, face) is presented or not (empty screen) due to a high or a low mean activity. Additionally, the activation pattern inside the red area can be used to distinguish faces and houses (bold dotted black line) whereas in the blue area both stimuli evoke the same multi-voxel pattern.

Although the concept of MVPA seems very intuitive, I nevertheless want to describe the neurophysiological mechanisms that lead to different activation patterns

for an important case in more detail, because they depict the limits of the method, which also mark the boundaries of my thesis.

Probably the most prominent area showing different spatial activation distributions is the visual cortex. Before functional imaging techniques were invented, it was known from studies on cats and monkeys (e.g. [71] [113] [13] [124]) that orientation selective columns of neurons exist in the visual cortex. These neurons show stronger activation during the presentation of a specific orientation than for other orientations. In monkeys these columns showed only a width of about $300-500\mu$m [166]. Although this size is too small for fMRI to map single columns, the distribution of columns for different orientations varies between voxels (compare Fig. 2.9 taken from [62] Fig. 2). In general, MVPs are subject specific [28]. Until the introduction of fMRI, functional non-invasive imaging techniques lacked the necessary spatial resolution to probe into these feature representations.

Note that in Fig. 2.8 and all figures following, a 3-dimensional brain volume is represented by a single slice for reasons of clarity.

Because the concept I propose makes explicit use of different spatial activation patterns, it can only be applied onto brain areas which exhibit those. It has been shown that MVPs can be distinguished for many different stimulus types and task types, for example, different colors [114], auditory word stimuli [95], odors [70], states of awareness [165], and touches [9]. Hence, pattern connectivity is applicable to a variaty of stimulati and tasks.

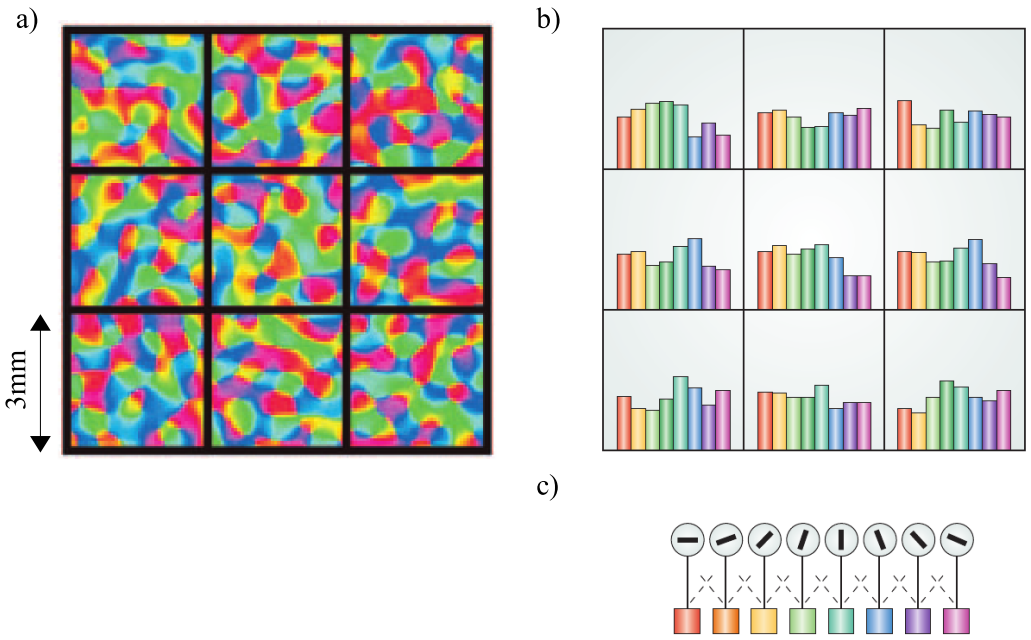

Figure 2.9: Scheme for orientation-selective column distribution. a) The spatial distribution of orientation selective columns is presented, color coded according to c). Spatial resolution of fMRI indicated by the measurement grid in a) (nine black squares) is too raw to map the single columns. However, the distribution of the orientation selective components varies over the nine voxels b). This causes subtly different response patterns in the early visual cortex for differently oriented stimuli. The images were taken from [62] Fig. 2.

2.3.2 Matrix decompositions of fMRI data

For a data-matrix Y (as in Form. 17 or only for a region I) a linear matrix decomposition into P components is given by

$$Y = XC + E \tag{19}$$

Here, I want to denote the $T \times P$-dimensional matrix X as the *temporal pattern matrix* and the $P \times S$-dimensional matrix C as *spatial pattern matrix*. E represents a remaining error matrix, which must not necessarily be unequal to zero. For such a matrix decomposition, I denote the p-th temporal pattern (p-th column of X) as X_p and the p-th spatial pattern (p-th row of C) as C_p.

Each coefficient of the data-matrix Y is the weighted sum of the patterns in C with weights from X (compare blue colored row and column in Figure 2.10).

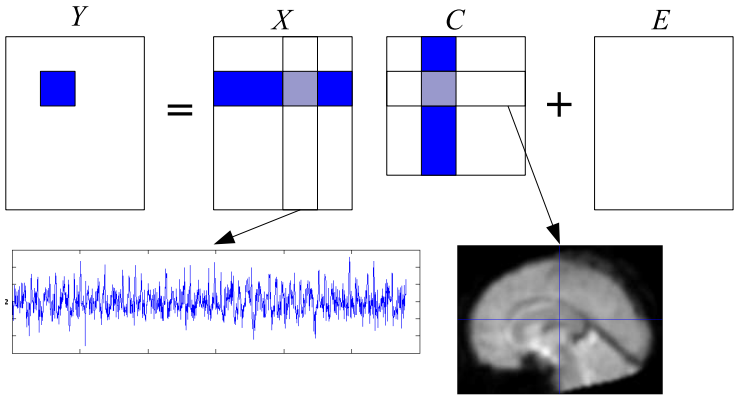

Figure 2.10: Scheme of a matrix decomposition. The columns X_p of X can be interpreted as time series associated to the brain volume given as a row C_p of the matrix C.

Of course, for a given data-matrix Y, many different matrices C, X, and E exist, for which Eq. 19 holds.

2.3.3 The general linear model

A frequently used matrix decomposition for fMRI data is the general linear model (GLM) [50]. Here, the data-matrix Y is modeled as a weighted superposition of the hemodynamic response functions associated with the onsets (compare chapter 2.1.2), which are stored in the so called *design matrix* X:

$$Y = X\beta + E, \quad y_s(t) = \sum_{p=1}^{P} X_p(t)\beta_{ps} + E_{ts}, \quad X_p = \tilde{u}_p = h * u_p, \tag{20}$$

where P is the number of used conditions u_1, ..., u_P given by the paradigm, β is the weighting or parameter matrix of the linear model, and E the matrix of normally distributed error terms. Each column X_p of the design matrix X represents an experimental condition and is the HRF onset function associated to

u_p (see Fig. 2.11 and compare chapter 2.1.2). Therefore the time course of each voxel is modeled as a weighted superposition of all HRF onset functions.

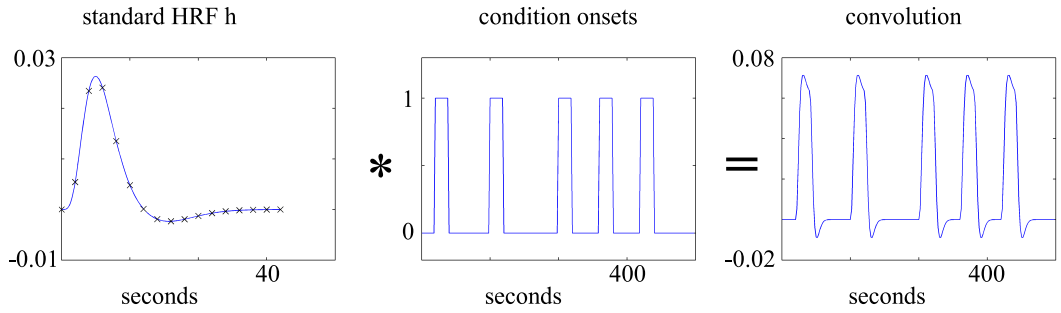

Figure 2.11: Computation of GLM design matrix X. Convolution of the standard HRF h (left) with the condition onsets (middle) yield a column of design matrix X (right). For each voxel it is desirable to know for which weighting (parameter matrix β) of these convolutions their superposition fits the voxel's measured time course best.

If X has full rank, which can easily be achieved by accurate paradigm design and definition of used conditions, an approximation b of the unknown β matrix can be estimated using least squares [50] [140]:

$$b = (X^t X)^{-1} X^t Y. \tag{21}$$

The matrix coefficient b_{ij} can be thought of as an effect strength of the i-th experimental condition on the j-th voxel. The effects of conditions onto a voxel s can be contrasted against each other with t-statistics, using contrasts $c = (c_1, ..., c_P)$ of the parameter estimates $b_s = (b_{1s}, ..., b_{Ps})^t$. The significance of a specific contrast c for a voxel s is tested with a t-test using

$$t_s = \frac{cb_s}{\varepsilon_s}, \quad \varepsilon_s^2 = \frac{(y_s - Xb_s)^t (y_s - Xb_s)}{T - \text{rank}(X)} c(X^t X)^{-1} c^t. \tag{22}$$

Now t_s follows the Student's t-distribution with $T - rank(X)$ degrees of freedom (see [50] [68]) and is called the *t-value* of the voxel with respect to c.

If, for example, three conditions are modeled in the design matrix $P = 3$ and for a voxel s onw wants to know wether the effect of the second condition is greater than the one of the first, one can examine the contrast $c = (-1, 1, 0)$ and compute t_s. A high t_s points to a significantly (corresponding to Student's t distribution) higher effect of the second condition onto the voxel, as of the first condition. From the t-value one can compute the *p-value* [50]. Under the null hypothesis that a voxel s shows no activation which is related to a contrast c (e.g. for $c = (-1, 1, 0)$), the p-value gives the probability of obtaining a t-value at least as extreme as the actually observed. So for small p-values (normally below 0.05 or 0.001) one rejects the null hypothesis because the probability for the actual observation is very low. Hence, the alternative hypothesis - that the voxel was related to the contrast - is accepted.

Because GLM deals with each voxel separately, it is called a univariate approach. Due to the great number of voxels, one has to account for false positives [50]. For

each contrast one gets a *statistic parametric map* (SPM) by assigning each voxel's t-value to the voxel's position. For an example of a SPM, see Fig. 2.12.

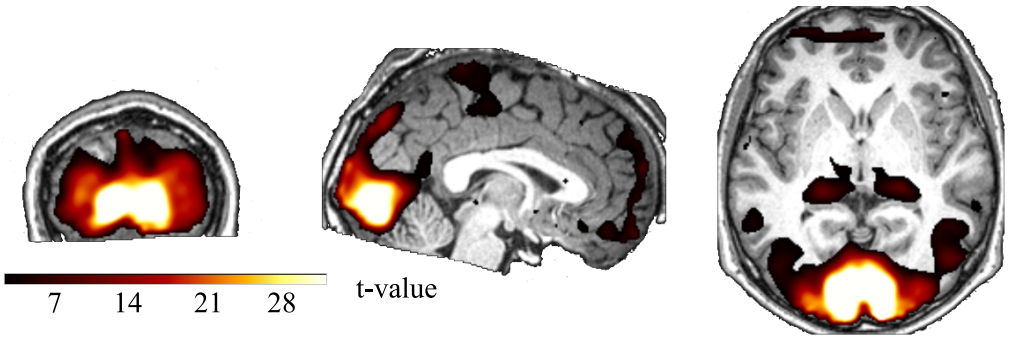

Figure 2.12: SPM t-value image of a GLM contrast. Voxels with an associated t-value above a threshold of 3 (approx. $p < 0.001$) are mapped color coded onto a structural scan. The t-value increases from dark red to white whereas the p-value decreases. Here one sees a strong activation of the visual cortex.

One way to define a ROI would be to add all adjacent voxels, which exceed a given t-value threshold, to a ROI's index set. The t-value threshold and the minimum number of voxels can be varied and used as parameters for more liberal or conservative ROI definition.

For GLM the temporal patterns can be seen in a similar way to optimal temporal components, and the spatial patterns in β as corresponding spatial components.

2.3.4 Principal component analysis

Another important matrix decomposition used in various fields is *principal component analysis* (PCA) which was first described by Karl Pearson in 1901 [118]. Mathematically, PCA is an orthogonal coordinate transformation, such that the projection of the transformed data on the first coordinate (first principal component) yields the greatest variance over all projections, the projection onto the second coordinate the second greatest, and so on [76].

Figure 2.13 shows an example PCA. The original data set (red) is rotated so that the new first coordinate (horizontal axis) lies in the direction of greatest variance. The transformed data set is colored in blue. For fMRI the axes in Fig. 2.13 would correspond to voxel activities y_s.

For a $T \times S$ data-matrix Y with zero temporal mean, a PCA decomposition can be computed, using singular value decomposition of Y:

$$Y = XC = W\Sigma V^t, \quad X = W\Sigma, \quad \text{and } C = V^t, \tag{23}$$

where W and V are $T \times T$ and $S \times S$ orthogonal matrices and Σ is a $T \times S$ diagonal matrix with real-valued non-negative coefficients on the diagonal. $C = V^t$ can be thought of as the inverse of the orthogonal transformation and $X = W\Sigma = YC^t$ as the transformed data.

It is easily seen that the orthogonal transformation V^t diagonalizes the covariance matrix Y^tY of the data:

$$V^t Y^t Y V = \Sigma^t \Sigma. \tag{24}$$

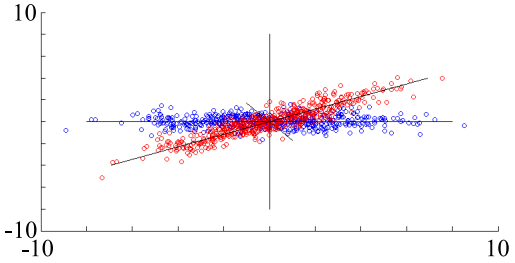

Figure 2.13: Illustration of principal component analysis. For a hypothetical 2-dimensional dataset (red circles) PCA determines the two orthogonal directions (rotated coordinate axes), which explain the most variance. This means that the projection of the original data set onto these directions provides distributions with maximum variances. Application of the orthogonal transformation V^t onto the original data gives a now decorrelated dataset (blue circles).

Hence, the dimensions in the transformed data X are decorrelated. Using $C = \Sigma V^t$ instead of $C = V^t$ additionally leads to a normalization of the data, yielding a variance of 1 along the new coordinates (compare Figure 2.14). This is called *whitening transformation*. Now the diagonal matrix $\Sigma^t \Sigma$ of Eq. 24 becomes the identity matrix.

The diagonal elements of Σ represent the variance of the data along corresponding dimensions in V^t [76]. A suitable permutation of Σ, W, and V respectively arranges the diagonal elements of Σ in decreasing order beginning with the largest coefficient in Σ_{11}.

PCA is often applied for data compression using only the first few most relevant (in the sense of explaining most variance) components. Only the first $L < S$ components c_1, ..., c_L (rows of C) are used to project the S-dimensional data Y to a lower L-dimensional space $X_L = Y C_L^t$ with $C_L = (c_1^t, ..., c_L^t)^t$. For my thesis, this is of particular interest, because connectivity studies [144] [49] [172] normally project the data Y^I of a region I onto its first principal component c_1

$$x = Y^I c_1^t. \tag{25}$$

The time course x is called *first eigenvariate* and can be thought of as the time course associated to the spatial pattern c_1 explaining most of the variance inside the data relative to the other components. In the state of the art methods time course x representing region I is used for further connectivity analysis.

Next, I will describe another matrix decomposition that embeds more natural conditions than maximization of variance to components.

2.3.5 Independent component analysis

Due to the nature of most experimental data being a superposition of independent signals (also called sources or components), a more natural matrix decomposition called *independent component analysis* (ICA) [31] has been developed during the

1980s and is still a subject of ongoing research. ICA approaches not only decorrelate the signals as PCA does, but try to find statistically independent components. In general, two events A and B are said to be statistically independent if and only if

$$P(A \cap B) = P(A)P(B). \tag{26}$$

Figure 2.14 shows the difference between PCA and ICA schematically. In a), one sees the raw data matrix consisting of two signals, with each blue circle representing one measurement. After the PCA, one sees in b) the whitened data along uncorrelated dimensions but the two signals (dimensions) are still statistically dependent. Finally, one sees in c) the ICA result of two independent signals.

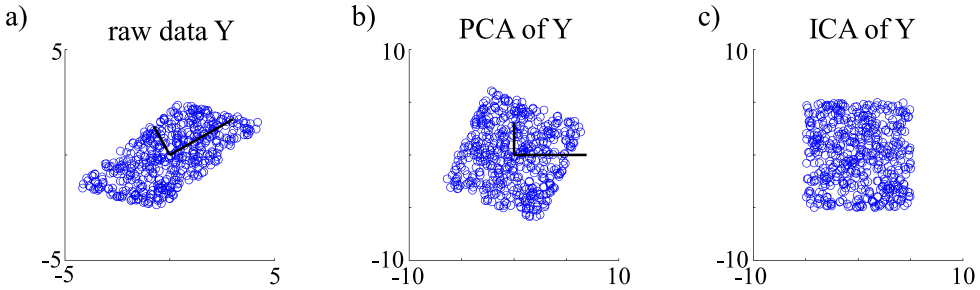

Figure 2.14: Illustration of PCA and ICA. In a) one sees the original data set (blue circles) and its two PCA eigenvectors (bold lines). After the PCA transformation and normalization (whitening) the transformed data set in b) is produced. Now both dimensions (bold lines in b)) are uncorrelated but still stochastically dependent. For example, one sees that small values in x-dimension are associated to larger variances in y-dimension than larger values in x-dimension. c) After a rotation, dimensions are also stochastically independent.

A general overview of ICA for both theory and applications is given in [73]. Using the previously introduced notation of a $T \times S$ dimensional data-matrix Y, an ICA approach gives a decomposition into P independent components

$$Y = {}^tX\,{}^tC, \tag{27}$$

where ${}^tX$ is a $T \times P$ matrix containing P independent time courses, corresponding to the P spatial patterns in the $P \times S$ matrix ${}^tC$. The upper left index ^{t} indicates that the ICA decomposition maximized the independence between temporal components in matrix ${}^tX$. By using the transposed Y^t instead of Y, one gets a decomposition

$$Y^t = {}^sC\,{}^sX, \tag{28}$$

where again ${}^sX$ contains the temporal and ${}^sC$ the spatial patterns but now the spatial patterns are independent from each other.

Many different numerical algorithms exist (e.g. [11] [25] [73]) for the estimation of components as less dependent from each other as possible. I work with an approach called *joint approximate diagonalization of eigenmatrices* (JADE) [25].

A theoretical overview of this method is given in [73] or [25] [26]. I refer to the JADE decomposition giving temporal independent components as tJADE and for spatial independent components as sJADE.

Due to the fact that many experimental data sets (as fMRI data) consist of temporal *and* spatial independent components, approaches were developed to jointly maximize components temporal and spatial independence [155] [159]. I again use the JADE variant called *spatio-temporal* JADE (stJADE) [159] for analysis later.

Because stJADE with $\alpha = 0$ does not give exactly the same results as sJADE, I explicitly used sJADE. tJADE is not replaced by stJADE with $\alpha = 1$ respectively.

Even though ICA accounts better for the form of the data than PCA it has some disadvantages: Independent component analysis cannot identify the actual number of source signals. All three ICA approaches have the number of independent components P as a free parameter. In general, different P yield different decompositions and components. In addition to this free parameter, stJADE has another free parameter $\alpha \in [0,1]$ weighting between a spatial $\alpha = 0$ or temporal $\alpha = 1$ decomposition. Principal component analysis has no free parameter, and one just chooses the first, most important component in the sense of explained variance. So, for ICA, one has to determine for which P (and α, or other free parameters) the decomposition is *optimal*. The way in which a decomposition might be *optimal* varies between applications. In section 3.1.3 I give a definition for *optimal* that was used for the application of pattern connectivity.

Furthermore, independent component analysis does not give a canonical ordering of the components, as PCA does. Hence, besides the lack of knowledge of how many components to extract, one does not know which of the extracted components are the most important or interesting ones. Some techniques (e.g. [91] [103]) have been proposed to circumvent this problem. In section 3.1.3 I address this issue in greater detail and present a solution for the application pattern connectivity.

Finally, ICA does not provide the proper scaling or sign of the source signals. This problem may be overcome with a-priori knowledge about the shape of the signals.

These problems and their impact on my thesis are addressed in greater detail in the following chapter. I used the ICA algorithms implemented in the MFBOX ([159]; http://mfbox.sourceforge.net/; Computational Intelligence and Machine Learning Group at the Institute of Biophysics, University of Regensburg, Germany) MATLAB toolbox for SPM5, to estimate ICA decompositions.

3 Pattern Connectivity and its applications

3.1 Pattern connectivity

This section describes the main idea of my work. In section 3.1.1 the central concept is introduced, followed by necessary assumptions about data and paradigm design in 3.1.2. Sections 3.1.3 and 3.1.4 are concerned with problems arising with this new concept and will present two solutions.

3.1.1 Introduction

As mentioned in the beginning, most fMRI studies concerning neuronal connectivity use ([130] [12] [153] [150] [44] [40] [88]) and recommend ([46] [144] [49] [172]) the first eigenvariate of the PCA decomposition (compare section 2.3.4) of a brain area for further connectivity analysis. Temporal behavior for each ROI is thereby represented in a single time course. Depending on preprocessing and one's ability to identify and eliminate artifacts in the data, this first eigenvariate gives a good approximation of the overall temporal behavior of a region of interest. However, if one wants to study connectivity between ROIs containing several patterns (for examples see section 2.3.1), the state of the art method is not applicable, because it gives only one time course per region.

I now propose to decompose ROI data with more natural matrix decompositions than PCA, in this case namely ICA (compare section 2.3.5), which, as I will show with the help two fMRI paradigms, are able to identify the single patterns. The methods for connectivity analysis after the component extraction stay the same as for the standard PCA approach (e.g. correlation analysis or dynamic caudal modeling). During my thesis, this method is referred to as *pattern connectivity*, emphasizing the fact that connectivity between patterns (instead of regions) is analyzed (compare Fig. 3.1). Besides ICA, other methods exist to extract pattern time courses. These are addressed in the discussion and future prospects sections (4.1 and 4.3).

A major difficulty of using ICA instead of PCA is the selection of suitable components. While for PCA the components are sorted and it is clear that the first component is to be used, because this is the one explaining most variance, one has no order for the ICA components. In the next section I give an algorithm describing the pattern selection. After the selection, the same methods (see chapter 2.2) can be applied which were developed for the standard method, to study connectivity between these components.

In the following I want to state necessary general assumptions allowing ICA to identify the MVPs and enabling a well-definied component selection.

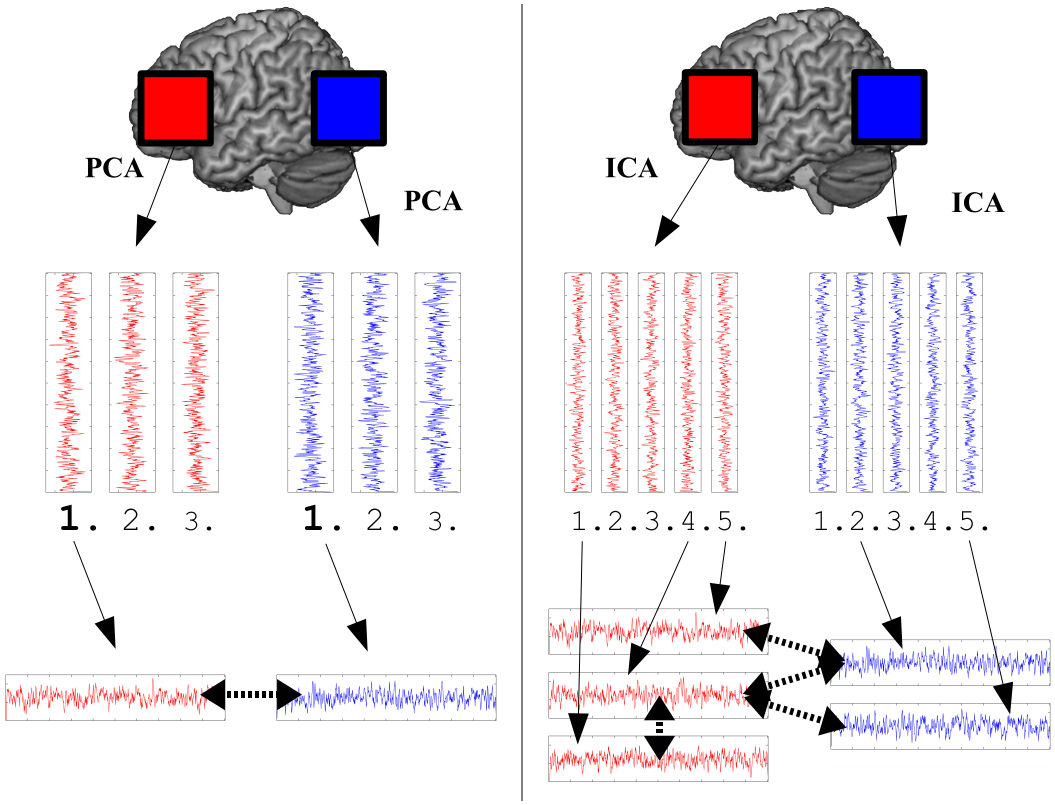

Figure 3.1: Scheme of PCA and ICA temporal components. A schematic example for a connectivity study between two regions (red and blue) is presented. The left side shows the standard state of the art PCA method. Each ROI is represented by the first principal component. The connectivity between these two principal components is further analyzed (e.g. unsing DCM). In contrast, the right side of the figure shows the newly proposed approach of pattern connectivity. Each ROI is decomposed into several components (using for example ICA) from which time courses associated to multi-variate patterns can be selected for further connectivity analysis. For both decompositions, PCA left and ICA right, the spatial parts of the shown components were omitted for better lucidity.

3.1.2 Assumptions

Same notations as introduced in section 2.3.2 are used. The $T \times S$ data-matrix Y of an experiment consisting of T scans over S voxels is taken as basis.

First assumption: The number N of regions of interest I_1, ..., I_N, as well as, the numbers $P_n \in \mathbb{N}$ $(n = 1, ..., N)$ of MVPs for each ROI must be known a-priori. For each of these $\sum_{n=1}^{N} P_n$ patterns, a condition onset function $u_p^{I_n}$ $(p = 1, ..., P_n)$ which evokes the pattern must adhere to the experiment.

The MVPs involved in the connectivity study are denoted as *patterns of interest* or short POIs. The spatial activation distributions of the POIs for a ROI I with

D voxels and P patterns of interest are denoted as $Z_p^I \in \mathbb{R}^D$ ($p = 1, ..., P$). A POI's time course is denoted as χ_p^I ($p = 1, ..., P$). The spatial (temporal) part of the COI is a row (column) vector. If ROI I contains only one POI and noise and artifact terms are ignored the ROI data Y^I is given as:

$$Y^I = \chi_1^I Z_1^I. \tag{29}$$

For a region of interest I that is not involved in the processing of condition u_p^I, the time course $\chi_p^I(t)$ is zero. This assumption is similarly stated for dynamic causal modeling for which the number of ROIs and an a-priori connectivity structure must be known. The major difference is that for DCM each region contains exactly one POI, whose time course is assumed to represent the ROIs principal temporal behavior and is estimated as the first PCA component.

Second assumption: Considering a ROI I with P POIs then each pattern of interest's time course χ_p^I ($p = 1, ..., P$) has to be positively correlated with the associated HRF onset function $\tilde{u}_p^I$ ($p = 1, ..., P$).

Because condition u_p^I causes the p-th POI Z_p^I, this assumption states that the evoked HRF of the p-th condition is positive. See Fig. 3.2) for the standard HRF h which is positive in a), a positive, but slightly different, individual HRF in c), and a negative HRF in b).

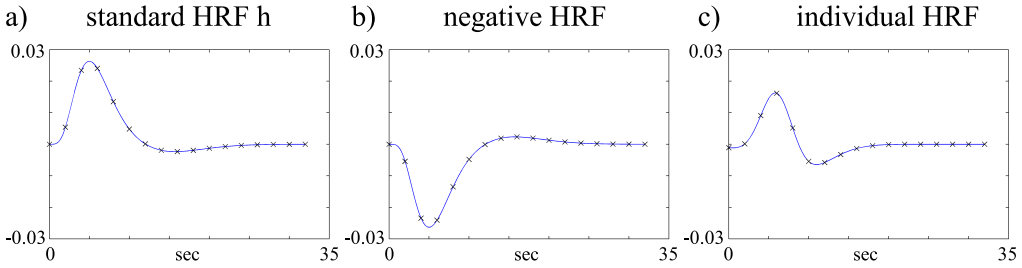

Figure 3.2: Pattern connectivity, second assumption. a) Time course of the standard HRF h. b) Negative HRF, which is negatively correlated with the standard HRF h and would not be allowed. c) Possible ROI-specific HRF response showing positive correlation with h. Black crosses mark measurement timepoints.

As stated above, the HRF can vary between subjects, regions of interest, tasks, and the presented stimuli ([169] [1] [101] [136] [104] [89]), so this assumption should be verified for each subject, region, and task separately. How well this assumption is met also depends on the studied connectivity type. However, in most cases the assumption is met [50] [19] [18].

Third assumption: Activation of region I is given as a linear model of its patterns of interest (compare also Fig. 3.3):

$$\begin{aligned} Y^I &= (\chi^I + \varepsilon^I_{\text{temporal}})Z^I + E^I_{\text{temporo-spatial}}, \\ \chi^I &= (\chi^I_1, ..., \chi^I_P), \quad Z^I = \begin{pmatrix} Z^I_1 \\ \vdots \\ Z^I_P \end{pmatrix}. \end{aligned} \tag{30}$$

Here $\varepsilon^I_{\text{temporal}}(t)$ and $E^I_{\text{temporo-spatial}}(t)$ denote region-dependent temporal and temporo-spatial error terms of dimensions $T \times P$ and $T \times S$. This assumption could also have been used to define the term *pattern of interest*. As second assumption, this assumption has also been stated for GLM [50] (compare section 2.3.3) and is necessary for the application of a linear model such as GLM or ICA.

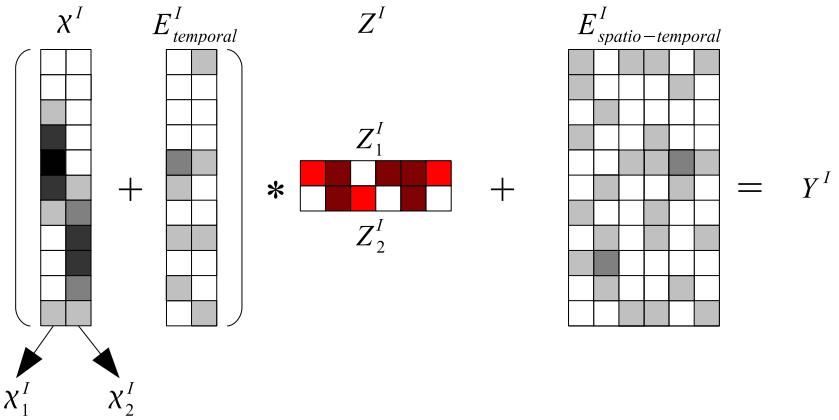

Figure 3.3: Pattern connectivity, third assumption. Example of a ROI I containing 2 POIs χ^I_1 and χ^I_2. Data matrix Y^I is the matrix product of the spatial activity distributions Z^I with their time courses χ^I plus noise terms.

However, concerning the concept of voxel-patterns, the linear model may not always be a sufficient approximation. Because neither the neuronal activity nor the measured BOLD response of a superposition of different stimuli (e.g. several colors, orientations, or other features at the same time) has to be the superposition of neuronal or BOLD activity of the single stimuli.

To circumvent this problem, conditions u^I_1, ..., u^I_P are additionally assumed to have no temporal overlap. This means, if for time t the onset $u^I_p(t) = 1$ then $u^I_q(t) = 0$ for all $p \neq q$ and $p, q = 1, ..., P$. For example, if there is a face presentation stimulus and a house presentation stimulus, which both evoke a pattern inside a ROI I, then there must not be a condition in which both stimuli are shown at the same time, because the resulting activation pattern in I will not be the linear superposition of the face and house patterns. This assumption can easily be met by accurate paradigm design and assures that the linear model assumption is valid.

Fourth assumption: For a ROI I, the spatial parts of all POIs Z_1^I, ..., Z_P^I are linearly independent and have the same norm:

$$|Z_1^I|_2 = \ ... \ = |Z_P^I|_2 \tag{31}$$

So two different POIs have to evoke indeed different spatial activation patterns and do not only lead to a stronger activation of the whole region. This assumption is necessary because ICA is scaling invariant and in general one can not be sure how different components are scaled relative to each other. One can normalize all spatial components to the same constant (I choose 1) and together with assumption two, temporal components are no longer invariant in the terms of scaling. Now the scaling factor (fourth assumption) and its sign (second assumption) are well-defined.

The limitations of this assumption lie in the neurophysiological foundations of the patterns of interest. In section 2.3.1 I gave examples of different spatial activation patterns which are linear independent and as small variations of patterns of many voxels can be assumed to have approximately the same norm [59] [62]. A higher spatial resolution of the functional MR images increases the distinguishability of the patterns.

3.1.3 Pattern selection

To obtain suitable pattern time courses for connectivity, one has three selection steps. Firstly, a decomposition algorithm has to be chosen, which in the present thesis is independent component analysis in the form of sJADE, tJADE, and stJADE described in section 2.3.5. Secondly, parameters of the decomposition method have to be adjusted to subject and ROI. For all three of the ICA algorithms e.g. the number of extracted components P^{ICA} is a free parameter. Thirdly, after a ROI was decomposed using the selected algorithm with its adjusted parameters, the components associated to the desired pattern have to be selected. For example, sJADE extracted 12 independent components, which was the optimal adjusted number of components for this ROI, one has to identify e.g. two components associated to two patterns desired for connectivity analysis. In this section adjustment of decomposition parameters and component selection are introduced.

Let I be a ROI, known to contain P_I patterns, whose temporal behaviors are desired to be known for connectivity analysis. For each of these patterns, an onset function $u_p^I : \mathbb{R}_0^+ \to \{0,1\}$ ($p = 1, ..., P_I$) which is known to evoke the pattern Z_p^I ($p = 1, ..., P_I$) in I, was specified by the experimentator. Decomposing an area I with ICA into P_I^{ICA} patterns gives a matrix decomposition

$$Y^I = X^I C^I, \tag{32}$$

where X^I contains temporal and C^I spatial components, which, depending on the used ICA approach (see section 2.3.5), are stochastically independent from each other.

Now the spatial and temporal parts Z_p^I, χ_p^I of the POIs can be approximated with spatial $C_{\pi(p)}^I$ (row of C^I) and temporal components $X_{\pi(p)}^I$ (column of X^I) respectively of the ICA decomposition in Eq. 32. These corresponding components are denoted *components of interest* (COI). The map π between index sets

$$\pi : \{1, ..., P_I\} \to \{1, ..., P_I^{\text{ICA}}\} \tag{33}$$

gives the column index of X^I for each pattern of interest. Thereby π represents the mapping between POIs and COIs indices. For a better overview, region dependencies of this transformation are omitted and I simply write π instead of π^I.

The relation between patterns of interest and components of interest is as follows: Patterns of interest are the unknown (real) patterns inside certain brain areas of the measured fMRI data between which one wants to analyse connectivity evoked by specific onsets. After the fMRI measurement and the definition of individual ROIs, the components of interest are selected from ICA decompositions of these ROIs and further used as approximations for the patterns of interest to study their connectivity.

Linear independence of the patterns of interest (fourth assumption) and their non-overlapping time courses (third assumption) guarantees a substantial degree of spatial and temporal independence and hence are necessary conditions that ICA can find and distinguish the patterns. Fig. 3.4 shows an example illustrating POIs and COIs with two regions of interest.

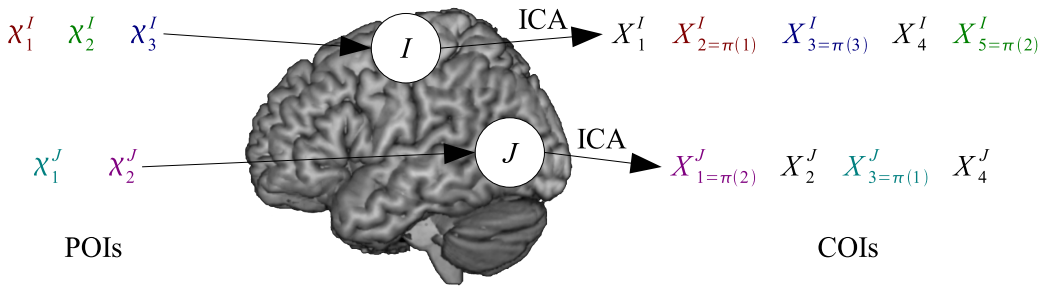

Figure 3.4: Scheme for POIs and COIs. Here, an example with two regions I and J containing $P_I = 3$ and $P_J = 2$ POIs is presented. Both were decomposed using ICA, extracting $P_I^{\text{ICA}} = 5$ and $P_J^{\text{ICA}} = 4$ components (right side). The components X_p^I and X_q^J with $p = 1, ..., 5$ and $q = 1, ..., 4$, on the right side of the figure, are the independent components estimated with ICA and one hopes to find components (color coded on the right side) corresponding to the color coded POIs χ_r^I on the left side of Fig. 3.4. The black components on the right represent extracted noise or artifact components. For example, here it is $\chi_1^J \approx X_{3=\pi(1)}^J$ with $\pi(1) = 3$.

As already stated, the major difficulty using ICA instead of PCA is the selection of corresponding COIs and the adjustment of ICA parameters. At this point it must be mentioned that some techniques to optimize ICA parameters, in particular the number of extracted components (e.g. [91] [103]), have already been developed. However, in general this is not the case for all parameters (e.g. α for stJADE) and one has no optimization algorithm for an arbitrary parameter of a decomposition method. Therefore I solved this problem in a more generic way.

In general, I expect the ICA algorithm to have $A > 0$ free parameters $a = (a^1, ..., a^A)$ with parameter spaces $a \in \Lambda = \Lambda_1 \times ... \times \Lambda_A$. Components given by ICA decomposition using parameters a are denoted with:

$$Y^I = X^I(a)C^I(a). \tag{34}$$

At first, I explain in which way a particular realization $a = (a^1, ..., a^A) \in \Lambda$ is better than another, and how an optimal parameter set can be estimated.

Intuitively for ROI I, a parameter set is good if, for the temporal part of each pattern of interest χ_p^I ($p = 1, ..., P_I$), the ICA decomposition of I yields a temporal pattern X_q^I that is related to it. Using the correlation between extracted components and HRF onset functions associated to the desired POIs, I can define the *decomposition fitness function* F of a parameter set $a \in \Lambda$ as

$$F : \Lambda \to [0,1], \quad F(a) := \sqrt[P_I]{\prod_{p=1}^{P_I} \max_{q=1,\ ...,\ P_I^{\mathrm{ICA}}} |r_{X_q^I, \tilde{u}_p^I}|}. \tag{35}$$

The well known empirical correlation $r_{x,y} \in [-1,1]$ between equally sized samples x and y was defined in section 2.2.1 Form. 10. One sees that F is maximal if for all POIs χ_p^I, a component X_q^I can be found, so that both are highly correlated. The absolute value in Form. 35 of the correlation is used because ICA is sign invariant. Due to the second assumption from section 3.1.2, I know that POIs and COIs have to be positively correlated. This fact can now be used to determine a COI's sign. The p-th root normalizes the product. This fitness function was used to adjust parameters a for each subject and region.

In the example of a ROI I with only one pattern, $P_I = 1$, decomposed using stJADE, Form. 35 simplifies to

$$F : \mathbb{N} \times [0,1] \to [0,1], \quad F(P_I^{\mathrm{stJADE}}, \alpha) = \max_{q=1,\ ...,\ P_I^{\mathrm{stJADE}}} |r_{X_q^I, \tilde{u}_1^I}|. \tag{36}$$

Here, a parameter set a, providing the component with the maximum correlation with the HRF onset function u_1^I of the single POI, would be optimal.

The parameter space Λ was systematically sampled to see how F depends on the single parameters. For stJADE, for example, I used $a^1 = P_I^{\mathrm{stJADE}} = 2, 3, ..., 20$ and $a^2 = \alpha = 0.0, 0.05, ..., 1.0$.

Due to different hemodynamic response functions and local artifacts for different regions, I also expect the estimated adjusted parameters to vary between ROIs and participants.

For a region I, let $a_{I,\mathrm{opt}} = (a_{I,\mathrm{opt}}^1, ..., a_{I,\mathrm{opt}}^A)$ denote the estimated optimal set of ICA parameters, where $a_{I,\mathrm{opt}}^1 = P_I^{\mathrm{ICA}}$ is the number of extracted independent components.

Finally, the P_I components representing patterns of interest (POIs) are selected from the extracted P_I^{ICA} ICA components. Again Pearson's correlation between components and HRF onset functions associated to POIs is used as a measure for relatedness. For each $p = 1, ..., P_I$, the component $X_{\pi(p)}^I(a_{I,\mathrm{opt}})$ out of the P_I^{ICA} independent components, having the highest correlation with the HRF onset function $\tilde{u}_p^I$, is selected as COI, approximating χ_p^I.

$$\pi(p) := \underset{q=1,...,P_I^{ICA}}{\arg\max} \left| r_{X_q^I(a_{I,\mathrm{opt}}), \tilde{u}_p^I} \right| \tag{37}$$

As introduced above, I omitted the region dependency for the mapping between POI and COI indices and simply wrote π instead of π^I.

The COI $X^I_{\pi(p)}(a_{I,\text{opt}})$ can be interpreted as the time course of the multi-voxel pattern associated with condition u^I_p. The selected COIs

$$X^I_{\pi(1)}(a_{I,\text{opt}}),\ ...,\ X^I_{\pi(P_I)}(a_{I,\text{opt}}), \tag{38}$$

replace the single first PCA component and can be used for further connectivity analysis.

Let $I_1, ..., I_N$ be the regions of interest, each containing P_{I_i} $(i = 1, ..., N)$ patterns of interest. In general, a connectivity measure K (e.g. restricted correlation or a parameter of a dynammic causal model) depends on all $\sum_{i=1}^{I_N} P_{I_i}$ COIs:

$$K = K(X^{I_1}_{\pi(1)},...,X^{I_1}_{\pi(P_{I_1})},\ ...\ ,X^{I_N}_{\pi(1)},...,X^{I_N}_{\pi(P_{I_N})})\ \in \mathbb{R}\,. \tag{39}$$

Here, dependence of the index mapping π on the region of interest was omitted, and for a better overview also the dependence of a connectivity measure K on all COIs is not written out.

Before discussing a major problem arising with the proposed method of component selection, a summary of the method of pattern connectivity is given in Fig. 3.5 and in more detail here:

1. Step: Question / Hypothesis Firstly, one has to state a clear question or hypothesis concerning the connectivity between specific brain areas during specific experimental conditions. One has to know which ROIs are involved and how many POIs each region contains and through which experimental condition these POIs are evoked. For this purpose, previous findings from literature are used.

Furthermore, the experimental design has to be specified. One has to implement suitable stimuli for the POIs and the later localization of the ROIs. The number of trials per condition has to be defined so that enough data is obtained for reliable analysis afterwards. However, the experiment must not be too long, because participants will show exhaustion effects that limit the duration of one scanning session to about one hour. Depending on the initial question, many other aspects of paradigm design may be of interest.

The exclamation marks in the Fig. 3.5 denote information one has to know a-priori. For this example, $P_I = 1$ and $P_J = 2$ patterns of interest were chosen for regions I and J respectively.

2. Step: Carry out experiment Now, it is possible to perform the experiment with an fMRI scanner. Important issues arising for the measurement are a suitable TR ($\leq$ 3 s for connectivity studies, to cover the slope of the HRF), a sufficient spatial covering of the brain in particular of the regions of interest, a high spatial resolution of the functional scans so that patterns can be distinguished, and that each subject gets the same task instructions in the beginning reducing inter-subject variations.

1. Step: Question / Hypothesis

Which ROIs are involved? Which onsets evoke POIs in which ROIs? Experimental design?

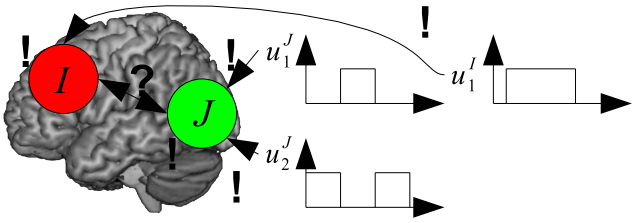

2. Step: Carry out experiment

Measurement of functional, structural, and behavioral data.

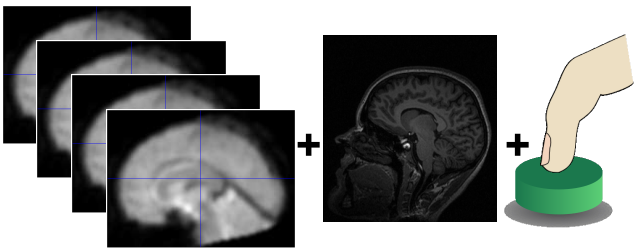

3. Step: Preprocessing

4. Step: ROI definition

Define position, form, and size for each ROI and subject.

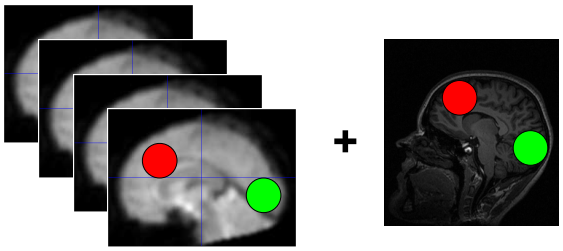

5. Step: Pattern selection I

For each ROI, estimate ICA parameter set $a_{I,opt}$ for best decomposition using proposed fitness function.

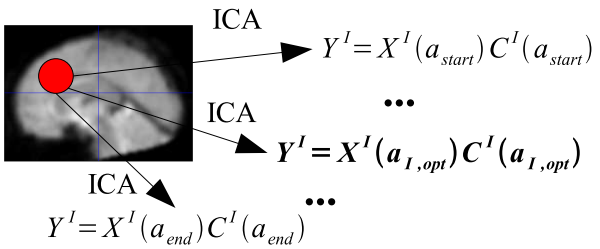

6. Step: Pattern selection II

For each ROI, select COIs using the optimal decomposition.

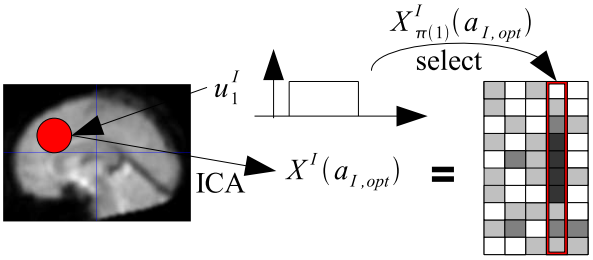

7. Step: Study Connectivity

Study connectivity between the COIs of all regions.

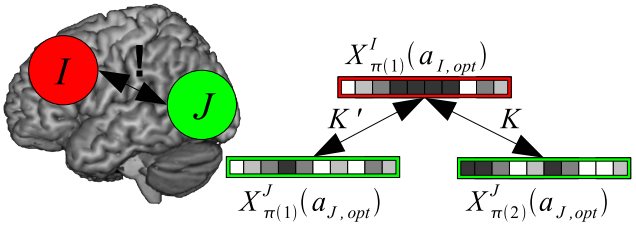

Figure 3.5: Scheme of pattern connectivity.

3. Step: Preprocessing Several preprocessing steps have to be carried out to prepare the data for further analysis. For details, see chapter 2.1.3.

4. Step: ROI definition Individual positions for regions of interest have to be defined for each subject. Therefore, I use GLM contrasts (compare chapter 2.3.3 for GLM theory and 3.2.2 and 3.3.4 for its application) combined with a-priori knowledge of the raw position of each region. In addition, size and form of a ROI have to be defined giving a voxel index set for each ROI.

5. Step: Pattern selection I Now it is possible to use ICA to decompose the data-matrices Y^I and Y^J. As proposed above, one computes ICA for various parameter sets $a \in \Lambda$, which sample the parameter space Λ in an accurate manner and use the proposed fitness function F to select the optimal parameter sets $a_{I,\text{opt}}$ and $a_{J,\text{opt}}$ for both regions separately.

6. Step: Pattern selection II Having the optimal ICA decompositions, one selects components of interest taking the extracted component which shows the highest correlation with the HRF onset function $\tilde{u}$ associated with onset u as COI.

7. Step: Study connectivity The selected COIs can now be used for further connectivity analysis from simple correlation analysis between the components to the point of using them as time courses for dynamic causal models. In Fig. 3.5, two connectivity measures, K and K', are shown, describing the connectivity between the three COIs.

Only steps 4, 5, and 6 differ between the standard PCA and the pattern connectivity method. In step 7, I then use the first principal components or the selected COIs for further connectivity analysis, for the state of the art method or pattern connectivity respectively.

The details of all these steps differ for miscellaneous initial issues about connectivity. For two fMRI studies, I will describe these details later, closely following the steps above. But first, a major problem arising with decomposition's parameter adjustment and component selection must be addressed.

3.1.4 Statistical connectivity baseline caused by component selection

Due to the relation of onsets to each other, the selection of components by their correlation to conditions leads to a methodical artifact in the relation between extracted components.

For example, if I consider two randomly positioned regions I, J and two conditions u_1^I, u_1^J correlated with each other (see Fig. 3.6). Now I hypothesize that u_1^I evokes a pattern inside I and u_1^J in J respectively and that those two patterns are connected with each other, meaning that their time courses are correlated. Because the ROIs were positioned randomly, ICA decomposition will give independent but in general not experimentally related components, which by accident may be correlated with conditions anyway. Now following the approach of pattern selection proposed above and choosing (from all extracted independent components for I) the component that shows the highest correlation with $\tilde{u}_1^I$ (respectively for J) I will of course find a correlation between the two selected components. In the extreme case, where one is interested in the connectivity between two regions during one particular condition $u_1^I = u_1^J$, one finds the two selected components with highest correlation to $\tilde{u}_1^I$ also to be correlated with each other. So one finds connectivity between arbitrary-positioned ROIs for all experimental onsets u, which is not desired.

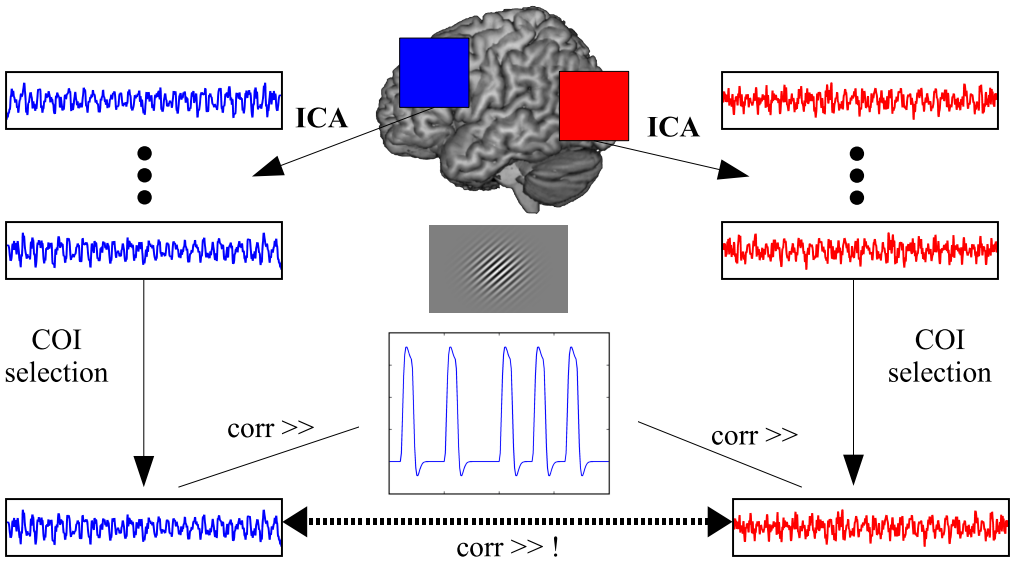

Figure 3.6: Pattern selection gives correlated patterns. Example of two ROIs each containing one COI related to an 45° Gabor patch stimulus. For both regions, ICA decompositions are computed and one COI, which is highly correlated with the presentation of the stimulus, is selected for each ROI. One also expects the extracted COIs to be correlated with each other.

I will describe two approaches to circumvent this methodical artifact: The first aims to estimate a statistic connectivity baseline, which can be accounted for in later analysis, whereas the second method uses only a part of the data for component selection, and the remaining part for connectivity analysis, thus eliminating the random effects causing the baseline.

Estimation of the component selection connectivity baseline: For a connectivity measure (e.g. correlation between two patterns or an estimated DCM parameter, also compare section 2.2), I will denote the statistically expected value of the connectivity measure for selected components from randomly positioned ROIs as *component selection connectivity baseline* (CSCB) of the connectivity measure. Randomly positioned regions must have the same size (number of voxels) and form as the regions of interest.

To estimate the CSCB, I compute the connectivity measure several times for randomly positioned regions, extract and select COIs as proposed above, and build the mean of the resulting connectivity measures, which by definition is the empirical CSCB.

Considering, for example, the situation of Fig. 3.6 and the connectivity measure K to be the correlation of two selected COIs $X^I_{\pi(1)}$ and $X^J_{\pi(1)}$:

$$K = r_{X^I_{\pi(1)}, X^J_{\pi(1)}}. \tag{40}$$

Regions I and J shall be previously defined areas, which I think should be functionally connected. Because COIs $X^I_{\pi(1)}$ and $X^J_{\pi(1)}$ could be components which are accidently correlated with the corresponding HRFs, it is not sufficient to find $K > 0$ to reason that I and J are funcionally connected. One has to show that $K > \mathrm{CSCB}_K$.

In general, for a connectivity measure K, the component selection connectivity baseline CSCB_K can be estimated by repeatedly computing K for randomly positioned regions and taking the mean of these K. Decomposition's parameter adjustment and COI selection have to be performed for each repetition separately. Assuming N repetitions with computed connectivity measures K_1, ..., K_N, CSCB_K is estimated as:

$$\mathrm{CSCB}_K \approx \frac{1}{N} \sum_{i=1}^{N} K_i. \tag{41}$$

The interpretation of the CSCB is very intuitive. Faced with a connectivity result of any kind for defined ROIs and selected COIs, I can estimate the CSCB, which states the connectivity result statistically to-be-expected for random areas, and compare with the K obtained from ROIs. Only if K significantly differs from CSCB_K one can interpret it as a considerable connectivity between ROIs.

Due to the fact that one has to compute many ICA decompositions for each randomly positioned region, the number of repetitions N, is limited by computation time. For advanced connectivity analysis methods, such as dynamic causal modeling (compare section 2.2.2) this computation may be a very time consuming task.

Separately selected components: Besides estimating the CSCB, one can try to separate the data that underlies component selection steps (steps 5 and 6 in figure 3.5) from the data used in connectivity analysis step (step 7). For this, I assume, without loss of generality, that the number of measured scans T is even. After step 4 of ROI definition (compare figure 3.5), I compute ICA decompositions on the basis of the entire data but use only the first 1, ..., $T/2$ scans for parameter

and component selection steps 5 and 6 and the last $T/2+1$, ..., T scans of those selected COIs for connectivity analysis or vice versa. Figure 3.7 illustrates an ICA decomposition, and further usage of the data for component selection and connectivity analysis.

An even more elegant way would be to use bootstrapping techniques [38] to sample a training subset of scans and determine optimal ICA parameters and select COIs from this training set. This way, remaining test scans could be used for connectivity analysis. Repeating those two steps and analyzing the distributions of the single connectivity results over bootstrap iterations one would obtain more reliable results. However, this may not be applicable for connectivity analysis techniques, which explicitly model the HRF response, such as, for example, DCM. Those methods need the temporal information and dependences between succeeding scans, which is destroyed through bootstrapping. Because I will use DCM, I will leave it at mentioning this possibility.

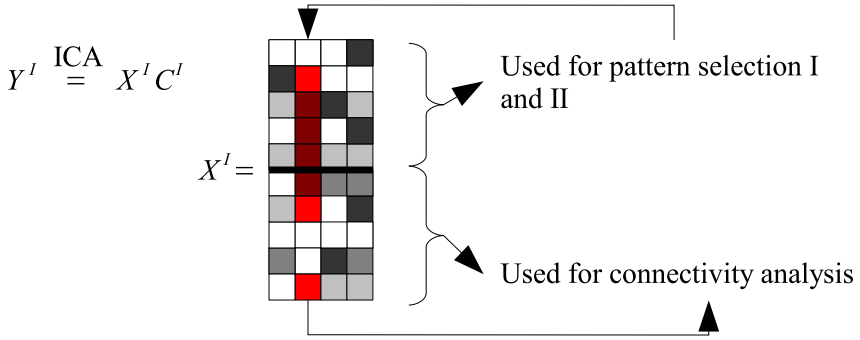

Figure 3.7: Illustration for separate component selection. After ICA decomposition of data Y^I, only the first half $(x^I_{ij})_{i=1..T/2,j=1..P}$ of matrix X^I is used to compute the fitness function F, determine optimal ICA parameters $a \in \Lambda$, and select COIs. After this, the second half of these selected COIs is used for connectivity analysis.

Here, I will always use three separated analyses. For the first one, I use the whole data to select ICA components and analyze connectivity between COIs also selected on the basis of all scans. For the second and third one, I use the proposed data split: applying ICA on the whole, selecting COIs on the basis of the first (second) half of data, and analyze connectivity for the second (first) half of scans.

So, if the found results for the first analysis are from the same magnitude as their CSCB, I can say that they are caused by component selection, and have no neurophysiological meaning. In addition, results can be excluded where the three analysis methods (using the whole data, the first, or second part for COI selection) significantly differ from each other, because this would mean that COIs selected on only one half of the data, lead to inconsistent connectivity results. Cases, where results from the split data are consistent upon each other but differ from results found with all data, might be caused by the insufficient amount of scans for the split data. I assume that temporal effects, which may change connectivity between first and second half of the experiment, such as for example learning or exhaustion, are small compared to the connectivity under investigation. Both approaches, comparing connectivity measures of specific ROIs with their CSCB and with connectivity measures obtained for the splitted data, can be used separately

to determine if found connectivity results are caused by the methodical artifact introduced through the pattern selection step or not.

3.2 I. Paradigm: Validation of pattern connectivity

After introducing the idea of pattern connectivity and the basic theory behind, I present the first fMRI study, whose aim was to compare pattern connectivity with the common PCA method, and to show that both methods yield the same connectivity results.

In the following, I proceed as outlined in Fig. 3.5. I begin by stating the connectivity hypothesis, including involved regions of interest, patterns of interest, and their related conditions. Also the details of experimental setups, a description of the used stimuli, and trial composition is explained in the following chapters.

3.2.1 Experimental setup and hypothesis

Because in the first experiment I want to compare connectivity measures obtained with the PCA method with those obtained with pattern connectivity, the experiment had to be chosen to only evoke one pattern of interest in each ROI, so that the PCA method was also applicable. Accordingly I chose to study connectivity between two regions inside the visual cortex: the region around the primary visual cortex (V1) and the visual area MT+ (middle temporal) also called V5, which consists of the subareas MT and MST (see [72] Fig. 6 or [82] for detailed investigation of are MT/V5). Whereas area V1 and its adjacent areas V2, V3, and V4 are involved in procession of almost all features of visual stimuli as ocular dominance, orientation, spatial frequency, size, color, and shape [66] [67] [5], the visual area MT+ mainly processes the motion attributes of stimuli.

Together, the areas V1, V2, V3, V4, and V5 form the visual cortex. Although there are methods to separate V1 from the nearby areas V2 and V3 and to distinguish between MT and MST, this is not in the scope of this work. I will refer to the union of V1, V2, and V3 as the visual area (VA) and to MT+ as the motion area (MA). See Fig. 3.8 for a raw localization of ROIs VA and MA taken from [72] Fig. 6 and [161] Fig. 1.

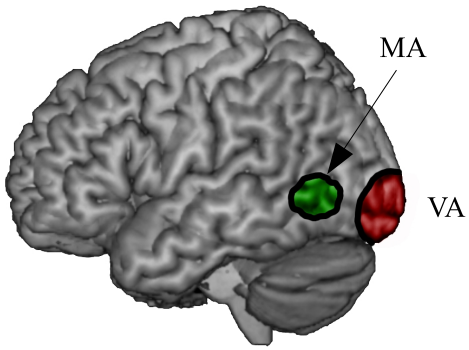

Figure 3.8: Regions of interest for the BMS paradigm. Regions of interest MA (green) and VA (red) are framed black.

Many studies have been conducted to investigate functional properties of the visual cortex (e.g. [170] [42] concerning the visual area MT in monkeys and [163] in humans). Of interest for us is the connectivity between VA and MA (for detailed information about those two areas and their connectivity see [90] [45]). Most

importantly MA gets its major input from VA (in particular V1 [15]). The connectivity between these areas has already been used to introduce dynamic causal modeling [49], and I used this simple network of the two areas VA and MA both containing only one POI, to compare pattern connectivity with the standard PCA method.

To evoke neuronal activation in MA, participants have to perceive a moving stimulus. Alternating expanding and contracting (1 Hz) flow fields of spheres have shown [72] to generate strong responses in MA. I will call this condition of a flowfield (20° diameter) consisting of randomly distributed gray spheres the motion condition (M). For more detailed information on the stimuli, refer to [72]. Because this stimulus will also lead to a strong response in VA one needs an additional stimulus that excites VA in a similar way but not MA to distinguish between VA and MA, and to determine individual positions. For this condition, denoted as the stationary condition (S), I choose the same distribution of gray (but now stationary) spheres. Finally, a baseline condition (B) was added, in which no spheres were presented. To facilitate necessary fixation during the whole experiment a small fixation cross was shown across all three conditions.

Due to the nature of its stimuli I will refer to this first experiment as the blank-motion-static paradigm (short BMS). The stimuli were presented in a block design using pseudo-randomized blocks of 20s duration (compare Fig. 3.9). The whole experiment took about 30 min and resulted in 910 functional MR scans per subject. Participants had only to pay attention to the visual stimulation and maintain fixation.

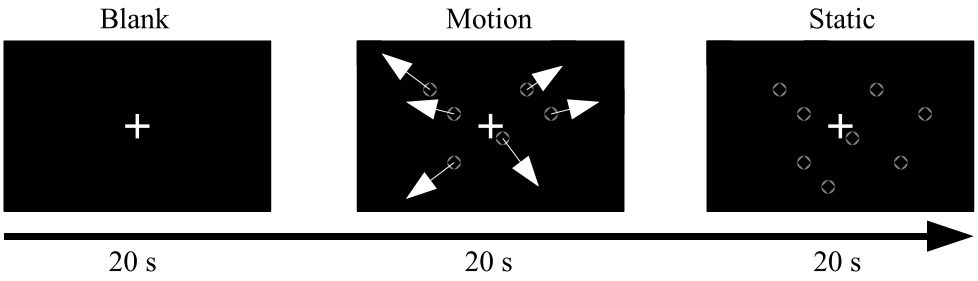

Figure 3.9: Design of the BMS experiment and illustration of BMS stimuli. Blank, motion, and static stimuli (from left to right) were presented ,pseudorandomized, for intervals of 20 s.

For simplicity, the voxel index sets associated with the ROIs VA and MA are denoted in the same way as VA and MA. The onsets of the blank, motion, and static conditions will be denoted as u_1, u_2, and u_3 respectively. I will denote the combination of onsets u_2 and u_3 the visual or stimulus onset $u_4 := u_2 + u_3$. Region VA contains one POI (pattern of interest) χ_1^{VA}, Z_1^{VA} related to the visual onset $u_1^{\mathrm{VA}} = u_4$. I remind the reader that $\tilde{u}_1^{\mathrm{VA}}$ was called the HRF onset function associated with area VA. Finally, region MA contains the pattern of interest χ_1^{MA}, Z_1^{MA} associated to the HRF onset function $\tilde{u}_1^{\mathrm{MA}} = \tilde{u}_2$ of the motion stimulus.

For pattern connectivity, associated COIs (components of interest) $X_{\pi(1)}^{\mathrm{VA}}, C_{\pi(1)}^{\mathrm{VA}}$ and $X_{\pi(1)}^{\mathrm{MA}}, C_{\pi(1)}^{\mathrm{VA}}$ were selected from ICA decomposotions using the adjusted ICA

parameters and following sections 3.1.3 and 3.1.4. For the standard PCA method, the PCA decomposition of the two regions was computed and the first component was selected as COI.

The hypothesis is that activation between VA and MA (in particular between their COIs) increases during the motion condition, relative to the static condition. As mentioned before, restricted correlation and dynamic causal modeling were used to verify this hypothesis.

Measuring functional connectivity, I hypothesize that the two selected components of interest show higher correlation during the motion condition than during the static condition. In terms of restricted correlation this means that correlation between $X^{\mathrm{VA}}_{\pi(1)}$ and $X^{\mathrm{MA}}_{\pi(1)}$ restricted to the motion condition u_2 is higher than correlation restricted to the static condition u_3:

$$r_{X^{\mathrm{VA}}_{\pi(1)},X^{\mathrm{MA}}_{\pi(1)}}\Big|_{u_2} > r_{X^{\mathrm{VA}}_{\pi(1)},X^{\mathrm{MA}}_{\pi(1)}}\Big|_{u_3}. \tag{42}$$

In terms of the component selection connectivity baseline (CSCB) introduced in section 3.1.4, this hypothesis becomes:

$$\Delta := r_{X^{\mathrm{VA}}_{\pi(1)},X^{\mathrm{MA}}_{\pi(1)}}\Big|_{u_2} - r_{X^{\mathrm{VA}}_{\pi(1)},X^{\mathrm{MA}}_{\pi(1)}}\Big|_{u_3} > \mathrm{CSCB}_{\Delta}, \tag{43}$$

where CSCB_{Δ} is the mean difference of restricted correlations computed for randomly positioned regions. Same notations as introduced in sections 2.2.1 and 3.1.4 are used.

Similar as for the restricted empirical correlation, I hypothesize for DCM a connection between COIs $X^{\mathrm{VA}}_{\pi(1)}$ and $X^{\mathrm{MA}}_{\pi(1)}$, which increases during motion stimulation (compare Fig. 3.10).

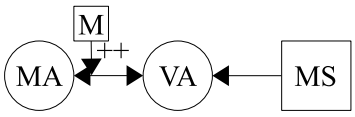

Figure 3.10: A-priori hypothesized dynamic causal model. Here a scheme for the hypothesized network is presented. ROIs are shown as circles and external inputs and modulators as squares. The visual stimulation (union of motion and static stimuli; MS) excites region VA, which transfers information to region MA. This bottom-up connection is modulated (M) by the motion regressor.

To test this hypothesis, four additional DCM-models representing different connectivity structures were estimated. All models were compared pairwise and the hierarchy between models was determined as introduced in section 2.2.2. The stated hypothesis is verified, if models which show a strong and positive motion modulation from the VA COI to the MA COI achieve better rankings (lower rank) in the model hierarchy than models that lack this modulation or show only weak or negative modulation strengths.

Four healthy volunteers (3 male, 1 female, aged $21 - 28$ years) participated in the BMS experiment. All were familiarized with the experimental tasks before

the fMRI scan session. All participants had normal or corrected-to-normal vision and none had a history of neurological or psychiatric illness. FMRI data was preprocessed using the algorithms previously described in chapter 2.1.3.

3.2.2 Region of interest definition

In this section I explain how the voxel index sets VA and MA of the regions were chosen and localized for later analysis.

The SPM5 toolbox was used to specify and estimate a General Linear Model (compare section 2.3.3) consisting of the three experimental onsets u_1, u_2, and u_3. For the localization of VA the contrast $c_{\mathrm{VA}} = (-1, 0.5, 0.5)$ was used. A high t-value of a voxel in the resulting statistical map means that this voxel showed a higher activation during visual stimulation (motion and static together) than during the blank condition. To determine individual positions of MA contrast vector $c_{\mathrm{MA}} = (0, 1, -1)$ was used. In this case voxels showing a high activation during the motion condition relative to the static condition had high t-values.

To improve visualization I estimated two GLMs for each participant. One was computed using raw not normalizied and unsmoothed data, and a second using normalized and smoothed data. Beside these two, I present the afterward normalized results obtained from the raw data to demonstrate the spatial smoothing effects of the normalization step. Fig.s 3.11 and 3.12 show t-value images in (a), (c), and (d) for the two contrasts c_{VA} and c_{MA} respectively and the specified individual ROIs in (b). Thereby voxels with $p < 0.0001$ ($T > 3.7$) are plottet, color coded, over the associated structural scan (gray background). Spatial smoothing due to normalization can be seen by comparing (a) and (c). Images for participants 1, 3, and 4 can be found in the appendix 5.1 Fig. 5.1, 5.2, and 5.3.

ROI coordinates were determined for each subject separately. Individual positioned ROIs for VA and MA were defined based on the GLM peak activations obtained from the contrasts c_{VA} and c_{MA} of the raw data. The positions were additionally transformed to MNI space using the SPM5 implemented normalization algorithm [100] for visualization and comparison purpose.

All voxels in a sphere with radius 8 mm around a ROI's position were taken to form the index sets VA and MA (see Figs. 3.11 b) and 3.12 b)). Thereby the raw non-normalized and spatially non-smoothed data was taken as a basis. For subject 2 Figs. 3.11 and 3.12 show GLM results and the defined ROI.

Table 2 shows t-values of peak voxels from the raw data and their normalized location in MNI space. Areas' positions are comparable to those reported in other studies as, for example, [162] [72] [161]. For all participants, peak voxels for both regions show high significance ($p < 0.0001$).

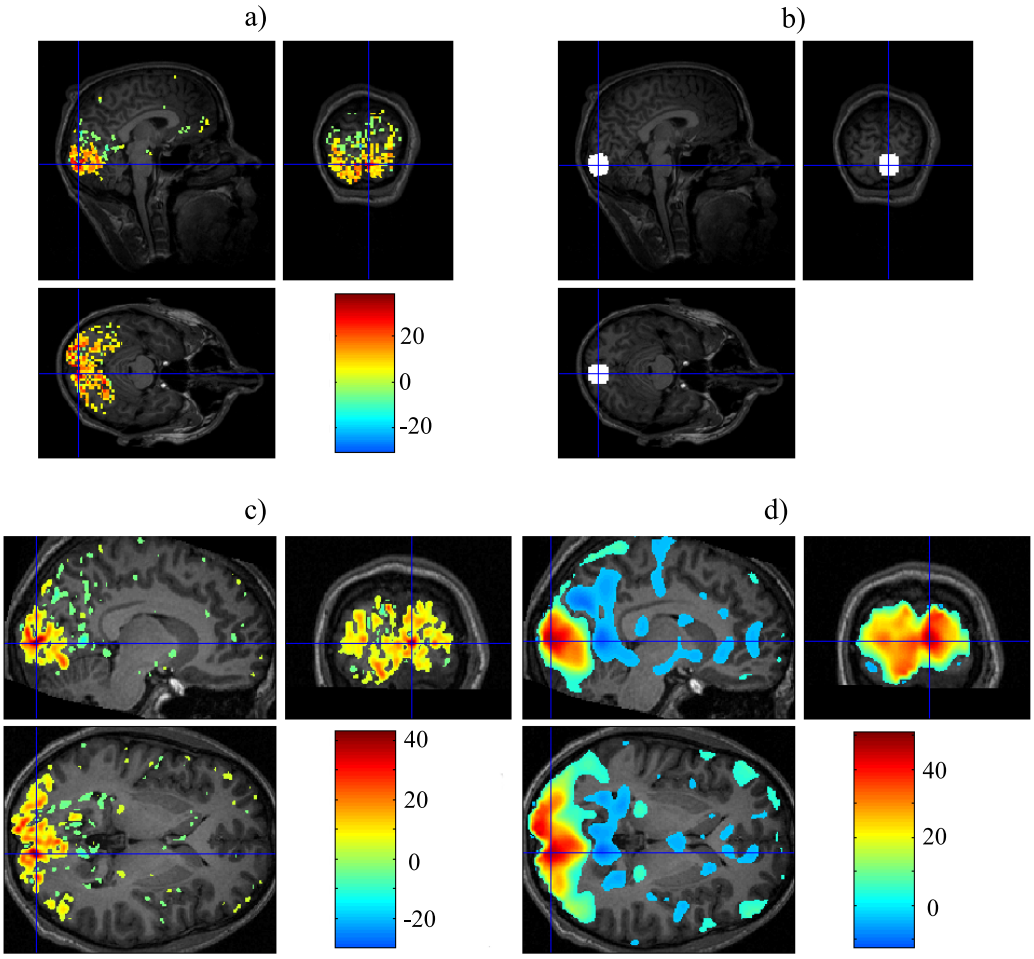

Figure 3.11: SPM of GLM contrast c_{VA} for subject 2. In all four images the presented data was laid over the structural scan (not normalized for a) and b), normalized for c) and d)). In a), c), and d) all voxels with $p < 0.0001$ ($T > 3.7$) with respect to the GLM contrast c_{VA} are shown color coded according to their t-values. Thereby also voxels with negative t-values (below -3.7) are presented. In a) the raw data after slicetiming and realignment preprocessing steps was taken as a basis whereas in c) the data was also normalized to the MNI brain. d) shows the result for the GLM of normalized and smoothed (gaussian kernel of 8 mm) data. In b) voxels of the depicted slice belonging to the ROI VA are colored white.

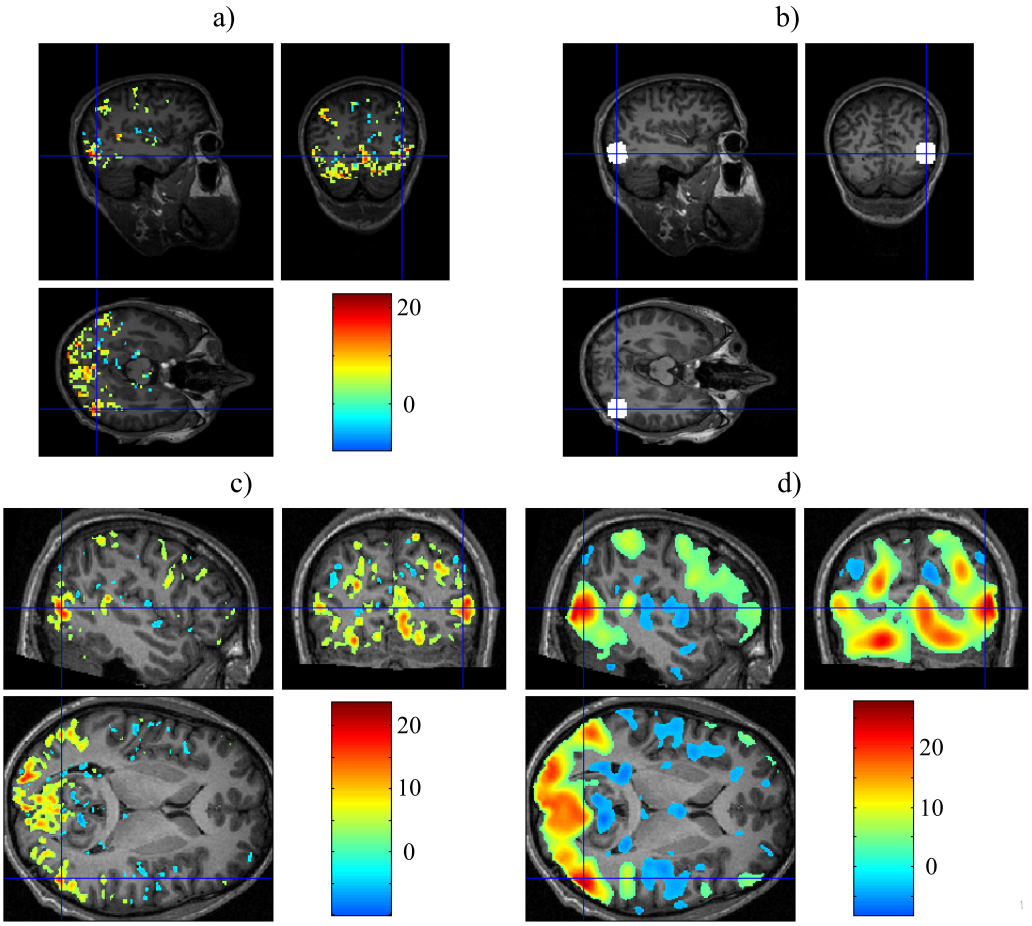

Figure 3.12: SPM of GLM contrast c_{MA} for subject 2. Here the same images as in Fig. 3.11 are presented for area MA.

ROI	voxels	t-value (raw)	MNI coordinates		
VA (S1)	251	44.38	−10	−91	−3
VA (S2)	251	37.84	9	−93	3
VA (S3)	253	53.81	−4	−82	0
VA (S4)	255	48.05	−5	−94	−3
MA (S1)	251	23.96	49	−67	2
MA (S2)	251	16.64	49	−72	6
MA (S3)	253	21.93	45	−64	0
MA (S4)	255	25.93	45	−64	−5

Table 2: ROI information for the BMS paradigm. The table presents the number of voxels, t-value of central ROI voxel, and MNI coordinates of the two regions VA and MA for all four subjects S1 to S4.

3.2.3 Component selection

As stated earlier in chapter 2.3.5, I will use ICA methods sJADE, tJADE, and stJADE for the estimation of the decomposition of data matrices Y^{VA} and Y^{MA} (see Equation 44 below). Whereas the number of extracted components P is a free parameter for all three algorithms, stJADE has the temporo-spatial weighting parameter α as a second free parameter (compare chapter 2.3.5). As stated in section 3.1.4, decompositions were computed for several free parameter sets sampling the associated parameter space Λ for each ICA algorithm accurately. For sJADE and tJADE decompositions for $P = 2, ..., 20$ components and for stJADE for $(P,\alpha) \in \{2, ..., 20\} \times \{0.00, 0.05, 0.1, ..., 0.95, 1.00\}$ were computed. In addition the PCA decomposition (see section 2.3.4) was estimated for each region.

$$Y^{\mathrm{VA}} = X^{\mathrm{VA}}(a)C^{\mathrm{VA}}(a), \quad Y^{\mathrm{MA}} = X^{\mathrm{MA}}(a)C^{\mathrm{MA}}(a) \tag{44}$$

In Eq. 44 the dependence on the used ICA algorithm, sJADE, tJADE, or stJADE, are omitted. For each extracted component of region VA, its correlation with the visual stimulus onset HRF $\tilde{u}_1^{\mathrm{VA}} = \tilde{u}_4$ was estimated. The same for region MA and the motion onset HRF $\tilde{u}_1^{\mathrm{MA}} = \tilde{u}_2$.

To find the best parameter set $a_{\mathrm{VA,opt}}$ and $a_{\mathrm{MA,opt}}$ for each ICA method I used the fitness function introduced in Eq. 35. Because VA and MA have only one COI, one gets

$$F_{\mathrm{VA}}(a) = \max_{p=1,\ ...,\ P} |r_{X_p^{\mathrm{VA}}(a),\tilde{u}_1^{\mathrm{VA}}}| \tag{45}$$

$$F_{\mathrm{MA}}(a) = \max_{p=1,\ ...,\ P} |r_{X_p^{\mathrm{MA}}(a),\tilde{u}_1^{\mathrm{MA}}}|. \tag{46}$$

For sJADE and tJADE it is $a = P$ and for stJADE $a = (P,\alpha)$ with $P = 2, ..., 20$ and $\alpha = 0.00, 0.05, ..., 1.00$. Table 3 shows computed maximum correlations and parameters $a_{\mathrm{VA,opt}}$ and $a_{\mathrm{MA,opt}}$, for which this maximal correlation is achieved. For PCA this is the component number in the single PCA decomposition with maximum correlation.

One sees that for PCA, always the first, most variance explaining component also has the highest correlation with the onset HRF (compare also Fig. 3.13). However, for ICA methods one always has to extract more components P to achieve maximum correlation and therefore maximum fitness. In addition, one sees that correlations for ICA methods are almost always higher than for PCA.

Figs. 3.13 and 3.14 show the fitness function F for ICA methods over their parameter spaces Λ relative to the maximum correlation achieved with PCA. Because each region contains only one pattern, this maximum correlation is equal to the fitness function. One sees that for the two regions VA and MA decomposed with sJADE or tJADE, always a parameter P was found, which yields a decomposition containing a component that is equal or more highly correlated to $\tilde{u}_1^{\mathrm{VA}}$ ($\tilde{u}_1^{\mathrm{MA}}$) than all PCA components. This implies that ICA finds components, which show a more significant, in the sense of correlation, relation to the paradigm than PCA (compare [155]).

ROI	Decomp.	Subject 1	Subject 2	Subject 3	Subject 4
VA	PCA	0.83(1)	0.80(1)	0.80(1)	0.89(1)
	sJADE	0.84(12)	0.83(4)	0.84(9)	0.87(2)
	tJADE	0.83(2)	0.83(5)	0.83(7)	0.89(2)
	stJADE	0.84(2; 0.50)	0.83(6; 0.80)	0.83(9; 0.75)	0.85(2; 1.00)
MA	PCA	0.71(1)	0.78(1)	0.60(1)	0.81(1)
	sJADE	0.81(8)	0.83(3)	0.73(5)	0.89(7)
	tJADE	0.78(9)	0.79(2)	0.73(11)	0.87(3)
	stJADE	0.82(10; 0.80)	0.87(7; 0.00)	0.74(5; 1.00)	0.89(3; 0.20)

Table 3: Maximum of the fitness function. Maximum fitnesses, $F_{\mathrm{VA}}(a_{\mathrm{VA,opt}})$ and $F_{\mathrm{MA}}(a_{\mathrm{MA,opt}})$, and the optimal parameters, $a_{\mathrm{VA,opt}}$ and $a_{\mathrm{MA,opt}}$ (in brackets), for which this maximum correlation is achieved are shown for the two ROIs and the four decomposition algorithms. For PCA, the number in brackets indicates the component yielding maximum correlation. For stJADE, the optimal parameter contains also the weight α. Correlations for region VA (MA) were computed between components and HRF onset functions $\tilde{u}_1^{\mathrm{VA}}$ ($\tilde{u}_1^{\mathrm{MA}}$).

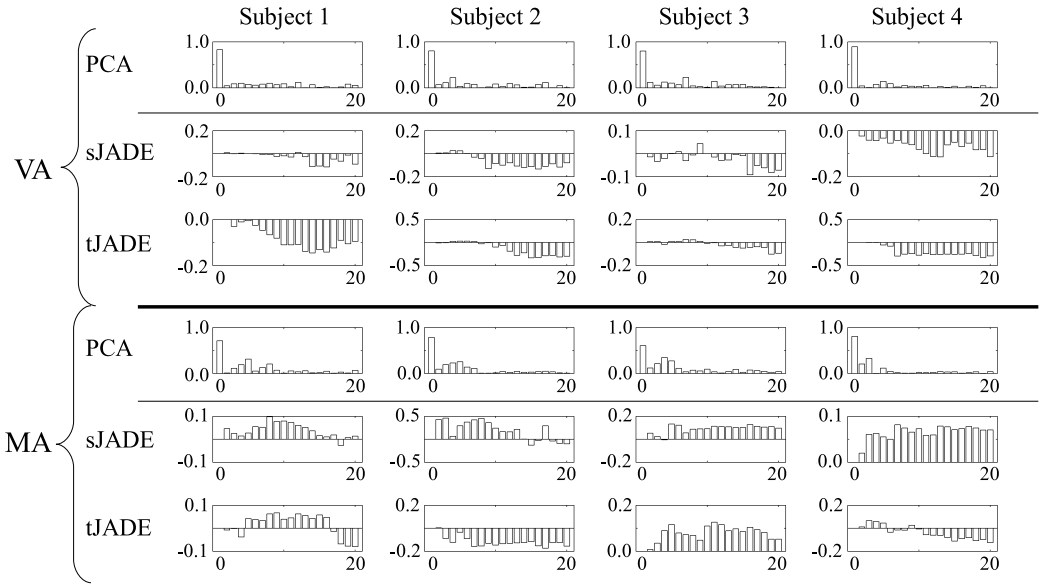

Figure 3.13: Fitness function F over parameter space Λ for sJADE and tJADE. For PCA (first and forth row of graphs) correlations between single PCA components and dependent on investigated ROI $\tilde{u}_1^{\mathrm{VA}}$ or $\tilde{u}_1^{\mathrm{MA}}$ for VA and MA respectively are presented. This is the same as the fitness function F for parameter $a = P$. The other rows show fitness functions (= maximal correlation) for sJADE and tJADE relative to a baseline of PCA's fitness, which was always realized for the first PCA component. The plotted value for a specific P in a graph, belonging to sJADE or tJADE, represents the maximum correlation over all P extracted components with the associated HRF onset functions $\tilde{u}_1^{\mathrm{VA}}$ ($\tilde{u}_1^{\mathrm{MA}}$) for area VA (MA) minus the fitness of PCA. Therefore, positive values in the sJADE and tJADE graphs indicate parameters P for which the ICA method yielded a component more highly correlated to the associated HRF onset functions than the PCA method.

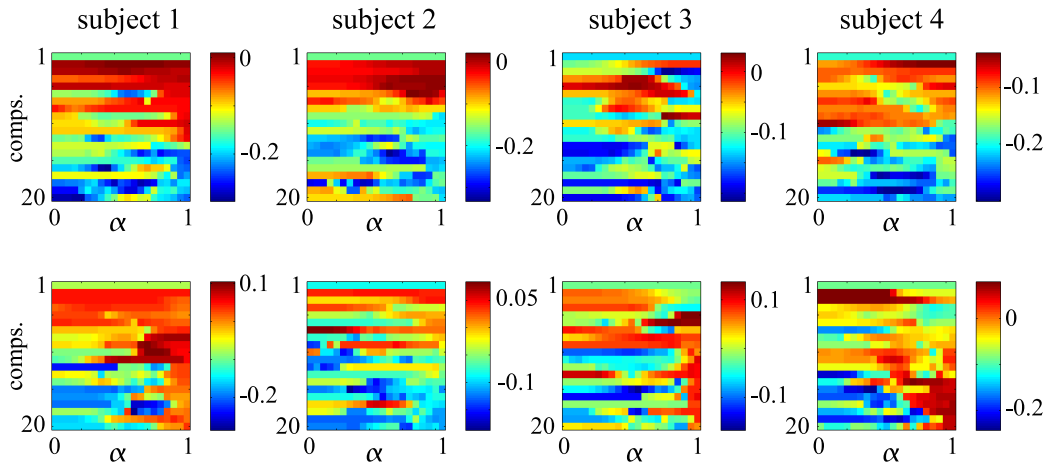

Figure 3.14: Fitness function F over parameter space Λ for stJADE. Plots show essentially the same for stJADE as Fig. 3.13 for sJADE and tJADE. For the now 2-dimensional parameter space Λ of stJADE, the fitness function F is presented for regions VA (upper half) and MA (lower half), color coded, according to colorbars. Again, PCA fitness (see Fig. 3.13) was used as a baseline and subtracted.

Using the decompositions obtained using the adjusted parameters from Tab. 3 the component of interest was selected for each ROI. For the two regions of interest VA and MA, I obtain one COI for each of the decomposition methods (PCA, sJADE, tJADE, and stJADE). Following chapter 3.1.3, for PCA I always select the first principal component, which was also the component achieving the highest correlation with the HRF onset function (see Tab. 3, number in brackets behind PCA fitness). For ICA methods, again following chapter 3.1.3 (only one COI per region), I selected that component of the decomposition realizing the maximum correlation. So, for example, in region VA of subject 3 decomposed with tJADE, correlation between patterns and $\tilde{u}_4$ is maximized when $P = 7$ patterns are extracted, and the highest correlation over these 7 patterns is 0.83 (compare Tab. 3). Now I chose this pattern out of the 7 extracted, which realizes the maximal correlation, to be the COI for VA obtained with tJADE.

This selection completes steps 5 and 6 of scheme 3.5 from chapter 3.1.2.

Until now, always all scans were used for correlation calculation and pattern selection. Following chapter 3.1.4 I select patterns in parallel only using the first (last) half of the measured scans. Tables 4 and 5 are equivalents of Tab. 3 for these two cases.

One sees a broad agreement between Tabs. 4 and 5 representing maximum fitness on the basis of the split data compared to Tab. 3 in which all information was used. COIs were selected separately for these three scenarios. The unused temporal data of the COIs selected using split data will be used for further connectivity analysis in the next chapter.

Finally, before beginning with connectivity analysis I will analyze how correlations found between patterns and associated HRF onset functions for VA and MA differ from correlations found for randomly positioned regions.

Besides the two ROIs, VA and MA, additionally 200 regions of the same size (8 mm radius spheres) were defined randomly located inside the brain. For statis-

tical analysis the first 100 regions will be used representing VA and the last 100 of the areas representing MA. These regions will be used to estimate the components selection connectivity baseline (compare section 3.1.4) later. For each of the first 100 areas, optimization of ICA parameters and COI selection was done in the same way as for VA, and for the last 100 regions in the same way as for MA. This yielded 100 COIs of random regions associated to $\tilde{u}_4$ and 100 COIs associated to $\tilde{u}_2$. For these COIs the mean correlation (= mean fitness) over the 100 COIs with $\tilde{u}_4$ and $\tilde{u}_2$ respectively is shown in Tab. 6.

Comparing mean maximum fitness values of the randomly positioned regions from Tab. 6 with maxima of defined ROIs VA and MA, one sees that the fitness function for ROIs achieves significantly higher values than the mean over the random areas. This reflects the relation between ROIs and onsets and confirms the GLM findings. But most importantly this indicates that ICA was able to identify the POIs and yielded paradigm-relevant COIs for VA and MA which can now be used for further connectivity analysis.

ROI	Decomp.	Subject 1	Subject 2	Subject 3	Subject 4
VA	PCA	0.82(1)	0.81(1)	0.84(1)	0.90(1)
	sJADE	0.83(12)	0.84(4)	0.87(9)	0.89(2)
	tJADE	0.82(2)	0.84(5)	0.86(7)	0.90(2)
	stJADE	0.82(2)	0.83(6)	0.87(9)	0.88(2)
MA	PCA	0.81(1)	0.79(1)	0.70(1)	0.84(1)
	sJADE	0.86(8)	0.84(3)	0.77(5)	0.90(17)
	tJADE	0.83(15)	0.80(2)	0.77(5)	0.89(3)
	stJADE	0.86(9)	0.85(7)	0.76(5)	0.90(3)

Table 4: Maximum of the fitness function using first half of the data only. As in Tab. 3 but now only taking the first half of all fMRI scans as basis.

ROI	Decomp.	Subject 1	Subject 2	Subject 3	Subject 4
VA	PCA	0.83(1)	0.79(1)	0.76(1)	0.89(1)
	sJADE	0.86(12)	0.82(4)	0.81(9)	0.87(10)
	tJADE	0.85(5)	0.84(6)	0.79(7)	0.89(4)
	stJADE	0.85(2)	0.86(6)	0.80(9)	0.88(10)
MA	PCA	0.62(1)	0.78(1)	0.51(1)	0.78(1)
	sJADE	0.77(8)	0.83(8)	0.70(5)	0.89(7)
	tJADE	0.74(9)	0.78(2)	0.71(11)	0.86(3)
	stJADE	0.79(10)	0.89(7)	0.73(6)	0.88(2)

Table 5: Maximum of the fitness function using second half of the data only. Compare Tables 4 and 3.

ROI	Decomp.	Subject 1	Subject 2	Subject 3	Subject 4
VA	PCA	0.27(0.06)	0.14(0.03)	0.18(0.14)	0.19(0.11)
	sJADE	0.31(0.09)	0.17(0.06)	0.21(0.17)	0.22(0.12)
	tJADE	0.32(0.08)	0.18(0.06)	0.22(0.17)	0.21(0.11)
	stJADE	0.33(0.08)	0.19(0.06)	0.23(0.19)	0.23(0.10)
MA	PCA	0.24(0.02)	0.17(0.05)	0.18(0.17)	0.22(0.20)
	sJADE	0.29(0.11)	0.21(0.09)	0.21(0.18)	0.24(0.21)
	tJADE	0.30(0.09)	0.21(0.08)	0.22(0.18)	0.24(0.19)
	stJADE	0.31(0.12)	0.22(0.10)	0.22(0.18)	0.26(0.23)

Table 6: Mean of maximum fitness function and extracted components for random regions. As in Tab. 3 the maximum of the fitness functions for the four decomposition algorithms, two regions, and four subjects were computed for the 100 randomly chosen regions. The table shows the mean over the ten maxima. Numbers in brackets denote the associated standard deviations.

3.2.4 Comparing connectivity of PCA and ICA components

Now connectivity between VA and MA was studied. As outlined in chapter 2.2.1, Pearson's correlation was computed between selected COIs from the two areas, during motion and static stimulation and compared to another. A higher correlation during motion than during static stimulation is hypothesized, indicating increased functional connectivity during motion. In addition five DCM models including the model in favor (compare section 3.2.1) were specified, estimated, and compared using SPM5.

As introduced in section 2.2.1 Form. 12, restricted empirical correlations between COIs during static condition u_3 were computed as

$$r_{X^{\mathrm{VA}}_{\pi(1)},X^{\mathrm{MA}}_{\pi(1)}}\Big|_{u_3} := \frac{\sum\limits_{t\in T_{u_3}} \left(X^{\mathrm{VA}}_{t\pi(1)} - \overline{X}^{\mathrm{VA}}_{\pi(1)}\Big|_{u_3}\right)\left(X^{\mathrm{MA}}_{t\pi(1)} - \overline{X}^{\mathrm{MA}}_{\pi(1)}\Big|_{u_3}\right)}{\sqrt{\sum\limits_{t\in T_{u_3}} \left(X^{\mathrm{VA}}_{t\pi(1)} - \overline{X}^{\mathrm{VA}}_{\pi(1)}\Big|_{u_3}\right)^2 \sum\limits_{t\in T_{u_3}} \left(X^{\mathrm{MA}}_{t\pi(1)} - \overline{X}^{\mathrm{MA}}_{\pi(1)}\Big|_{u_3}\right)^2}}. \quad (47)$$

Analog restricted empirical correlation was computed for the motion stimulus $r_{X^{\mathrm{VA}}_{\pi(1)},X^{\mathrm{MA}}_{\pi(1)}}\Big|_{u_2}$. Those two correlations were now determined for the four decomposition methods PCA, sJADE, tJADE, and stJADE on the basis of the whole data, then the first, and finally the second half of the scans. Thereby COIs selected on the whole, the second, and the first half of data were used. Tables 7 and 8 show the results of this analysis for each subject.

In addition, the 200 randomly positioned regions were used to estimate the CSCB for restricted correlation (compare page 52). From the first 100 models the COI associated to the HRF onset function of the visual stimulation $\tilde{u}_4$ was selected (analog for the last 100 and $\tilde{u}_4$). Analog to Form. 47, restricted correlations were computed 100 times, replacing the COIs used in Form. 47 with the COIs of the randomly located regions. The mean values for the CSCBs over these 100 computations is presented at the end of Tabs. 7 and 8. The CSCBs were only

computed on the basis of all scans.

In all cases, one sees a higher correlation during motion than during static stimulation ($\Delta > 0$) and, independent from the underlying data part, that connectivity changes between areas VA and MA lie high above the estimated CSCB estimates ($\Delta > \mathrm{CSCB}_{\Delta}$) which proofs the hypothesis. Figs. 3.15 and 3.16 summarize Tabs. 7 and 8 and show mean values and standard deviations for the different correlations.

One sees the higher correlation values between VA and MA during motion than during static, for all decomposition methods (left blue is below right blue bar in every graph) and that restricted correlations between VA and MA lie above the estimated CSCB (red bars). Accordingly I can conclude that the initial hypothesis for restricted correlation, $\Delta > \mathrm{CSCB}_{\Delta}$, was confirmed by PCA and all of the three ICA mehtods. This states that, so far, pattern connectivity can reproduce results obtained with the state of the art PCA method.

PCA				
ROI	S. 1	S. 2	S. 3	S. 4
$r(0,S)$	0.39	0.43	0.54	0.22
$r(0,S)$	0.77	0.85	0.77	0.80
Δ	0.38	0.42	0.23	0.58
$r(1,S)$	0.46	0.49	0.59	0.22
$r(1,M)$	0.85	0.86	0.83	0.83
Δ	0.39	0.37	0.23	0.61
$r(2,S)$	0.34	0.37	0.48	0.21
$r(2,M)$	0.69	0.83	0.71	0.77
Δ	0.35	0.46	0.23	0.56
CSCB_S	0.16	0.01	0.01	0.02
CSCB_M	0.20	0.04	0.03	0.05
CSCB_Δ	0.04	0.02	0.02	0.03

sJADE				
ROI	S. 1	S. 2	S. 3	S. 4
$r(0,\mathrm{S})$	0.38	0.34	0.31	0.38
$r(0,\mathrm{M})$	0.80	0.84	0.75	0.82
Δ	0.42	0.50	0.44	0.44
$r(1,\mathrm{S})$	0.54	0.16	0.37	0.07
$r(1,\mathrm{M})$	0.88	0.81	0.78	-0.10
Δ	0.33	0.65	0.41	-0.17
$r(2,\mathrm{S})$	0.22	0.28	0.28	0.26
$r(2,\mathrm{M})$	0.71	0.83	0.72	0.78
Δ	0.49	0.55	0.45	0.53
CSCB_S	0.17	0.01	0.00	0.03
CSCB_M	0.24	0.04	0.04	0.07
CSCB_Δ	0.07	0.04	0.04	0.04

Table 7: Correlation connectivity between VA and MA. The two tables show results of the connectivity analysis between VA and MA for decomposition algorithms PCA and sJADE. Correlation coefficients are denoted with $r(A,B)$ for A indicating the used datapart for component selection. For $A = 0$ the entire dataset was used for components selection and connectivity analysis, whereas for $A = 1$ ($A = 2$) the first (second) datapart was used for component selection and the second (first) part of the so selected COIs was used to compute restricted empirical correlations. Second parameter B indicates the experimental condition ($B = \mathrm{M}$ motion u_2; $B = \mathrm{S}$ static u_3), for which the correlation was computed (e.g. $r(0,\mathrm{M}) = r_{X^{\mathrm{VA}}_{\pi(1)},X^{\mathrm{MA}}_{\pi(1)}}\big|_{u_2}$ using all scans of $X^{\mathrm{VA}}_{\pi(1)}$ and $X^{\mathrm{MA}}_{\pi(1)}$). In addition, the difference Δ between correlations during motion and static conditions is presented. Finally, selected COIs from randomly positioned 200 regions were used to estimate the CSCB for the two restricted correlations (CSCB_S, CSCB_M) and their difference (CSCB_Δ) using all scans. Standard deviation of the CSCB estimates was always below 0.05.

tJADE				
ROI	S. 1	S. 2	S. 3	S. 4
r(0,S)	0.38	0.26	0.56	0.29
r(0,M)	0.77	0.78	0.84	0.85
Δ	0.39	0.52	0.28	0.56
r(1,S)	0.58	0.25	0.67	0.34
r(1,M)	0.87	0.76	0.87	0.89
Δ	0.29	0.52	0.21	0.55
r(2,S)	0.16	0.25	0.35	0.27
r(2,M)	0.63	0.78	0.75	0.82
Δ	0.47	0.54	0.40	0.55
$\mathrm{CSCB_S}$	0.16	0.02	0.02	0.03
$\mathrm{CSCB_M}$	0.23	0.06	0.04	0.06
CSCB_Δ	0.07	0.03	0.03	0.03

stJADE				
ROI	S. 1	S. 2	S. 3	S. 4
r(0,S)	0.40	0.22	0.13	0.29
r(0,M)	0.80	0.80	0.67	0.77
Δ	0.40	0.58	0.54	0.47
r(1,S)	0.57	0.07	0.07	0.31
r(1,M)	0.87	0.68	0.66	0.71
Δ	0.30	0.61	0.59	0.40
r(2,S)	0.23	0.25	0.14	0.22
r(2,M)	0.69	0.83	0.66	0.71
Δ	0.46	0.59	0.52	0.49
$\mathrm{CSCB_S}$	0.22	0.02	0.01	0.02
$\mathrm{CSCB_M}$	0.27	0.07	0.04	0.07
CSCB_Δ	0.05	0.05	0.03	0.05

Table 8: Correlation connectivity between VA and MA. The two tables show results of the connectivity analysis between VA and MA for decomposition algorithms tJADE and stJADE. For more details compare Tab. 7.

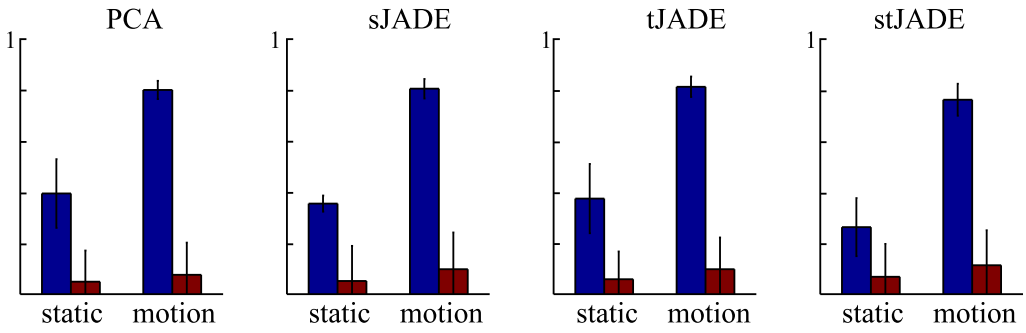

Figure 3.15: Restricted correlations between VA and MA on group level. Mean values (over subjects) for restricted empirical correlation onto static and motion conditions are presented (blue bars). The associated CSCB baseline is shown in red. Standard deviations over subjects are presented for the restricted empirical correlation and, for the CSCBs, additionally over the randomly positioned regions.

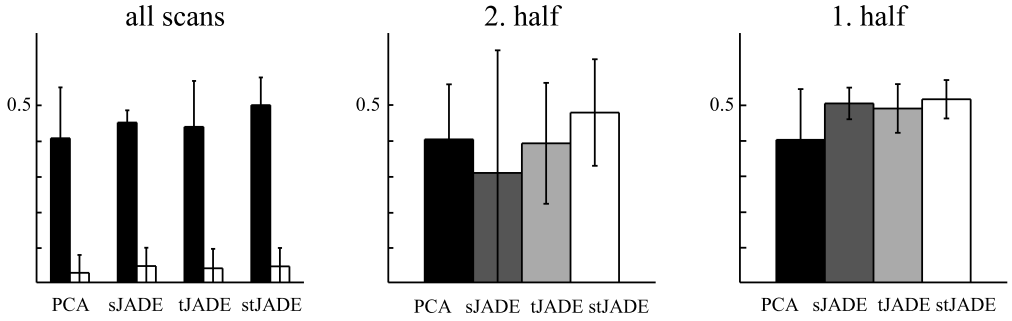

Figure 3.16: Functional connectivity changes between VA and MA on group level. Differences Δ between restricted empirical correlations during motion and static are shown for the three types of underlying data and the four decomposition types. In addition, in case all data was used, the component selection connectivity baselines CSCB_Δ for the differences are given (white bars in the left graph). Standard deviations over subjects are presented for all differences. For CSCB_Δ standard deviations were computed over subjects and random regions.

For DCM connectivity analysis, five models (see Fig. 3.17) were specified and estimated using the SPM5 toolbox. Each model consisted of one COI for each of the areas VA and MA, a bottom-up connection from the COI associated with VA to the COI associated to MA, and the stimulus condition (MS with onsets u_4) exciting VA. For model II, for example, one obtains the following DCM parameter matrices (compare section 2.2.2):

$$A = \begin{pmatrix} -1 & 0 \\ 1 & -1 \end{pmatrix}, \; B^1 = \begin{pmatrix} 0 & 0 \\ 0 & 0 \end{pmatrix}, \; B^2 = \begin{pmatrix} 0 & 0 \\ 1 & 0 \end{pmatrix}, \; C = \begin{pmatrix} 1 & 0 \\ 0 & 0 \end{pmatrix}. \quad (48)$$

Diagonal coefficients of matrix A represent stabilizing self-connections of the two areas and $a_{21} = 1$ the bottom-up connection from the VA COI to the MA COI. Modulation matrices B^1 and B^2 indicate effects of the two conditions visual and

motion respectively, onto the connections specified in A. Here, $b^2_{21} = 1$ represents the hypothesized motion modulation onto the bottom-up connection. Finally, parameters in C reflect external inputs into the system and $c_{11} = 1$ in particular represents the effect of the visual stimulus (motion and static combined) onto the VA COI.

Parameters of each model were estimated by fitting the model prediction to measured data (see section 2.2.2). I remind the reader that a-priori parameters equal to 1 (e.g. parameters in Form. 48) do not represent positive effects, but only one's beliefe that this connection or effect in itself exists. After the estimation of these a-priori models, positive values represent excitatory interactions whereas negative represent inhibitory. The favored model would be model II or IV, which are the simplest models including bottom-up motion modulation and thereby enabling an increase of the bottom-up connection during the motion stimulation.

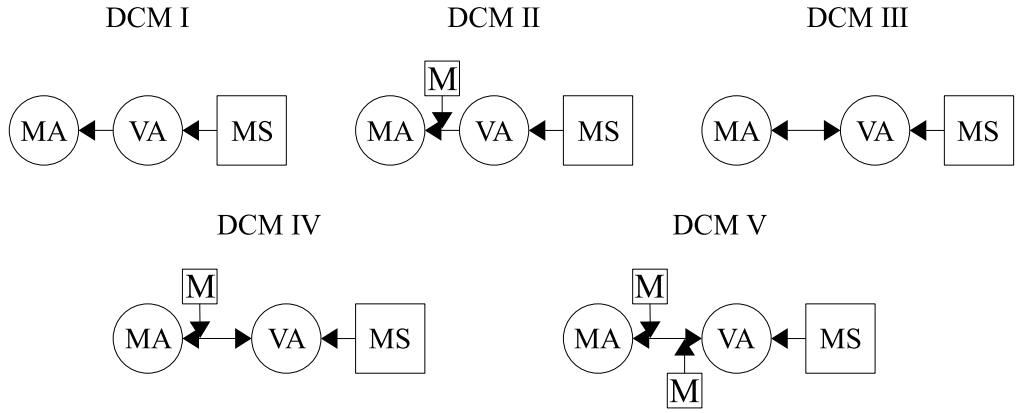

Figure 3.17: Five a-priori dynamic causal models. Regions are presented in circles and conditional inputs and modulators in squares. Condition MS indicates the stimulus condition u_4 (motion and static) whereas M denotes only motion u_2. Models are ordered from simplest I to the most complex V one.

For all subjects, estimations of DCM models were conducted on the basis of all scans and on the second or first half of scans depending on whether the first or second data part was used for COI selection. For these five models, Figs. 3.18 to 3.22 show estimated and averaged (over subjects) model parameters with associated maximum deviations.

Firstly, one sees that averaged estimated model parameters are comparable for the four decomposition methods and for the three types of underlying data (all scans, 2. half, 1. half). Most importantly, results obtained with ICA methods are comparable to those obtained with PCA. In addition, one sees that the bottom-up connection from VA to MA is strong, if no motion modulation onto it is allowed, and weak otherwise, indicating the importance of this bottom-up modulation, which was the hypothesis about the connectivity between VA and MA.

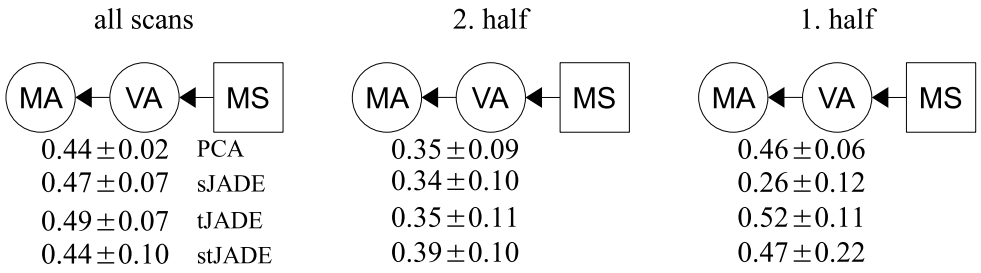

Figure 3.18: Averaged DCM model parameters (model I). The estimated and then averaged (over subjects) model parameters for model I are shown with associated maximum deviations. All parameters are in hertz. The four vertically arranged numbers represent the estimated bottom-up connection from VA to MA (a_{21}) for the four decomposition methods PCA, sJADE, tJADE, and stJADE (from top to bottom). Parameters were estimated on the basis of the entire data (left), second half (middle), and first half (right) of the data. Thereby underlying COIs were selected using the whole, first, and second datapart respectively.

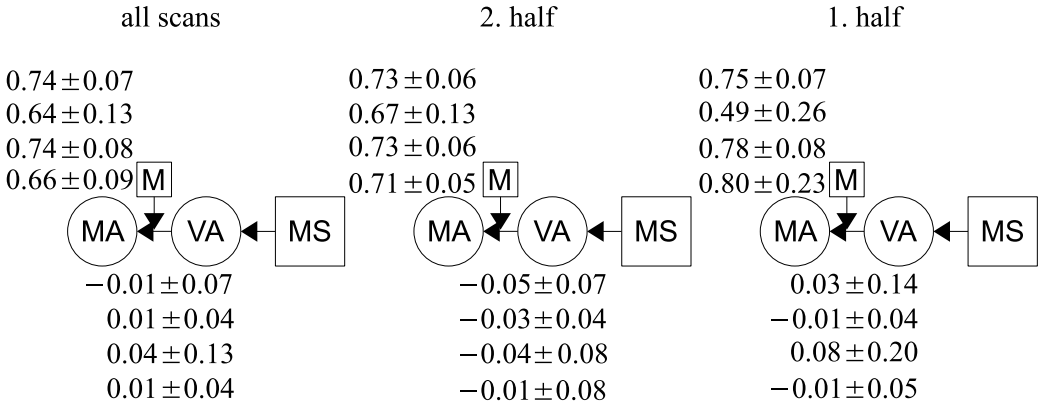

Figure 3.19: Averaged DCM model parameters (model II). As in 3.18 estimated and then averaged DCM model parameters are presented. The upper left values are associated with the motion (M) modulation onto the bottom-up connection from VA to MA (lower numbers).

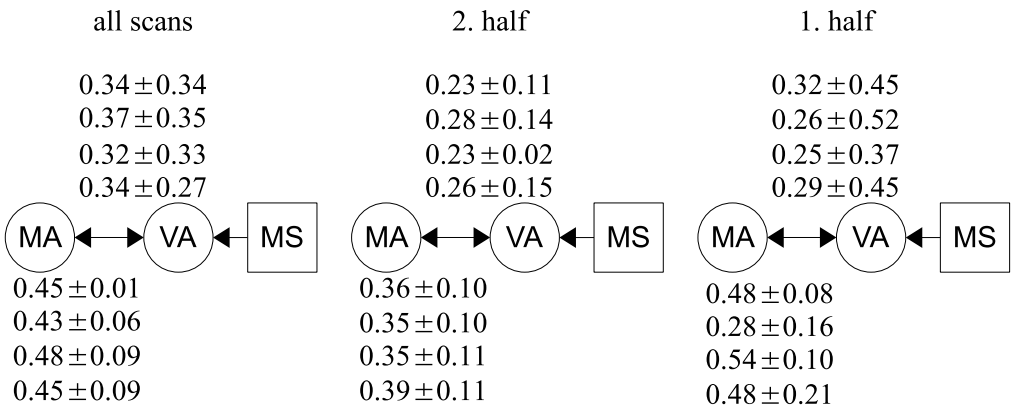

Figure 3.20: Averaged DCM model parameters (model III). As in 3.18 estimated and then averaged DCM model parameters are presented. The upper values are associated with the top-down connection from MA to VA.

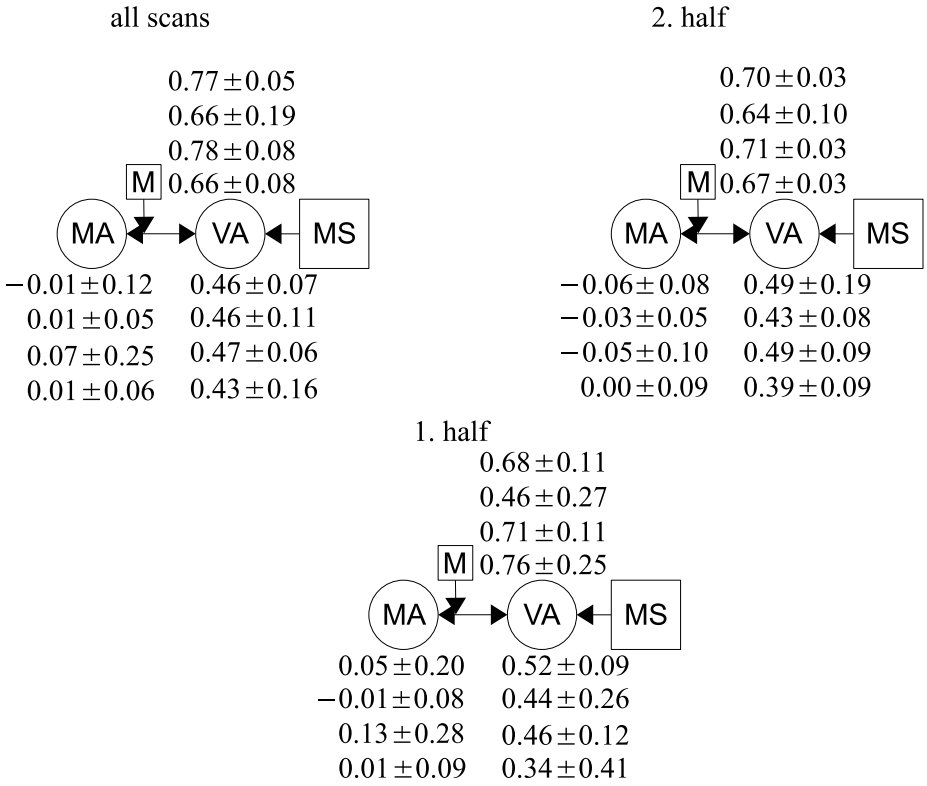

Figure 3.21: Averaged DCM model parameters (model IV). As in 3.18 estimated and then averaged DCM model parameters are presented. The upper right values are associated with the motion (M) modulation onto the bottom-up connection from VA to MA (lower left numbers) and the lower right values represent the estimated and averaged top-down effects from MA to VA.

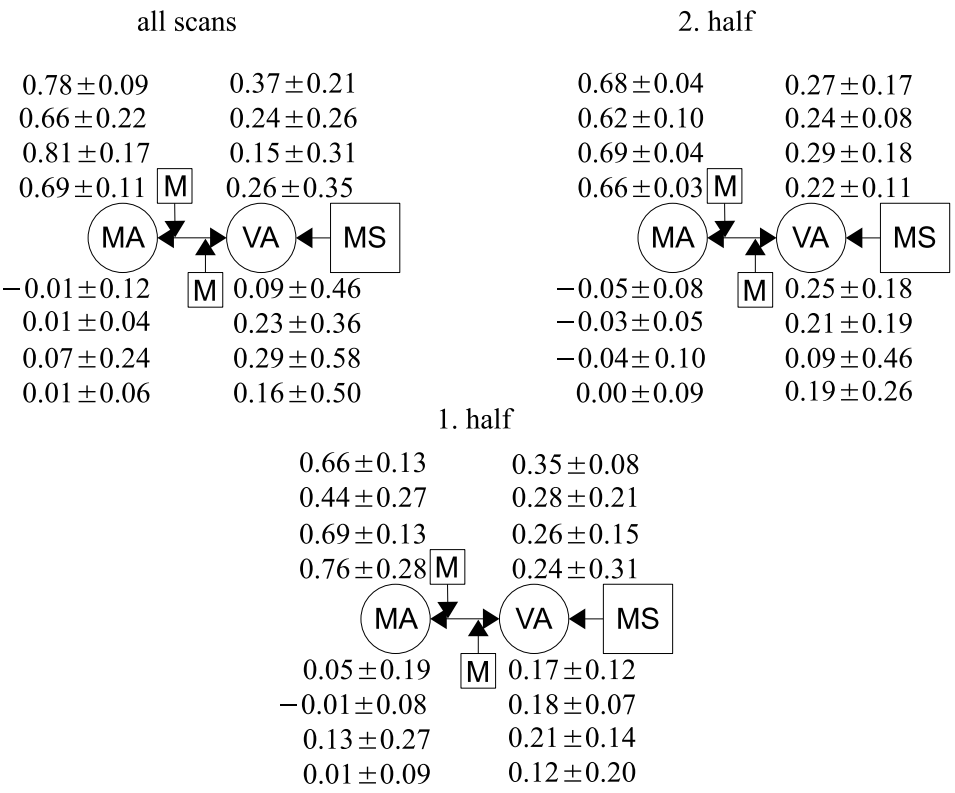

Figure 3.22: Averaged DCM model parameters (model V). As in 3.18 estimated and then averaged DCM model parameters are presented. The upper left and lower right values are associated to motion modulations onto bottom-up and top-down connections between VA and MA respectively.

After the estimation, all models were compared pairwise. Following section 2.2.2, the positive evidence ratios (PER) were computed for all model comparisons. Results are shown in Tab. 9.

Using the rank order selection introduced in section 2.2.2, one sees that for all decomposition methods and underlying data there is the same model hierarchy: IV, V, II, I, III (from best to worst). This will be described briefly for stJADE on the basis of the first datapart (lower right square of Tab. 9). Looking at model IV the PERs for models I, II, III, and V are: 4 : 0, 3 : 1, 4 : 0, and 4 : 0. Therefore all comparisons are in favor of model IV, which is not the case for any other model. Therefore model IV has rank 1 and is excluded from further considerations. Now looking at PERs of model V for comparison against models I, II, and III gives: 4 : 0, 3 : 1, and 4 : 0. So all PERs favor model III, which now is of rank 2 and excluded. PERs for model II compared to I and III are: 4 : 0 and 4 : 0 giving model II rank 3. Now only models I and III remain with a PER of 3 : 0 ranking model II at position 4 and model III at the last rank 5.

Although model II which was hypothesized in section 3.2.1 has not rank 1, the obtained rank order still implies the importance of the motion modulation, because models containing this modulation (models II, IV, and IV) are ranked better (lower) than models without it (model: III and V). The actual strength of the motion modulation can be estimated by comparing the estimated model parameters in Fig. 3.21 with their CSCBs.

The CSCB DCM model was only estimated for model IV. On the basis of all scans and the 200 randomly positioned regions, 100 dynamic causal models were estimated using the 100 COIs associated to $\tilde{u}_4$ and the 100 COIs associated to $\tilde{u}_2$ to replace the VA and MA COI respectively. The estimated mean parameters over the 100 DCMs are presented in Fig. 3.23. One sees that all mean parameters show deviations comparable to their sizes which points to an unstable estimation process of the DCM parameters, reflecting the random localization of the used regions which in most cases were not related to the paradigm. Most importantly one sees that the found motion modulations in Fig. 3.21 are higher than their CSCBs.

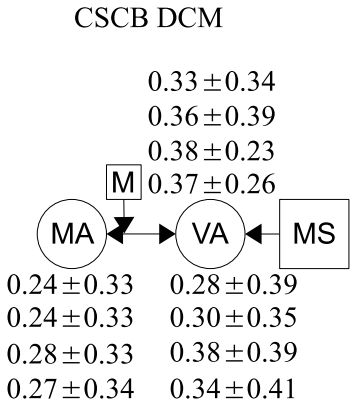

Figure 3.23: Mean CSCB DCM model parameters (model IV). As in 3.21 estimated and then averaged DCM model parameters are presented in the same way. The mean CSCB DCM parameters over the 100 dynamic causal models which were additionally averaged over subjects are shown.

One sees that ICA methods show the same result as PCA, and looking at model parameters, one sees that the motion modulation onto the bottom-up connection from VA to MA has large effects because the first three winner models contain it and the last two do not. This points to a higher effective connectivity from VA to MA during motion, which confirms the initial hypothesis about the underlying connectivity structure. It also supports the change found in functional connectivity by restricted empirical correlation between VA and MA during motion and static stimulation.

		all scans					2. half					1. half				
Decomp.	M	I	II	III	IV	V	I	II	III	IV	V	I	II	III	IV	V
PCA	I	**4.**	0	4	0	0	**4.**	0	4	0	0	**4.**	0	3	0	0
	II	4	**3.**	4	0	0	4	**3.**	4	0	0	4	**3.**	4	0	0
	III	0	0	**5.**	0	0	0	0	**5.**	0	0	0	0	**5.**	0	0
	IV	4	4	4	**1.**	2	4	4	4	**1.**	4	4	4	4	**1.**	4
	V	4	4	4	0	**2.**	4	4	4	0	**2.**	4	4	4	0	**2.**
sJADE	I	**4.**	0	***3***	0	0	**4.**	0	4	0	0	**4.**	1	3	1	1
	II	4	**3.**	4	0	0	4	**3.**	4	0	0	3	**3.**	3	1	1
	III	***0***	0	**5.**	0	0	0	0	**5.**	0	0	0	1	**5.**	1	1
	IV	4	4	4	**1.**	3	4	4	4	**1.**	4	3	3	3	**1.**	4
	V	4	4	4	0	**2.**	4	4	4	0	**2.**	3	3	3	0	**2.**
tJADE	I	**4.**	0	4	0	0	**4.**	0	4	0	0	**4.**	0	3	0	0
	II	4	**3.**	4	0	0	4	**3.**	4	0	0	4	**3.**	4	0	0
	III	0	0	**5.**	0	0	0	0	**5.**	0	0	0	0	**5.**	0	0
	IV	4	4	4	**1.**	3	4	4	4	**1.**	3	4	4	4	**1.**	4
	V	4	4	4	1	**2.**	4	4	4	0	**2.**	4	4	4	0	**2.**
stJADE	I	**4.**	0	3	0	0	**4.**	0	4	0	0	**4.**	0	3	0	0
	II	4	**3.**	4	0	0	4	**3.**	4	0	0	4	**3.**	4	1	1
	III	0	0	**5.**	0	0	0	0	**5.**	0	0	0	0	**5.**	0	0
	IV	4	4	4	**1.**	2	4	4	4	**1.**	3	4	3	4	**1.**	4
	V	4	4	4	1	**2.**	4	3	4	0	**2.**	4	3	4	0	**2.**

Table 9: Positive evidence ratios for DCM models. Each number gives the wins of the row model against the column model over the four subjects. Only models using the same dataparts and the same decomposition method were compared against each other. For example, the PER for the comparison between model I and model III for sJADE using all data would be $3:0$ (bold and italic numbers).

3.2.5 Summary

With the help of the BMS paradigm, I illustrated how the proposed method of pattern connectivity is applied to fMRI data and how arising problems such as finding optimal ICA parameters, and selecting components of interest can be treated with the methods proposed in sections 3.1.3 and 3.1.4.

For the results on basis of pattern connectivty one saw, that statistical effects due to component selection had no significant influence and that the three applied ICA approaches did not differ from each other.

Finally, I showed that connectivity analysis techniques (Pearson's correlation and DCM) applied to suitable selected ICA components generated the same connectivity measures as if applied to the first PCA component. Hence, I was able to reproduce findings obtained with the standard PCA method, using pattern connectivity which was the major goal of the BMS study.

3.3 II. Paradigm: Potentials of pattern connectivity

In the following an application for pattern connectivity is given, which lies outside the scope of the standard PCA method. The major goal of this study is to show that the proposed method of pattern connectivity enables the analysis of neuronal connectivity between multi-variate patterns of fMRI data in cases a region of interest contains more than one MVP. In particular, I want to show that ICA decomposition together with the introduced pattern selection algorithm (see section 3.1.3) are able to extract the evoked patterns and that the computation of connectivity measures on the basis of these pattern's temporal behaviors yields meaningful results.

Therefore, I conducted an fMRI study to investigate neuronal connectivity in a simple network consisting of two ROIs, the first containing two and the second containing one POI. The aim was to confirm intuitive hypotheses about the network using pattern connectivity to compute the connectivity measures restricted empirical correlation and DCM.

Additionally, I created synthetical fMRI data and will show that pattern connectivity can reproduce the underlying network used for data generation. As underlying network, the hypothesized connectivity structure for the real fMRI paradigm was used.

As for the BMS experiment, I follow the outlined scheme of Fig. 3.5.

3.3.1 Experimental setup and hypothesis

Similar to the BMS experiment, a model consisting of two ROIs was chosen. In the BMS paradigm, both regions of interest were represented by a single component of interest. Now a paradigm is presented, for which two COIs for one of the ROIs are needed, to capture its behavior.

As mentioned in chapter 2.3.1, the most popular brain area for multi-voxel pattern analysis is the visual cortex, evoking different activation patterns for different visual stimuli. Therefore I chose this area as the ROI with two COIs. Two differently orientated Gabor patches were used to evoke different spatial activation patterns. A Gabor patch is the pixelwise product of a sinusoidal and a gaussian stimulus. Fig 3.24 shows one of the two Gabor stimuli used and a small fixation cross in the middle of the screen. Due to its stimuli nature I refer to this experiment as the ORIENT experiment.

In addition to this stimulation, participants had to press a button dependent on the stimulus. Connectivity was studied between visual area VA which was already introduced in 3.2.1 and the motor area responsible for the button press, which is denoted as FM.

The paradigm was divided into 150 trials of about 9 s duration (compare Fig. 3.25). Each trial began with an initial fixation of 3, 4, 5 or 6 s followed by an instruction display of 0.5 s duration. After a short pause of 0.5 s in which only the small fixation cross was shown, a 45° or 135° Gabor patch (phase 0, frequency 1°, and Gauss constant 3°) was presented for 1.5 s in the middle of the screen. I want to refer to these two stimuli as S1 and S2.

Figure 3.24: Gabor patch. A superposition of a 2-dimensional Gauss function with a 2-dimensional sinusoidal function is called Gabor patch. For the presented Gabor patch, the 2-dimensional Gauss distribution has equal variances in both dimensions and the sinusoidal function is rotated with an angle of 45°.

Three instructions were possible: Two small black squares arranged in an angle of 45° instructed the participants to press a button with the right index finger as quickly as possible if and only if the 45° Gabor stimulus was shown. As before, to the second instruction of two black squares arranged in 135° (compare Fig. 3.25, second image from left) the participants had to press the same button also with the right index finger as fast as possible if and only if the 135° Gabor image appeared. The third instruction consisted of a small black circle and indicated the subjects just to fixate and not to press the button. These three instructions will be denoted as I1 (press if 45° Gabor patch), I2 (press if 135° Gabor patch), and I0 (fixation only). Each of the three instructions appeared in 50 trials, 25 times for each stimulus, resulting in 150 trials and about 675 functional scans. Instructions, durations of intertrial intervals (ITI), and stimuli were randomized over the experiment.

There are two reasons for using variable, random fixation durations (here 3, 4, 5, or 6 seconds) previous to each trial: At first, this shifts the stimuli onset relative to measurement time, so that over different trials the evoked HRF is sampled at different time points. Here, this increased the experimental sampling rate of 0.5 Hz to a virtual sampling rate of 1.0 Hz (see [104] for more details). Secondly and here more importantly, randomized onsets make it impossible for participants to anticipate stimulus onsets, which is of particular importance when subjects have to perform a task as fast as possible. Using randomized stimulus onsets is called jittering.

Another aspect in which BMS and ORIENT paradigm designs differ is the duration of stimulus presentation. Whereas in the BMS paradigm a block design was used, now a so-called event-related design is used, in which stimuli are presented only for a short time (here 1.5 s) causing weaker and unsaturated BOLD responses.

To avoid large movement artifacts, participants' exhaustion and other effects, which grow larger over time and cause temporal changes in the patterns, the overall length of the experiment had to be kept relatively short. However, as many trials per condition as possible had to be measured. The slow HRF after the stimulation

made relative large (here from $5 - 8$ s) intertrial intervals necessary, which also increased overall time.

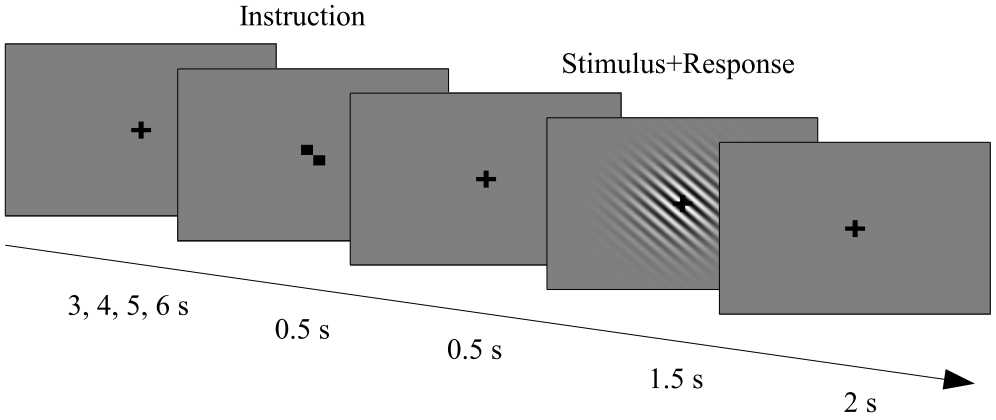

Figure 3.25: Design of an ORIENT trial. Each of the 150 trials of the ORIENT paradigm had the same design. After a randomized $3 - 6$ s lasting initial fixation period one out of three different instructions was shown for 0.5 s followed by a short 0.5 s lasting fixation. Then a Gabor patch with two possible orientations was presented for 1.5 s and dependent on the previous instruction participants had to press a button as fast as possible. Finally, a 2 s fixation period ended the trial. In the images, fixation crosses and the 135° instruction are presented oversized for better visualization.

Our hypothesis is that Gabor patches activate area VA and evoke two different activation patterns for the two orientations. Depending on previous instructions the interpretation of visual information in VA leads to an activation in a motor area, which causes the reaction to press the button. Between VA and the motor area information is processed by several other areas, which e.g. decide whether to respond or not (e.g. [123] [105] [164]). However for simplicity I will only study the visual area VA detecting the stimulus and the motor area FM executing the button press.

The part of the motor cortex known as the primary motor cortex (M1), located in the precentral gyrus integrates information from other cortical pre-motor and sensory areas (e.g. [131] [154]). Over direct connections to the spinal cord, M1 innervates contralateral muscles [131]. The primary motor cortex comprises a representation of different body parts (see Fig. 3.26 a) for a raw description) called a motor homunculus (e.g. [120] [133] [81]). In the scope of this work I are interested in the part representing the fingers only and will call this region FM shown in Fig. 3.26 b) in green.

Similarly to the BMS paradigm, I will introduce some notations: Voxel index sets of areas VA and FM will also be denoted as VA and FM. Together with the instructions I1, I2, and I0 the stimuli S1 and S2 give six possible conditions I0S1, I0S2, I1S1, I1S2, I2S1, and I2S2.

Figure 3.27 shows all subsequently used onsets. $u_1(t)$ denotes the motor onsets I1S1 and I2S2. This is the union of the two conditions, in which participants had to press the button. Analog $u_2(t)$ denotes the non-motor onsets of conditions I0S1, I2S1, I0S2, and I1S2. In addition, $u_3(t)$ and $u_4(t)$ denote the onsets of all

stimuli S1 and S2 respectively. For example, $u_3(t)$ contains onsets of all conditions with stimulus S1 (I0S1, I1S1, and I2S1). Here the stimulus onset and not the instruction onset time is used. Onset's duration was set to 1.5 s. In addition a baseline regressor $u_0 = u_B$ modeling the default activity of the brain was specified. The onsets of this regressor start with the offset of the Gabor patch stimulus and also last for 1.5 s. Finally, I need onsets of I1S1, I2S2, I1S2, and I2S1, which will be denoted u_5, u_6, u_7, and u_8 respectively (compare Fig. 3.27).

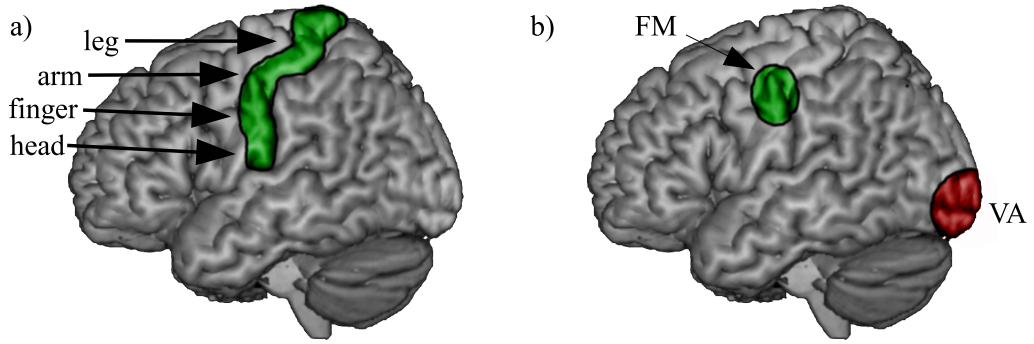

Figure 3.26: Regions of interest for the ORIENT paradigm. a) Motor homunculus b) Regions of interest, VA and FM, for the ORIENT paradigm.

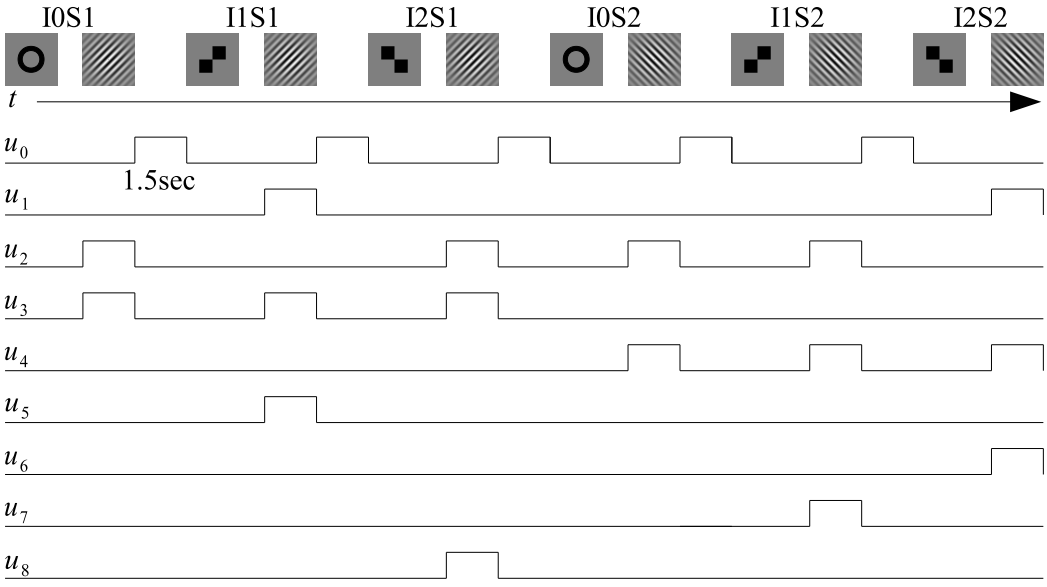

Figure 3.27: Conditions of ORIENT paradigm. The figure shows a hypothetical series of six trials including the six possible task and stimulus combinations I0S1, I1S1, I2S1, I0S2, I1S2, and I2S2 (first row). Below onset functions u_0, ..., u_8 are presented. For example, one sees that onset function u_2 represent trials for which the participant was instructed just to fixate. All onsets except u_0, which is the baseline onset and starts after the Gabor patch stimulus of each trail, begin with the Gabor patch stimulation. Each onset has a duration of 1.5 s.

The two COIs in VA are associated with onsets u_3 (S1, 45° stimulus) and u_4 (S2, 135° stimulus). Their associated HRF onset functions are

$$\tilde{u}_1^{VA} = \tilde{u}_3, \quad \tilde{u}_2^{VA} = \tilde{u}_4. \tag{49}$$

For the motor COI in FM the associated HRF onset function is

$$\tilde{u}_1^{FM} = \tilde{u}_1. \tag{50}$$

These HRF onset functions are used later to find optimal ICA parameters and to select COIs.

One now expects the connectivity between the two COIs of VA and the COI of FM to change, depending on the given instruction and perceived stimulus. Considering, for example, the bottom-up connection from the 45° COI in VA to FM, I expect to find an increase of this connection during trials in which the previous instruction agreed with the stimulus (here 45° instruction I1), relative to those trials in which the instruction did not agree with the stimulus (here 135° instruction I2).

For restricted empirical correlation, I now had two hypotheses, one for the COI $X^{\mathrm{VA}}_{\pi(1)}$ associated with $\tilde{u}_1^{VA}$ and one for the second COI $X^{\mathrm{VA}}_{\pi(2)}$ associated with $\tilde{u}_2^{VA}$. For $X^{\mathrm{VA}}_{\pi(1)}$, for example, I hypothesized a higher correlation with the FM COI during I1S1 trials than during I2S1 trials. Analog I hypothesized a higher correlation between $X^{\mathrm{VA}}_{\pi(1)}$ and the FM COI during I2S2 trials than during I1S2 trials:

$$r_{X^{\mathrm{VA}}_{\pi(1)}, X^{\mathrm{FM}}_{\pi(1)}}\Big|_{u_5} > r_{X^{\mathrm{VA}}_{\pi(1)}, X^{\mathrm{FM}}_{\pi(1)}}\Big|_{u_8} \tag{51}$$

$$r_{X^{\mathrm{VA}}_{\pi(2)}, X^{\mathrm{FM}}_{\pi(1)}}\Big|_{u_6} > r_{X^{\mathrm{VA}}_{\pi(2)}, X^{\mathrm{FM}}_{\pi(1)}}\Big|_{u_7} \tag{52}$$

For illustrative purpose, the COIs $X^{\mathrm{VA}}_{\pi(1)}$ and $X^{\mathrm{VA}}_{\pi(2)}$ of VA are denoted as VA1 and VA2 respectively, and also the COI $X^{\mathrm{FM}}_{\pi(1)}$ is denoted as FM.

Besides functional connectivity using restricted empirical correlation also effective connectivity applying DCM was analyzed. The hypothesized DCM model reflects the restricted correlation hypotheses, and is presented in Fig. 3.28. I expected bidirectional connections between VA COIs and FM, which are modulated on the bottom-up part through instructions . For example, I hypothesized a positive modulation of condition I1S1 onto the connection between VA1 and the motor COI.

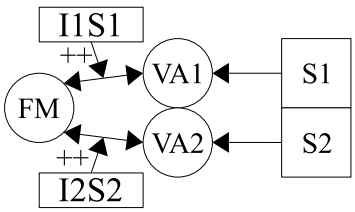

Figure 3.28: Expected DCM model for ORIENT paradigm. Gabor patch stimuli S1 and S2 excite patterns in VA. I hypothesize bottom-up connections from VA1 and VA2 to COI FM, which are modulated by motor conditions I1S1 and I2S2 respectively and increase during these conditions.

To test this hypothesis, four additional DCM-models representing different connectivity structures were estimated. All models were compared pairwise and the hierarchy between models was determined as introduced in section 2.2.2. The stated hypothesis is verified, if models which show a strong and positive instruction modulation from the VA COIs to the FM COI achieve better rankings (lower rank) in the model hierarchy than models that lack these modulations or show only weak or negative modulation strengths.

FMRI acquisition protocol and performed preprocessing steps were exactly the same as for the BMS experiment and were introduced in section 2.1.3. Three righthanded subjects (2 male, 1 female, aged $21 - 24$ years) participated in the experiment. All were familiarized with experimental tasks before fMRI scan session. All participants had normal or corrected-to-normal vision, and none had a history of neurological or psychiatric illness.

3.3.2 Behavioral data

A necessary constraint to find a motor component or even to locate area FM is that participants were able to do the task, which means that they pressed the button only when the instructed Gabor patch was presented. Hence the task was intended to be solved easy for participants. To check this, behavioral data was analyzed by computing hit rates h and false-alarm rates f for the three possible instructions. The hit rate gives the percentage of actual button presses relative to the number of trials in which the button had to be pressed. The false-alarm rate gives the ratio of trials in which the button was pressed even though the participant was instructed otherwise. Results are shown in Tab. 10.

One sees hit rates of almost 100 % ($h = 1$) and a false-alarm rate of 0 % for all conditions and subjects. This means that participants performed very well. Scans of trials in which subjects did not correctly respond were excluded from further analysis.

subject	h (45°)	h (135°)	f (45°)	f (135°)	false-alarm rate (G)
1	1.00	1.00	0.00	0.00	0.02
2	1.00	0.92	0.00	0.00	0.06
3	1.00	1.00	0.00	0.00	0.00

Table 10: Behavioral results for ORIENT paradigm. Hit rates h and false alarm rates f are shown. For instruction G, where participants had only to fixate, only a false-alarm rate exists.

3.3.3 Synthetic data

Besides the ORIENT study, I give an additional validation for pattern connectivity applied to regions with more than one pattern. Therefore a synthetic fMRI data set was generated for which patterns, connections, and connectivity changes are exactly known and can be compared to the results found with pattern connectivity.

For a better comparability, data dimension of $64 \times 64 \times 34$ voxels and 675 scans was kept the same. A voxelwise baseline activation Z_0 was defined as a

uniformly distributed (between $[-1; 1]$) random vector of dimension $64 \times 64 \times 34$. In addition three spatial activation patterns Z_1, Z_2, and Z_3 were generated as uniformly distributed random vectors of dimension $64 \times 64 \times 34$ and coefficients in $[0; 1]$. The first two patterns Z_1 and Z_2 were located at voxel position $(20; 42; 15)$ by voxelwise multiplication with a 3D-gaussian kernel ($\sigma^2 = 20$ voxels). Analogously pattern Z_3 was localized at $(42; 20; 15)$. Patterns Z_1 and Z_2 can be seen as patterns of interest of the 45° and the 135° stimulus respectively whereas Z_3 will represent the motor activation pattern.

The synthetic data set will be treated as a fourth participant during the ORIENT experiment. Steps of ROI definition and component selection were carried out in the same as for human subjects.

As a basis for the temporal behavior of the patterns, I took the paradigm onsets from subject 3. To simulate a real underlying network of connected patterns DCM was used to integrate (compare Form. 14 in section 2.2.2) these onsets, using the hypothesized model of Fig. 3.28. Denoting the neuronal activity of the three patterns as z_1, z_2, $z_3 : \mathbb{R}^+ \to \mathbb{R}$ and defining used DCM onsets $U_1 = u_3$ (S1), $U_2 = u_4$ (S2), $U_3 = u_5$ (I1S1), and $U_4 = u_6$ (I2S2), One obtains the following parameters for the a-priori model of Fig. 3.28:

$$A = \begin{pmatrix} -1 & 0 & 1 \\ 0 & -1 & 1 \\ 1 & 1 & -1 \end{pmatrix}, \; B^1 = \begin{pmatrix} 0 & 0 & 0 \\ 0 & 0 & 0 \\ 0 & 0 & 0 \end{pmatrix}, \; B^2 = \begin{pmatrix} 0 & 0 & 0 \\ 0 & 0 & 0 \\ 0 & 0 & 0 \end{pmatrix} \tag{53}$$

$$B^3 = \begin{pmatrix} 0 & 0 & 0 \\ 0 & 0 & 0 \\ 1 & 0 & 0 \end{pmatrix}, \; B^4 = \begin{pmatrix} 0 & 0 & 0 \\ 0 & 0 & 0 \\ 0 & 1 & 0 \end{pmatrix}, \; C = \begin{pmatrix} 1 & 0 & 0 & 0 \\ 0 & 1 & 0 & 0 \\ 0 & 0 & 0 & 0 \end{pmatrix} \tag{54}$$

Here now $a_{31} = a_{32} = a_{13} = a_{23} = 1$ represent the bottom-up and top-down connections between the two visual patterns and the motor pattern. The four B matrices give the modulations of the four onsets U_1, ..., U_4 onto the direct connections. In particular, $b^3_{31} = b^4_{32} = 1$ indicate the modulation of U_3 and U_4 onto the corresponding bottom-up connection. Finally, $c_{11} = c_{22} = 1$ states that the first visual pattern gets its input from U_1, which is the 45° Gabor patch condition, and that the second visual pattern is excited by U_2, which is the 135° Gabor patch stimulus. The neuronal behavior of the system is now described by the following equation (compare Eq. 14):

$$\dot{z}(t) = \left(A + \sum_{i=1}^{4} U_i(t) B^i \right) z(t) + CU(t) \tag{55}$$

Using the Balloon model implemented in SPM5, this yielded simulated BOLD responses $\chi_i = \lambda(z_i)$ for the three patterns $i = 1, 2, 3$. An illustration of this process is shown in Fig. 3.29.

Having the spatial (Z_1, Z_2, Z_3) and temporal parts (χ_1, χ_2, χ_3) for the three patterns and assuming a linear model as in Eq. 30, simulated BOLD activation at time t can now be generated as:

$$Y_t = Z_0 + \sum_{p=1}^{3} Z_p(\chi_p(t) + \varepsilon(t)) + Z_{\mathrm{rnd}}(t). \tag{56}$$

Here ε and $Z_{\mathrm{rnd}}(t)$ are standard, normally distributed temporal and spatial noise terms ($\sigma^2 = 0.04$). The final generation of the artificial data is illustrated in Fig. 3.30.

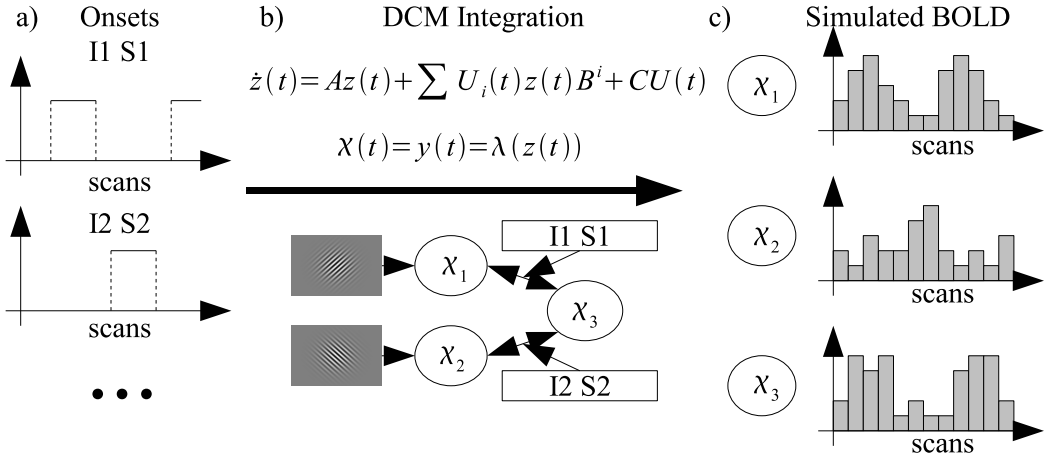

Figure 3.29: Simulating COI's BOLD response by integration of onsets using DCM. Onsets (a) are integrated using the hypothesized DCM a-priori model and the bilinear DCM approximation for the neuronal level (b) of Eq. 14, to obtain simulated neuronal pattern time courses, with which I can compute a BOLD response using the Balloon model (c).

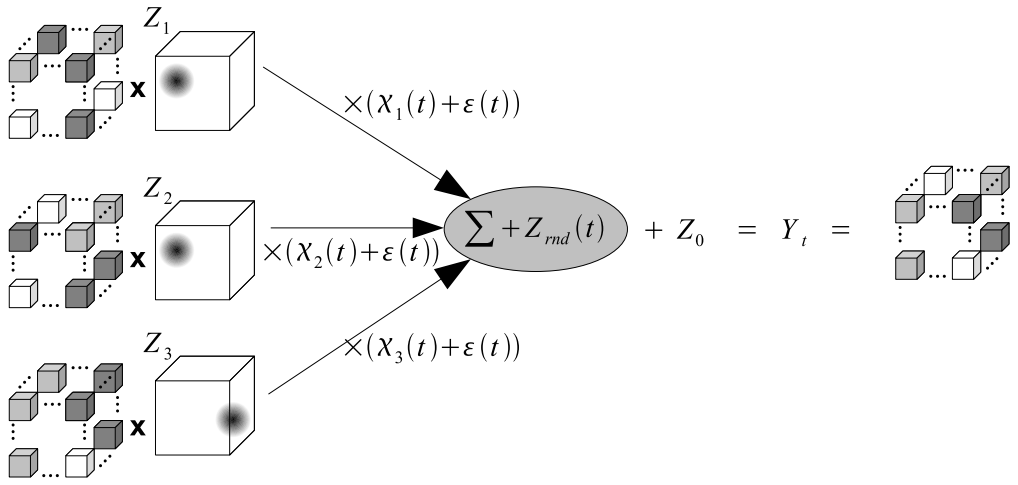

Figure 3.30: Simulated data as superposition of patterns of interest. Localized random spatial activation patterns Z_i ($i = 1, 2, 3$) are weighted with corresponding time courses χ_i ($i = 1, 2, 3$) and added to form the over datamatrix Y of the synthetic data.

To validate pattern connectivity, it was not necessary to include artifacts such as head motion. Therefore several of the preprocessing steps described in 2.1.3

were not applied onto the synthetic data set. Only the temporal mean removal for each voxel and the bandpass filter were applied.

3.3.4 Region of interest definition

To determine individual positions of the regions VA and FM I again used two GLM contrasts. Baseline regressor u_0 together with motor and non-motor conditions u_1 and u_2 were used for the GLM design matrix.

To locate visual area VA I searched for voxels activated during the presentation of the Gabor patch. In this way, I compared stimulus regressors against baseline using the contrast $c_{\mathrm{VA}} = (-1,\ 0.5,\ 0.5)$. For the motor area I compared motor versus non-motor regressor using $c_{\mathrm{FM}} = (0, 1, -1)$. For subject 3, Figs. 3.31 and 3.32 present the t-maps for c_{VA} and c_{FM} respectively. GLM t-value images for participants 1 and 2 can be found in appendix section 5.1 Fig. 5.4, 5.5, and 5.6. In the images, t-values were plotted color coded for voxels exceeding an threshold of $p < 0.001$ ($T > 3.1$).

A GLM for the synthetic data set was also computed, using the same contrasts and thresholds to localize areas VA and FM. Figure 3.33 presents results of this analysis. As ROI's positions were arbitrary for the synthetic data set and no structural MR scan was defined, only non-normalized images are shown.

In agreement with other studies examining finger movements (e.g. M1 coordinates $(-46;\ -14;\ 50)$ in MNI space for discrete finger movements [56], see also [133]) I find area FM in the left hemisphere at the positions shown in Table 11. For area VA, I find approximately the same coordinates as in the BMS study. Finally estimated ROI positions for synthetic data differ only by about a few voxels from the positions used to generate the data (VA at $(20;\ 42;\ 15)$ and FM at $(42;\ 20;\ 15)$).

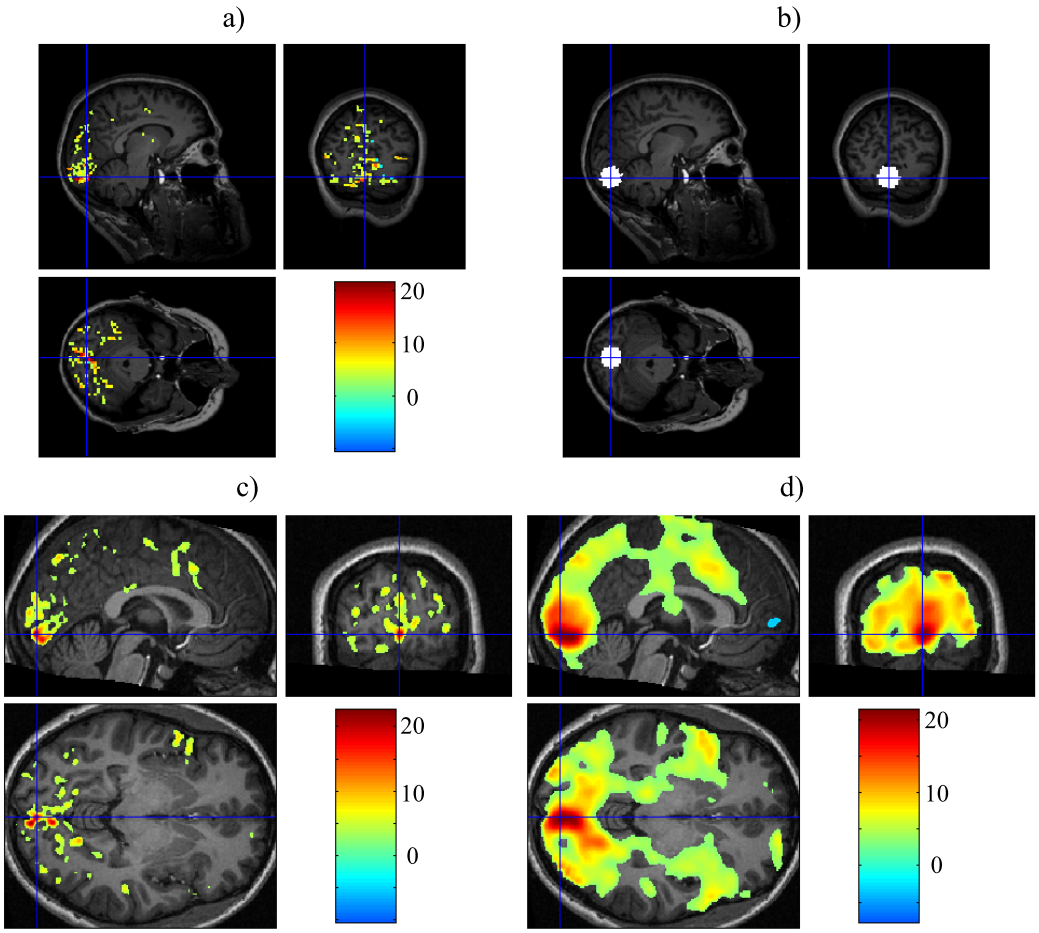

Figure 3.31: SPM of GLM contrast c_{VA} for subject 3 for ORIENT paradigm. In all four images data presented is shown as an overlay over the structural scan (not normalized for a) and b), normalized for c) and d)). In a), c), and d) voxels with $p < 0.001$ ($T > 3.1$) with respect to GLM contrast c_{VA} are shown color coded, according to their t-values. Voxels with negative t-values (below -3.1) are also presented. Those are negatively correlated voxels. the Activation clusters with fewer than 5 voxels were excluded from the images. In a) the raw data after the slicetiming and realignment preprocessing steps was taken as a basis, whereas in c) the data was also normalized to MNI space. d) shows the result for the GLM of normalized and smoothed (gaussian kernel of 8 mm) data. In b), voxels of the depicted slice belonging to the ROI VA are colored white. The crosshair in all images is located at the same position which for the t-maps is the location of the peak voxel.

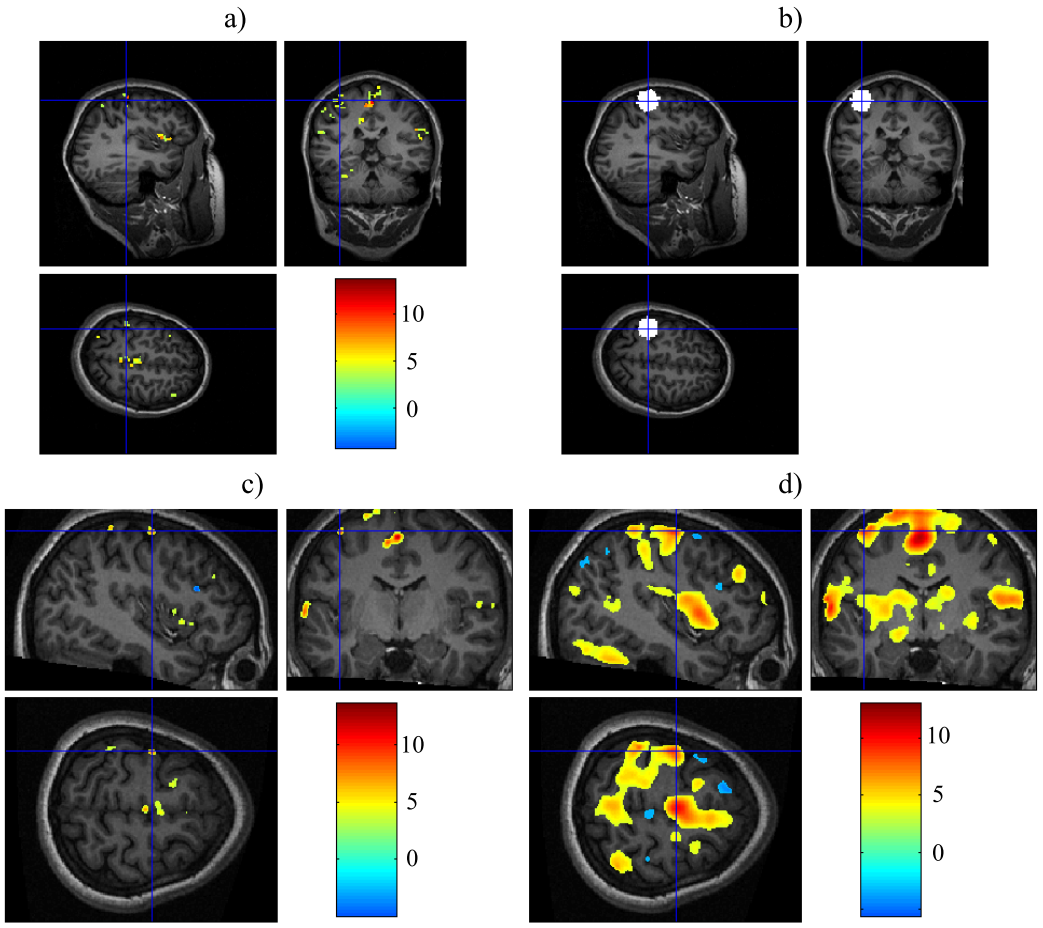

Figure 3.32: SPM of GLM contrast c_{FM} for subject 3 for ORIENT paradigm. Here the same images as in Figure 3.31 are presented for area FM using GLM contrast c_{FM}.

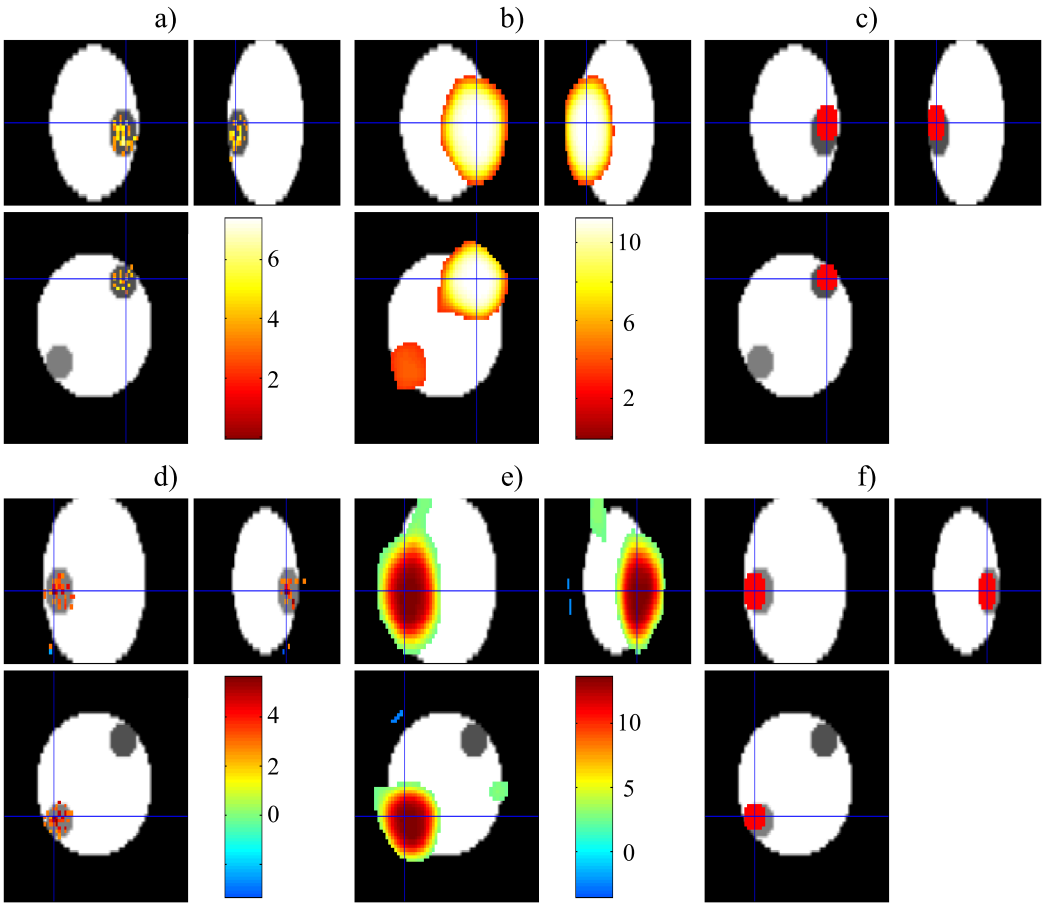

Figure 3.33: SPM of t-values for the GLM contrasts c_{VA} and c_{FM} on the basis of synthetic data. As in Figs. 3.31 and 3.32 maps of t-values are shown now for synthetic data. Images in the upper half, (a)-(c), show contrast c_{VA} and images in the lower half, (d)-(f), show contrast c_{FM}. In (a) and (d) one sees the unsmoothed, color coded t-values for region VA (a) and FM (d) using contrasts c_{VA} and c_{FM} respectively. The coordinate cross is placed at the voxel with highest t-value. Next in (b) and (e), one sees smoothed GLM results for the two contrasts. Finally, in (c) and (f) one sees voxels of the specified ROIs in red, which are used for further analysis. Due to the lack of a structural scan, the background image is a shematical illustration. The two gray spheres of the background are located at the original positions of regions VA and MA which were used to generate the data.

ROI	voxels	t-value (raw)	MNI coordinates		
VA (S1)	251	9.24	14	−89	13
VA (S2)	251	13.01	9	−90	1
VA (S3)	255	20.89	4	−84	−7
VA (S4)	251	7.37	19	45	17
FM (S1)	251	6.04	−33	−10	62
FM (S2)	251	6.91	−44	−30	45
FM (S3)	255	8.72	−41	−14	58
FM (S4)	251	5.60	41	18	15

Table 11: ROI information for the ORIENT paradigm. The table presents the number of voxels, t-value of central ROI voxel, and MNI coordinates of areas VA and FM for all three human subjects S1, S2, and S3 and the synthetic data (S4). Coordinates for synthetic data were not normalized.

As in the BMS paradigm all voxels inside a sphere of 8 mm around the peak voxel were included into the voxel index sets VA and FM resulting in an almost identical number of voxels for each ROI (see also Figures 3.31 b), 3.32 b), and 3.33 c) and f) for an illustration).

3.3.5 ICA parameters and component selection

Extracted data matrices Y^{VA} and Y^{FM} were decomposed using the three decomposition methods sJADE, tJADE, and stJADE. ICA components were computed with parameters $a = P \in \{2, ..., 20\}$ for sJADE and tJADE and $a = (P,\alpha) \in \{2, ..., 20\} \times \{0.00, 0.05, ..., 1.00\}$ for stJADE:

$$Y^{\mathrm{VA}} = X^{\mathrm{VA}}(a)C^{\mathrm{VA}}(a), \quad Y^{\mathrm{FM}} = X^{\mathrm{FM}}(a)C^{\mathrm{FM}}(a). \tag{57}$$

Following section 3.1.3, fitness function F was computed for each parameter. Because FM consists only of the motor COI, the fitness function given in Eq. 36 can be used:

$$F_{\mathrm{FM}}(a) = \max_{p=1,\ ...,\ P} |r_{X_p^{\mathrm{FM}}(a),\tilde{u}_1^{\mathrm{FM}}}|, \tag{58}$$

where $\tilde{u}_1^{\mathrm{FM}} = \tilde{u}_1$ was the HRF onset function of the motion condition u_1. Because region VA consists of two COIs, the fitness function for VA has to employ both associated onset functions, $\tilde{u}_1^{\mathrm{VA}}$ and $\tilde{u}_2^{\mathrm{VA}}$, for the two components. Using Eq. 35 I get

$$F_{\mathrm{VA}}(a) = \sqrt{\max_{p=1,\ ...,\ P} |r_{X_p^{\mathrm{VM}}(a),\tilde{u}_1^{\mathrm{VA}}}| \max_{p=1,\ ...,\ P} |r_{X_p^{\mathrm{VA}}(a),\tilde{u}_2^{\mathrm{VA}}}|}. \tag{59}$$

So only parameter sets a, giving decompositions containing a component that is highly correlated with $\tilde{u}_1^{\mathrm{VA}}$, which is the HRF onset function of S1 stimulus u_3 ($= 45°$), and a component that is highly correlated with $\tilde{u}_2^{\mathrm{VA}}$, which is the HRF onset function of S2 stimulus u_4 ($= 135°$) will have a high fitness.

Decompositions of parameters which maximize fitness functions, can be used for COI selection (see chapter 3.1.3). In addition, the fitness function was also

computed using only the first or second half of the data, for later connectivity analysis on the basis of the unused data part. Optimal parameters a (in brackets) and their maximal fitness values are shown in Tab. 12.

As for the BMS paradigm (compare section 3.2.3 page 52), besides the two ROIs VA and FM, additionally 200 regions of the same size (8 mm radius spheres) were defined randomly located inside the brain. Again, for each of the first 100 areas, optimization of ICA parameters and COI selection was done in the same way as it was done for VA (FM analog for the last 100 regions). The mean fitness value for both sets of regions is also presented in Tab. 12.

ROI	Decomp.	Subject 1	Subject 2	Subject 3	Subject 4
VA(0)	sJADE	0.22(18)	0.31(20)	0.25(19)	0.72(5)
	tJADE	0.25(16)	0.25(14)	0.26(18)	0.62(13)
	stJADE	0.24(11; 0.65)	0.23(15; 0.65)	0.29(11; 0.50)	0.70(2; 1.00)
VA(1)	sJADE	0.24(20)	0.27(20)	0.26(19)	0.73(5)
	tJADE	0.28(10)	0.28(4)	0.28(12)	0.63(11)
	stJADE	0.25(7; 0.30)	0.30(20; 1.00)	0.27(19; 0.80)	0.71(2; 1.00)
VA(2)	sJADE	0.28(15)	0.32(19)	0.25(16)	0.72(7)
	tJADE	0.27(20)	0.30(10)	0.27(13)	0.62(13)
	stJADE	0.26(13; 0.15)	0.26(12; 0.65)	0.28(20; 0.35)	0.69(2; 1.00)
RND	sJADE	0.19(0.04)	0.19(0.02)	0.20(0.03)	0.19(0.02)
	tJADE	0.19(0.03)	0.20(0.03)	0.20(0.02)	0.19(0.01)
	stJADE	0.20(0.03)	0.20(0.03)	0.21(0.02)	0.20(0.02)
FM(0)	sJADE	0.38(17)	0.37(3)	0.39(6)	0.54(4)
	tJADE	0.27(12)	0.39(9)	0.37(3)	0.63(9)
	stJADE	0.38(17; 0.95)	0.37(3; 1.00)	0.42(12; 0.35)	0.53(6; 0.65)
FM(1)	sJADE	0.41(17)	0.40(19)	0.43(6)	0.54(2)
	tJADE	0.28(17)	0.37(9)	0.44(3)	0.66(4)
	stJADE	0.42(18; 0.85)	0.40(20; 0.65)	0.45(11; 0.50)	0.54(6; 0.55)
FM(2)	sJADE	0.39(17)	0.39(4)	0.36(19)	0.55(4)
	tJADE	0.32(11)	0.44(10)	0.39(10)	0.62(9)
	stJADE	0.38(17; 0.95)	0.40(2; 0.30)	0.41(12; 0.00)	0.54(4; 0.75)
RND	sJADE	0.24(0.06)	0.21(0.03)	0.26(0.06)	0.23(0.05)
	tJADE	0.23(0.06)	0.23(0.04)	0.25(0.05)	0.23(0.05)
	stJADE	0.25(0.06)	0.23(0.04)	0.29(0.07)	0.25(0.05)

Table 12: Maximum and fitness of ICA decompositions for regions VA and FM. Maximal fitness values, $F_{\mathrm{VA}}(a_{\mathrm{VA,opt}})$ and $F_{\mathrm{FM}}(a_{\mathrm{FM,opt}})$, for VA and MA respectively on the basis of all scans (ROI(0)), first (ROI(1)), and second (ROI(2)) data part with associated parameters, $a_{\mathrm{VA,opt}}$ and $a_{\mathrm{FM,opt}}$ (in brackets), are presented for the three subjects and the synthetic data (subject 4). Rows denoting *RND* show the mean maximum fitness of the 100 randomly positioned areas with standard deviations (in brackets).

Comparing maximum fitness of regions VA and FM with the expected maximum fitness estimated from the randomly localized areas, one sees that VA and FM showed higher fitness than randomly positioned regions. This indicates that ICA was able to identify paradigm-relevant components in VA and FM. One sees a

great difference between ROIs and random regions maximum fitness, for synthetic data, and a smaller differences for human data. This indicates that for the human data, ICA was unable to identify spatial pattern and their time courses as accurate as for the synthetic data.

As a test, I also computed the PCA decomposition of Y^{VA}, which as expected (see chapter 3.1) yielded only inconsistent results. The first PCA component was never paradigm-related (showing weak correlations with HRF onset functions) and other paradigm-related PCA components always showed high correlations with the stimulus onsets (union of 45° and 135° stimuli) associated HRF onset function, and not with the single orientations associated HRF onset functions (45° or 135° stimulus alone). Hence, I will only discuss and show results further for the ICA methods.

After the estimation of optimal parameters a, COIs (two for VA, one for FM) were selected from optimal decompositions. Thereby following chapter 3.1.3 components showing maximal correlation with associated HRF onset functions $\tilde{u}_1^{\mathrm{VA}}$, $\tilde{u}_2^{\mathrm{VA}}$ for VA and $\tilde{u}_1^{\mathrm{FM}}$ for FM are chosen as COIs. For ICA decompositions, whose parameter a was estimated on only one half of the data, only the same half was used for COI selection, leaving the unused part for connectivity analysis.

3.3.6 Connectivity between VA and FM COIs

The hypothesis for connectivity between selected COIs stated that VA COIs show higher connectivity to FM's COI if associated stimuli (S1 and S2 for VA COIs) match the previous instruction (I1 and I2). To test the hypothesis I used restricted empirical correlation and DCM (see chapters 2.2.1 and 2.2.2).

As introduced in section 2.2.1 Form. 12, I computed restricted empirical correlations between the COIs of VA and the motor COI, and then took the differences:

$$\Delta_1 := r_{X^{\mathrm{VA}}_{\pi(1)},X^{\mathrm{FM}}_{\pi(1)}}\Big|_{u_5} - r_{X^{\mathrm{VA}}_{\pi(1)},X^{\mathrm{FM}}_{\pi(1)}}\Big|_{u_8} \tag{60}$$

$$\Delta_2 := r_{X^{\mathrm{VA}}_{\pi(2)},X^{\mathrm{FM}}_{\pi(1)}}\Big|_{u_6} - r_{X^{\mathrm{VA}}_{\pi(2)},X^{\mathrm{FM}}_{\pi(1)}}\Big|_{u_7} \tag{61}$$

The hypothesis was that Δ_1 and Δ_2 are both greater than 0, meaning, for example, that correlation between $X^{\mathrm{VA}}_{\pi(1)}$, which is the COI in VA associated to Gabor patch stimulus S1, and motor COI $X^{\mathrm{FM}}_{\pi(1)}$ is higher during I1 instructed trials, than for I2 instructed trials. In the terms of CSCB this hypothesis more conservatively states: $\Delta_1 > \mathrm{CSCB}_{\Delta_1}$ and $\Delta_2 > \mathrm{CSCB}_{\Delta_2}$.

Results for human participants were averaged and presented together with results for synthetic data in Figs. 3.34, 3.35, and 3.36. Differences which were computed using all scans are shown in Fig. 3.34, using only the first half are shown in Fig. 3.35, and using only the second half of scans are shown in Fig. 3.36.

Comparing only the right sides of Figs. 3.34, 3.35, and 3.36 one sees that synthetic data showed large Δ_1 and Δ_2 (about 0.2 to 0.3) which confirms the initial hypothesis. One also sees in Fig. 3.34 that statistical effects caused by component selection had no major effect on the estimated functional connectivity and that differences, Δ_1 and Δ_2, lay highly above their CSCBs (only seen by their deviation bars in Fig. 3.34, right).

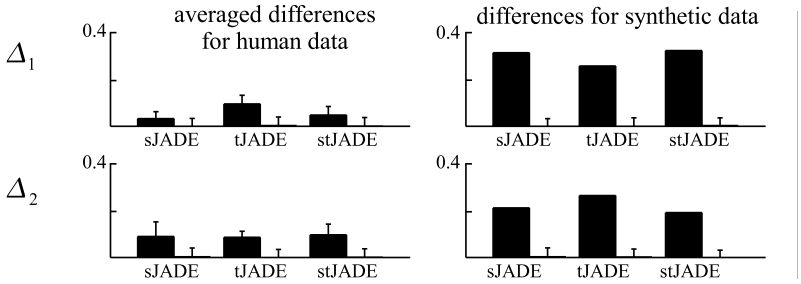

Figure 3.34: Functional connectivity estimates for ORIENT paradigm on the basis of all data. Restricted empirical correlation differences Δ_1 and Δ_2 are computed on the basis of all fMRI scans. Results for the three participants were averaged and the average is presented together with standard deviations on the left side of the Figure (blue bars). Results for synthetic dataset are shown on the right side (blue bars). The standard deviations right to each blue bar represent standard deviations from CSCB, which was computed as the average over the randomly positioned regions.

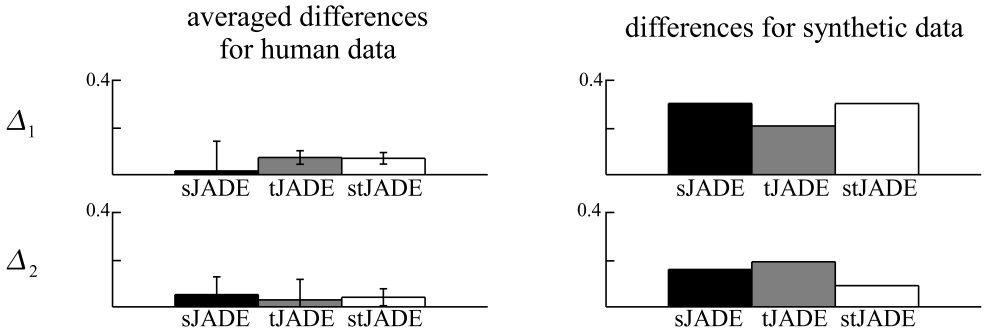

Figure 3.35: Functional connectivity estimates for ORIENT paradigm on the basis of the first datapart. The same results as in Fig. 3.34, now obtained on the basis of the first half of data, are presented without the CSCBs. Because of this, ICA parameter estimation and component selection was performed only using the second half of the scans.

For participants (left parts of Figs. 3.34, 3.35, and 3.36), the situation is not so clear. Only very small (about 0.05 to 0.1) correlation changes Δ_1 and Δ_2 which are of the size fo the CSCB were obtained. In any case, a trend in the direction of positive changes can be seen. None of the differences are negative, which would contradict the hypothesis.

For the DCM connectivity analysis, five models (see Fig. 3.37) were specified and estimated using the SPM5 toolbox. Each model consisted of the two COIs $X^{\mathrm{VA}}_{\pi(1)}$ and $X^{\mathrm{VA}}_{\pi(2)}$ from area VA and motor COI $X^{\mathrm{FM}}_{\pi(1)}$ of region FM and bottom-up connections from VA COIs to FM. Stimulus conditions u_3 and u_4 of the two Gabor stimuli, S1 and S2, excited the associated COIs in VA. The favored models were models II and IV being the simplest models which include bottom-up instruction modulations. For synthetic data model IV which was used to simulate the data is favored.

I would like to remind the reader that positive connectivity and modulation strengths represent excitatory interactions, whereas negative represent inhibitory effects. Estimated and averaged model parameters are presented for the five models in Figs. 3.38 - 3.42.

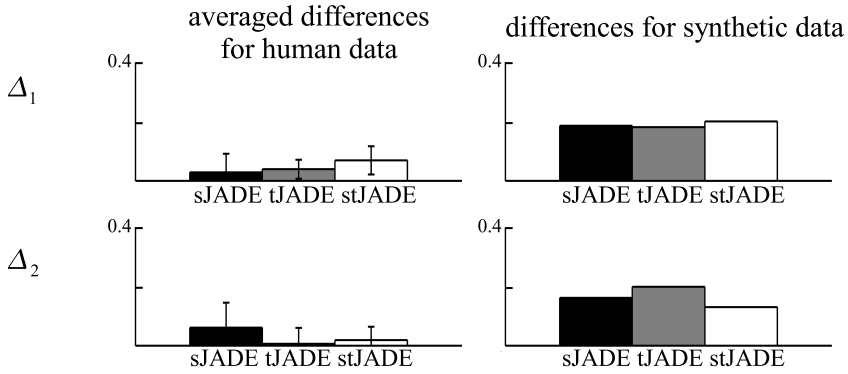

Figure 3.36: Functional connectivity estimates for ORIENT paradigm on the basis of the second datapart. The same results as in Fig. 3.34, now obtained on the basis of the second half of data, are presented without the CSCBs. Thereby ICA parameter estimation and component selection was performed only using the first half of the scans.

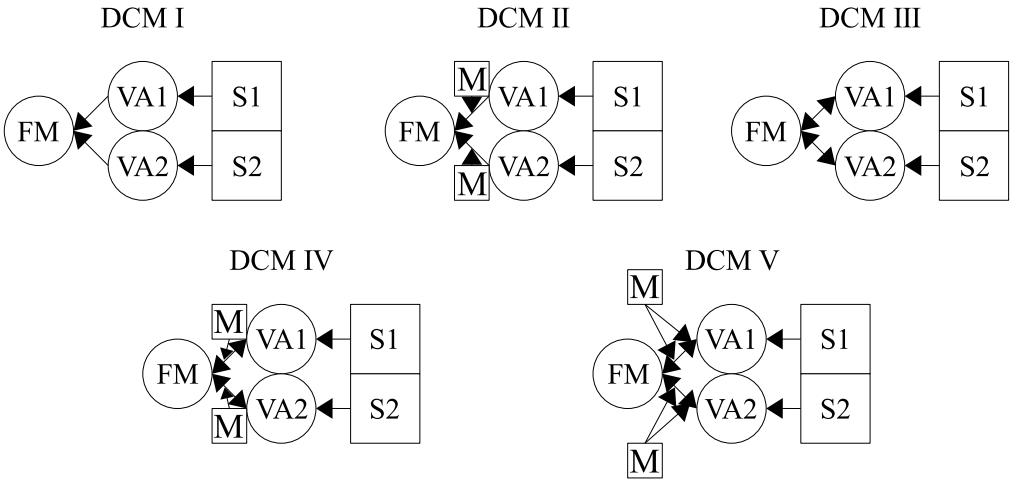

Figure 3.37: Five a-priori dynamic causal models for the ORIENT paradigm. Regions are presented in circles and conditional inputs and modulators in squares. S1 and S2 indicate conditions u_3 (45°) and u_4 (135°) whereas M denotes the associated motor condition: u_5 (I1S1) to the connection between VA1 and FM and u_6 (I2S2) to the connection between VA2 and FM. Models are ordered from simplest (I) to the most complex (V) one.

In general, only weak (about ±0.1) direct, bottom-up connections from VA1 to FM and VA2 to FM for all models were observed. This indicates that these connections alone were not able to explain behavior of the COIs. Of greater interest is the modulation of the bottom-up connections from VA1 and VA2 to FM. As

for correlation analysis, differences between DCM parameters of real fMRI and synthetic data were obtained.

Examining only parameters from human data (upper models in Figs. 3.38 - 3.42) and from models which include the instruction modulations (models II, IV, and V), one sees large modulations (about 0.7) if the models were estimated on the basis of all scans and in most cases very weak modulations if models were estimated on only one half of the data. The inability of ICA decompositions to identify patterns of interest on the basis of the split data might explain these results.

Synthetic data (lower model in Figs. 3.38 - 3.42) shows more consistent results for the three underlying datasets. Models containing the instruction modulation showed large modulation strengths (about 0.7) of the bottom-up connections, independent of the underlying data. This reflects the model used for data generation.

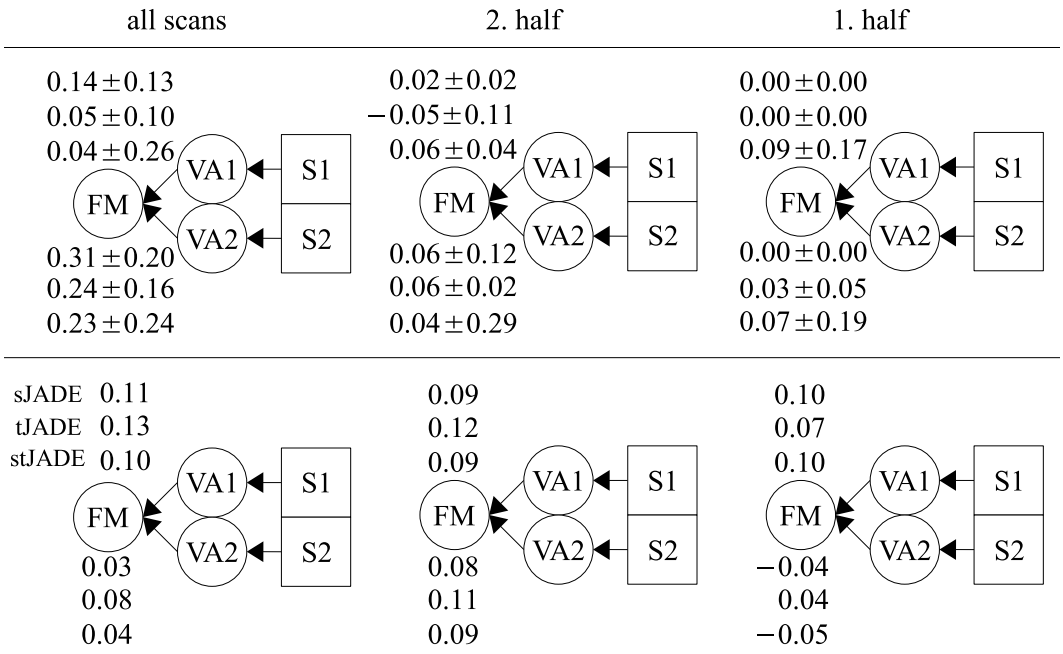

Figure 3.38: Estimated DCM (I) model parameters for ORIENT paradigm. All parameters are in hertz. The estimated and averaged (over the three subjects) model parameters and maximum deviations for model I are shown in the upper half of the figure. Separated by a continuous line, the same estimated model parameters for synthetic data are shown below. The three vertically arranged numbers represent estimated bottom-up connections from VA1 to FM (upper three numbers) and from VA2 to FM (lower three numbers in each model) for the three ICA decomposition methods sJADE, tJADE, and stJADE (from top to bottom). Parameters were estimated on the basis of the entire data (left), second half (middle), and first half (right) of the data. Underlying COIs were therefore selected using the whole, first, and second datapart respectively.

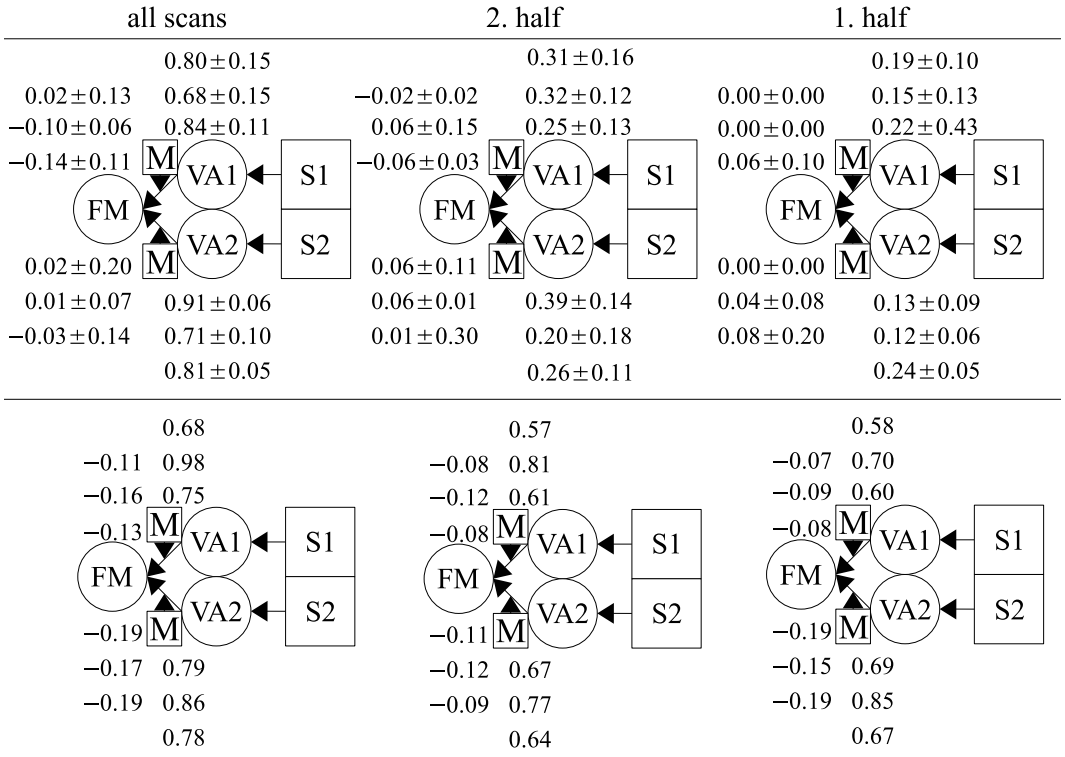

Figure 3.39: Estimated DCM (II) model parameters for ORIENT paradigm. As in 3.38, estimated and averaged DCM model parameters are presented for real (upper half) and synthetic data (lower half). The upper and lower right values in each model are associated with the modulation (M) onto the bottom-up connection from VA1 and VA2 to FM (upper and lower left numbers).

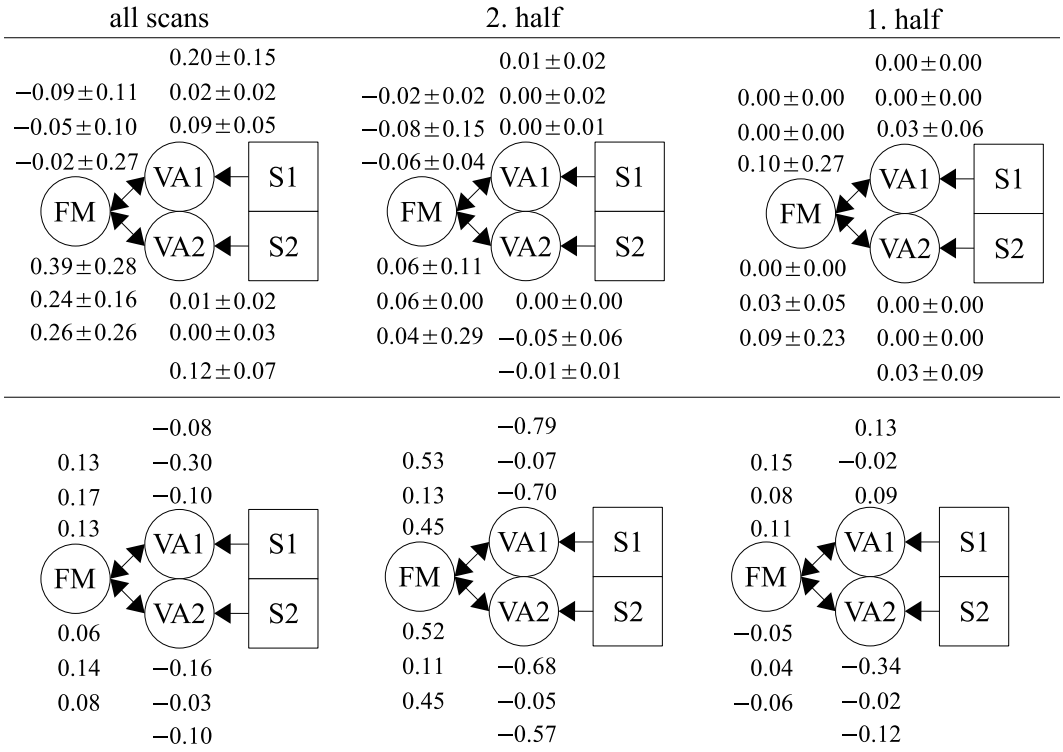

Figure 3.40: Estimated DCM (III) model parameters for ORIENT paradigm. As in 3.38, estimated and averaged DCM model parameters are presented for real (upper half) and synthetic data (lower half). The upper and lower right values for each model are associated with top-down connection from FM to VA1 and VA2.

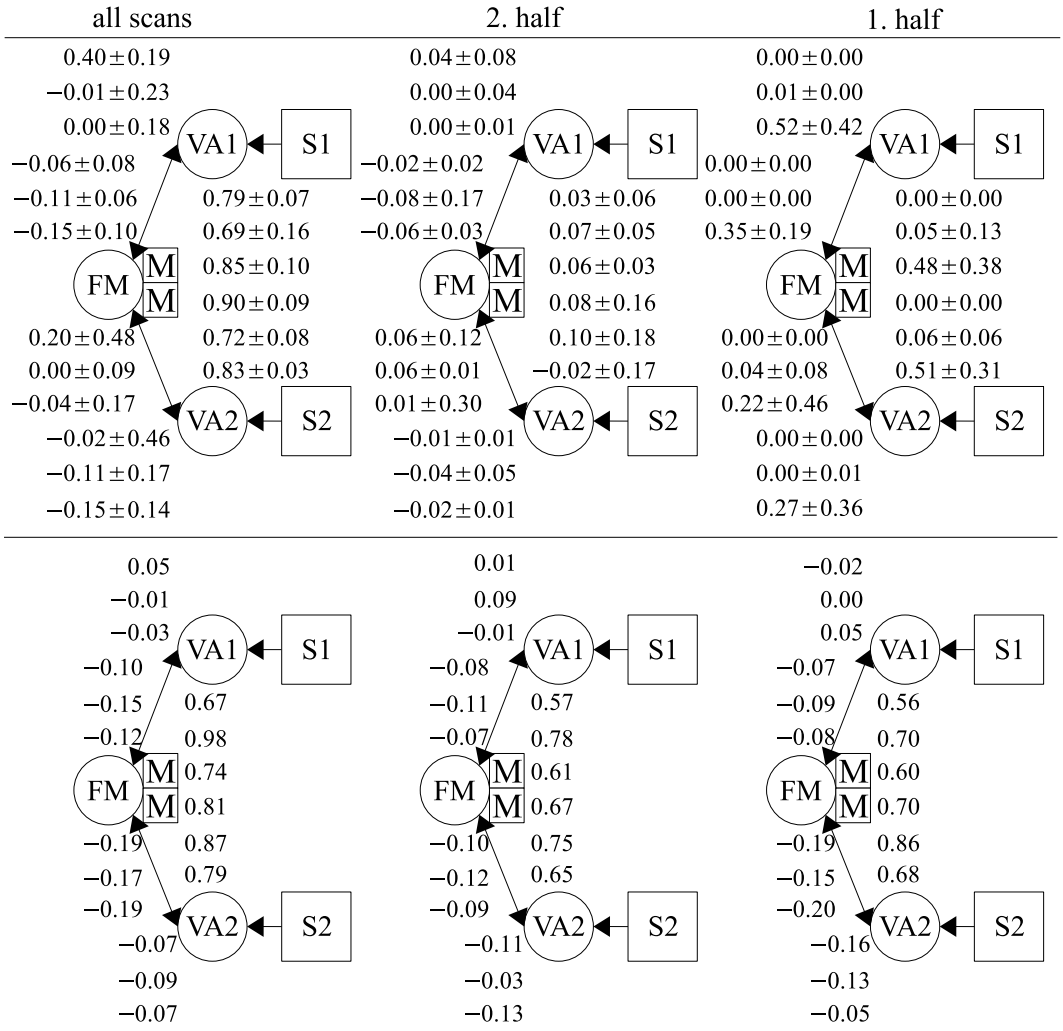

Figure 3.41: Estimated DCM (IV) model parameters for ORIENT paradigm. As in 3.38, estimated and averaged DCM model parameters are presented for real (upper half) and synthetic data (lower half). For each model the two most left number blocks represent bottom-up (left) and top-down (right) connections from VA1 and VA2 to FM. The central blocks in each model represent modulation (M) strengths.

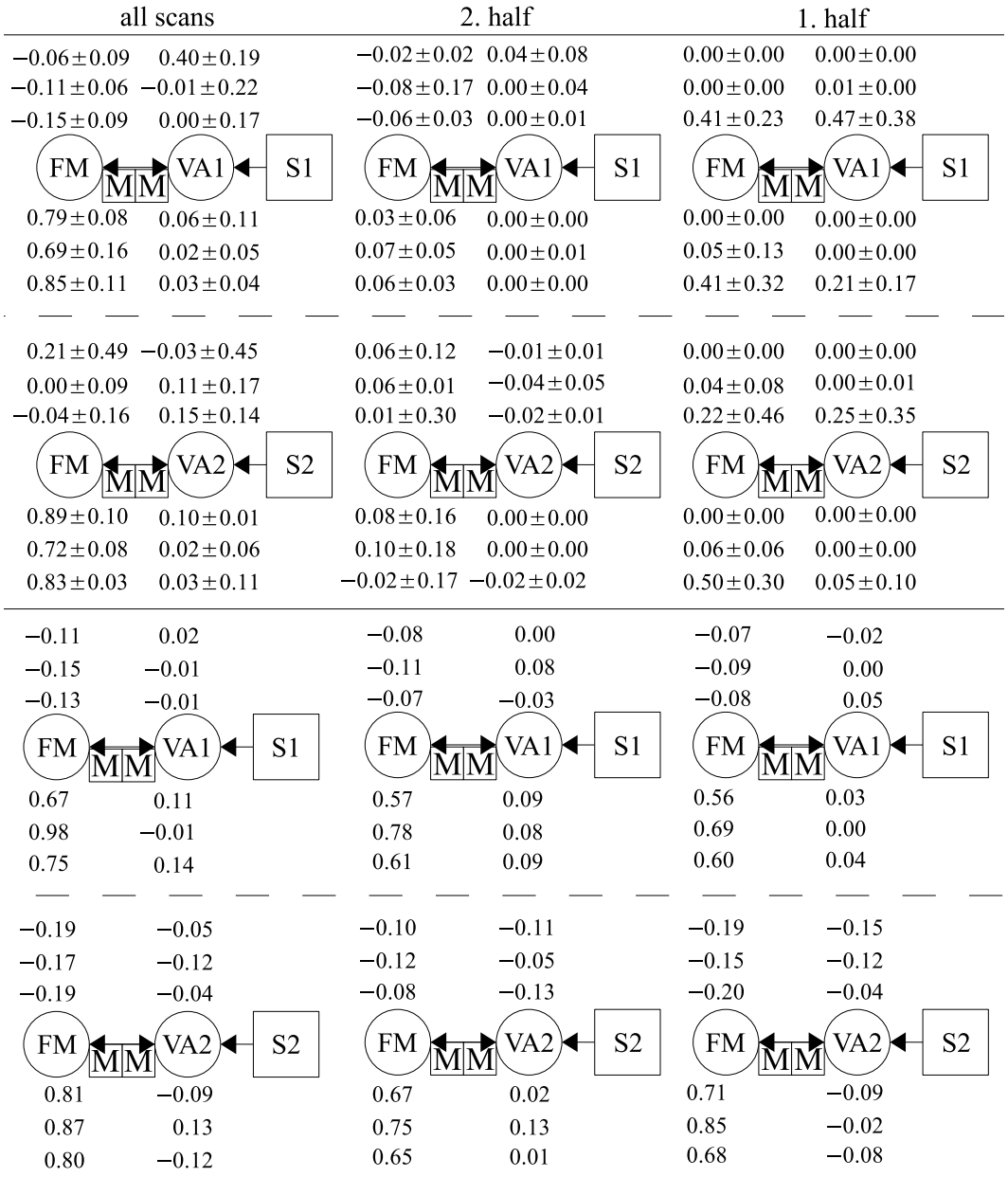

Figure 3.42: Estimated DCM (V) model parameters for ORIENT paradigm. As in 3.38, estimated and averaged DCM model parameters are presented for real (upper half) and synthetic data (lower half). For a better overview the connection between VA1 and FM (upper half of the figure) was separated from connection between VA2 and FM (lower half) divided by the dashed line. In each model upper numbers represent bottom-up (left) and top-down (right) connectivity strengths. The lower numbers represent modulation (M) effects onto bottom-up (left) and onto top-down (right) connections.

Subsequent to the estimation, all models were compared pairwise. Following section 2.2.2 the positive evidence ratios were computed for all model comparisons. Results for real and synthetic data are shown in Tab. 13.

		all scans					2nd half					1st half				
Decomp.	M	I	II	III	IV	V	I	II	III	IV	V	I	II	III	IV	V
sJADE	I	**4.**	0	2	0	0	**2.**	1	3	3	3	**2.**	0	3	3	3
	II	3	**1.**	3	2	2	2	**1.**	2	3	3	2	**1.**	2	3	3
	III	0	0	**5.**	0	0	0	1	**3.**	3	3	0	1	**3.**	3	3
	IV	3	1	3	**2.**	3	0	0	0	**4.**	3	0	0	0	**4.**	3
	V	3	0	3	0	**3.**	0	0	0	0	**5.**	0	0	0	0	**5.**
tJADE	I	**4.**	0	3	0	0	**2.**	0	3	3	3	**2.**	1	3	3	3
	II	3	**1.**	3	3	3	2	**1.**	2	3	3	2	**1.**	3	3	3
	III	0	0	**5.**	0	0	0	1	**3.**	3	3	0	0	**3.**	3	3
	IV	2	0	3	**2.**	3	0	0	0	**4.**	3	0	0	0	**4.**	3
	V	2	0	2	0	**3.**	0	0	0	0	**5.**	0	0	0	0	**5.**
stJADE	I	**4.**	0	3	0	0	**1.**	2	3	3	3	**3.**	1	3	1	1
	II	3	**1.**	3	2	3	1	**2.**	3	3	3	1	**3.**	3	1	1
	III	0	0	**5.**	0	0	0	0	**3.**	2	3	0	0	**4.**	1	1
	IV	3	0	3	**2.**	3	0	0	0	**4.**	3	2	2	2	**1.**	3
	V	3	0	3	0	**3.**	0	0	0	0	**5.**	2	2	2	0	**2.**
sJADE	I	**4.**	0	1	0	0	**5.**	0	0	0	0	**4.**	0	0	0	0
	II	1	**1.**	1	1	1	1	**1.**	1	1	1	1	**1.**	1	1	1
	III	0	0	**5.**	0	0	1	0	**4.**	0	0	0	0	**4.**	0	0
	IV	1	0	1	**2.**	1	1	0	1	**2.**	1	1	0	1	**2.**	1
	V	1	0	1	0	**3.**	1	0	1	0	**3.**	1	0	1	0	**3.**
tJADE	I	**4.**	0	1	0	0	**4.**	0	1	0	0	**4.**	0	1	0	0
	II	1	**1.**	1	1	1	1	**1.**	1	1	1	1	**1.**	1	1	1
	III	0	0	**5.**	0	0	0	0	**5.**	0	0	0	0	**5.**	0	0
	IV	1	0	1	**2.**	1	1	0	1	**2.**	1	1	0	1	**2.**	1
	V	1	0	1	0	**3.**	1	0	1	0	**3.**	1	0	1	0	**3.**
stJADE	I	**4.**	0	1	0	0	**5.**	0	0	0	0	**4.**	0	1	0	0
	II	1	**1.**	1	1	1	1	**1.**	1	1	1	1	**1.**	1	1	1
	III	0	0	**5.**	0	0	1	0	**4.**	0	0	0	0	**5.**	0	0
	IV	1	0	1	**2.**	1	1	0	1	**2.**	1	1	0	1	**2.**	1
	V	1	0	1	0	3.	1	0	1	0	**3.**	1	0	1	0	**3.**

Table 13: Positive evidence ratios for DCM models. DCM comparison results for real fMRI (upper half) and for synthetic data (lower half) is presented. Each number gives the wins of the row model against the column model over the three subjects, for real fMRI data (wins range from 0 to 3) and the single comparison for synthetic data (wins range from 0 to 1). Only models using the same part of the data and the same decomposition method were compared against each other. Bold numbers on the diagonals give the rank of a model in the model hierarchy determined as described in section 2.2.2.

Although model hierarchy slightly varies over ICA methods and underlying data,

by comparing the rank of the models (diagonal bold numbers in Tab. 13) one clearly sees that models containing the instruction modulator onto the bottom-up connections from VA1 and VA2 to FM (these are models II, IV, and V) are favored over models without modulation of the bottom-up connections. This can be seen for real and synthetic data, except for stJADE on the basis of the 2nd half of the data, where the model I is slightly better as model II. This confirms the initial DCM hypothesis for the human data that, for example, if participants were instructed to press the button if stimulus S1 is shown (I1), effective connectivity increases from VA1 to FM if the stimulus S1 was actually presented.

For synthetic data, model IV was favored (1st rank) if models had been estimated on the basis of all or the 2nd half of scans. On the basis of the 1st half, model V was favored. Due to the fact that model V differs from model IV only in the bottom-down connections and modulations, and that these connections and modulations in model V showed only very weak effect strengths (about 0.1) compared to the bottom-up modulation (about 0.7), I conclude that the model used for creation of the synthetic data could have been replicated and that ICA had been able to identify the used patterns.

In the same way as for the BMS paradigm (compare section 3.2.4 on page 63), CSCB DCM model parameters were estimated for model IV. On the basis of all scans and the 200 randomly positioned regions, 100 dynamic causal models were estimated. For each model now the three COIs obtained from randomized located regions replace the three COIs of ROIs VA and FM. The estimated mean parameters over the 100 DCMs are presented in Fig. 3.43.

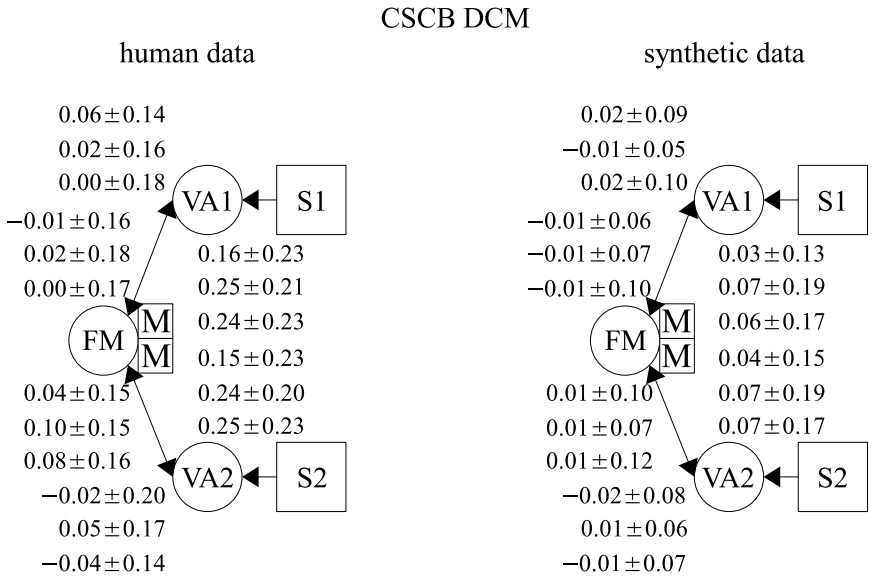

Figure 3.43: Mean CSCB DCM (IV) model parameters for ORIENT paradigm. As in 3.41, estimated and averaged DCM model parameters shown in the same way. The left model shows averaged (over the 100 models and the three human subjects) CSCB DCM model parameters. The right model presents the mean CSCB DCM parameters over the 100 DCMs for synthetic data. For both models, standard deviations are shown.

One sees that parameter deviations are comparable to parameter sizes which points, as for the BMS experiment, to an unstable estimation process of the DCM parameters, reflecting the random localization of the used regions. Most importantly one sees, for human data on the basis of all scans and for synthetic data independent of the underlying data, that the found motion modulations of the favored model IV from Fig. 3.21 are higher than their component selection connectivity baselines.

3.3.7 Summary

With the help of the ORIENT paradigm, I illustrated how the concept of pattern connectivity is applied, if a ROI's behavior can not be captured with a single time course. For area VA, I demonstrated how the fitness function for two COIs (see Eq. 59) was used to identify optimal ICA parameters and how COIs were selected from the optimal ICA decomposition.

The standard PCA method was not applicable to test the connectivity hypothesis in this case. To validate results found with pattern connectivity, a simple network of three patterns (VA1, VA2, and FM) with self-evident connectivity structure (see hypothesis for the ORIENT paradigm) was chosen. In addition, synthetic fMRI data was genergated, using DCM's bilinear model (compare section 2.2.2) to simulate BOLD responses on the basis of one of the real subject's onset functions. Pattern connectivity revealed the initially used connectivity structure, used for data generation.

Connectivity measures, restricted empirical correlation and dynamic causal modeling, were used to analyze connectivity for real and synthetic data.

For the real fMRI data, restricted empirical correlations showed only weak results, which tend to support the initial hypothesis. In general, found correlation changes were not above the estimated statistical baseline. Results for synthetically-generated data were consistent with information used to create it, and showed large correlation changes between VA1, VA2, and FM dependent on simulated instructions. All results lie well above statistically expected values for the synthetically generated data set.

DCM analysis yielded unambiguous results for synthetic fMRI data. The obtained model hierarchy and estimated model parameters revealed the used model for data creation. This was confirmed by the comparison of the estimated CSCB for model parameters with the actual obtained model parameters.

Weak results from DCM analysis of human data on the basis of the split data suggest that here ICA was unable to identify POIs. Considering only the DCM results from human data on the basis of all scans, strong instruction modulation for all three ICA methods were obtained. Together with the found model hierarchy and the low CSCB values of the favored model, the strong instruction modulations support the initial DCM hypothesis and imply that the ICA algorithms were able to identify patterns of interest if all data was used.

From the ORIENT paradigm, I conclude that ICA algorithms together with the proposed selection steps were able to determine the two POIs in region VA and that pattern connectivity was successfully used to analyze neuronal connectivity, for several patterns contained inside one area, on the basis of fMRI data, which

was the major goal of the ORIENT experiment stated at the beginning.

4 Discussion, summary, and future prospects

4.1 Discussion

One question that probably arises when first confronted with the concept of pattern connectivity is why one uses ICA to decompose a ROI into several patterns, although PCA itself provides more than one component. Concerning this topic, I want to state that the key idea of pattern connectivity is not particularly to use ICA instead of PCA, but to apply connectivity analysis methods onto patterns instead of single time courses for each ROI. Independent component analysis was chosen because it yields a more natural criterion (the stochastic independence of the components) for data decomposition than PCA (orthogonal components explaining maximum remaining variance). Therefore connectivity studies of PCA components can also be seen as pattern connectivity even if the method seems inappropriate for extracting of more than one COI for a region.

On the one hand, if more than the first eigenvariate of a PCA decomposition is used one has to be careful with interpretation of the connectivity results of these components. On the other hand, as one saw in the ORIENT paradigm, PCA tends to merge the two patterns together into one pattern, representing the overall stimulus and not the two orientations.

As well as using the same decomposition method (PCA, ICA, etc.) for all regions of a connectivity study one can also use different methods for different regions. For example, using the first PCA eigenvariate for regions with only one POI and ICA components to represent more complex behavior of other regions. However, different scaling and other properties of the components such as, for example, the independence of ICA components have to be considered and treated carefully, so the same decomposition method should be used in general for all involved ROIs.

The application of ICA on fMRI data is not new. A common use of ICA is to determine, and then eliminate, sources of noise and artifacts (e.g. [21] [147]). Here, ICA is applied on the whole brain in a first step. Known artifacts and noise components are selected and discarded from extracted components. The remaining components are used to form a new data matrix for further analysis. Another frequent application is the study of the so-called default mode network during resting state (e.g. [142] [141] [23] [167]). Hereby, ICA is applied onto the whole brain again and one searches for differences between healthy (or young) participants and impaired (or old) participants (e.g. [171] [127]). Also correlations between ICA components and HRF onset functions were used [103] [91] to separate noise from paradigm-related components or to distinguish task-related from default mode network components [22]. However, in no previous study, to the best of the author's knowledge, has ICA been applied onto single brain areas to determine time courses of multi-variate pattern and study their connectivity, nor has any study, so far, addressed or solved the methodical problems, arising for neuronal connectivity (compare section 3.1.4) through component selection.

As mentioned in section 3.1.3, some algorithms have been developed to determine the optimal number of components P for ICA decompositions, e.g. based on minimum description length (MDL) [132]. An implementation of this MDL estimator into the MFBOX toolbox (Computational Intelligence and Machine Learning

Group at the Institute of Biophysics, University of Regensburg, Germany) has been tested for the BMS data, but suggested a large number of about $70 - 80$ components for all ROIs and subjects. These parameters also yielded only decompositions with very small fitness values F so that they were ignored during further analysis and ICA parameters were estimated in the proposed generic way.

In almost all cases the three different ICA methods sJADE, tJADE, and stJADE yielded comparable results. In particular the temporal ICA variant tJADE, which searches for stochastically independent COIs, shows almost the same results as the spatial variant sJADE, which searches for independent spatial patterns. As stated in section 3.1.2, I in fact assume temporal (third assumption about non-overlapping time courses) and spatial independence (fourth assumption about independent spatial patterns) between patterns. This might be the reason why all three ICA variants yielded consistent results.

In section 3.1.3, Form. 35 on page 36, a fitness function F for the estimation of optimal ICA parameters was introduced. I will now discuss an alternative form of this fitness functions. A parameter a was said to be *good* if the ICA decomposition it provided contained paradigm-related components. For the proposed fitness function, paradigm-related meant that one could find independent components which show high correlation with the associated HRF onset functions of a ROI (compare section 3.1.3). Instead of correlation, I could have also used mutual information [107], which would not only account for variance of the two distributions, but also for higher stochastic central moments [73]. However, tests, using estimated mutual information approximated with an algorithm proposed in [107] instead of correlation, provided self-inconsistent results. From the author's point of view, the main reason for the poor approximation of mutual information lay in the small number of data points (functional scans).

Besides the two used connectivity analysis methods - restricted correlation and DCM - several other methods to study connectivity exist and were mentioned in section 2.2.1. I want to discuss why these two methods were preferred above the other ones. First of all, using correlation provides a very simple and intuitive measure of functional connectivity not stating any additional conditions for underlying data. On the contrary, dynamic causal modeling is a very complex method, comprehending a neuronal level and a sophisticated model for the BOLD response, highlighting effective connectivity. So with these two, I have an example of a simple and a complex technique to study functional and effective connectivity. Secondly, the different stimulus to peak delays of HRF responses of different regions (compare section 2.1.2) complicate the interpretation of results obtained by methods not modeling a region-specific HRF. This is especially valid for methods using Granger causality, which explicitly use temporal delays. After all, due to strong a-priori knowledge of the underlying connectivities for the BMS and ORIENT paradigms, and the stated goals, this thesis has a rather confirmatory than exploratory nature, making DCM the preferred method over Granger causality or coherency [144].

Finally, I will address the poor results of Pearson's correlation connectivity analysis of the real fMRI data from the ORIENT paradigm. Only very weak effects near connectivity baseline were detected (compare Fig. 3.34, 3.35, and 3.36 on page 81). The main reason for this may be the event-related design of the ORI-

ENT paradigm. Due to the relatively short presentation time of 1.5 s for the Gabor patches, the shape of the evoked HRF response plays an important role. For the BMS experiment, where I had a block design and stimulations of 20 s, BOLD responses in regions VA and MA reach a saturated level after several seconds. The differences between baseline activation and stimulus activation of the regions now lead to the strong correlation differences, during the different stimulations obtained in the BMS experiment. In the ORIENT paradigm it is very unlikely that BOLD responses caused by the Gabor patches did reach saturation. Therefore the shape of the hemodynamic response function plays a major role and because Pearson's correlation does not account for HRF's shape, but DCM does, I obtain the hypothesized results for DCM, but Pearson's correlation is not able to identify connectivity changes. The fact that for synthetic data these differences dependent on underlying data can not be observed, might be caused through additional noise and artifact terms in the real fMRI data.

4.2 Summary

I was able to show that for fMRI data, it is possible to study neuronal connectivity between multi-variate patterns instead of brain regions. The concept of pattern connectivity, which allowed these analyses, was theoretically introduced and applied to two fMRI paradigms and synthetic fMRI data. This new approach enables the application of neuronal connectivity analysis techniques to multi-voxel patterns instead of brain regions, by replacing the single PCA eigenvariate representation for each region with a representation of multiple paradigm-related components. Solutions for arising problems - due to methodical artifacts, caused by component selection - were introduced and illustrated during the analysis of the fMRI paradigms.

With the help of the BMS paradigm I was able to compare connectivity results, obtained using the standard PCA method with those results obtained using pattern connectivity. Both methods showed comparable results for the two applied connectivity analysis methods of correlation and dynamic causal modeling. Results were in agreement with hypothesized neuronal connectivity structures. I conclude that pattern connectivity can replicate connectivity analysis results obtained with the standard PCA method. That was the major goal of the BMS study.

Aim of the ORIENT fMRI study was to illustrate potentials of pattern connectivity, by investigating a more complex situation with more than one pattern per brain area. Unfortunately, connectivity results for real fMRI data using empirical correlation were weak, and did not differ significantly from the estimated connectivity baseline. The potential reasons for this were laid out in the discussion section. For synthetic fMRI data, empirical correlation showed large connectivity changes, which were in agreement with the information used for data creation. In contrast to Pearson's correlation, DCM analysis of real fMRI data revealed the hypothesized connectivity changes. This implies that for the ROI VA, which contained two POIs, ICA methods were able to find and separate the components of interest. One saw a clear hierarchy for the DCM models, which supported the connectivity hypothesis. This was the first major goal of the ORIENT study. A similar hierarchy was found for synthetic data, replicating the connectivity struc-

ture which was used to simulate of artificial data. This was the second major goal of the ORIENT study (compare beginning of section 3.3).

I conclude that pattern connectivity, as a generalization of the state of the art PCA method, is able to replicate results found with the standard method and furthermore can be applied to study neuronal connectivity between multi-variate patterns of fMRI data, revealing the underlying connectivity structure. Finally, I state that the approach of pattern connectivity has proven a valid alternative along side the PCA method, and opens the field of multi-voxel pattern analysis for neuronal connectivity studies.

4.3 Future Prospects

Although pattern connectivity has proven to be applicable onto fMRI data, and to give interesting new insights into connectivity structures between MVP of brain areas so far, there are still numerous ways in which the concept can be extended.

Besides restricted empirical correlation and dynamic causal modeling, different techniques to study connectivity may be applied to analyze other connectivity properties (see section 2.2.1). Also other neuronal networks comprising more complex connectivity structures as the used ones can be analyzed. Limitations to those two fields are only given by current state connectivity analysis methods, and the ability to distinguish components of interest (compare section about MVPs 2.3.1).

A possible modification of the concept would be to use other ICA decompositions than the ones used here or even decomposition techniques using other constraints than stochastical independence of components such as, for example, non-negative matrix factorization (NMF) [87] [111].

From the author's point of view, the most interesting next methodical step is to use information time courses obtained with support vector machines (SVM) (compare section 2.3.1) rather than components of matrix decompositions to represent behavior of brain patterns. Thereby the COIs now selected from ICA decomposition (or other model free matrix decompositions) are replaced by time courses reflecting the actual information content about a stimulus or task inside a brain area. Considering one ROI and two stimuli u_1 and u_2, such as, for example, region VA and Gabor stimuli S1 and S2 in the ORIENT paradigm, the information content of a specific scan can be represented as the probability that during this scan stimulus u_1 (or u_2) was presented. These probabilities can be estimated for a scan using support vector machines or similar classification methods, by determining how often the scan was classified to belong to u_1 or u_2. One can therefore study dependencies and interactions between those probability time courses.

One advantage of this approach would be that the selection of components, which goes along with a statistical offsets for neuronal connectivity, is avoided. But the major advantage would be that one can allow overlapping onset functions for different patterns of interest. This was forbidden in assumption three in section 3.1.2 in which I needed non-overlapping onsets of different POIs to assure the linear structure a regions data Y^I. This variant of pattern connectivity does not use ICA or other matrix decompositions, which would need the linear structure. However, new problems, for example, the applicability of current connectivity analysis methods and interpretation of their results have to be handled, and the

role of the HRF also has to be revisited.

5 Appendix

5.1 GLM contrasts for BMS and ORIENT paradigms

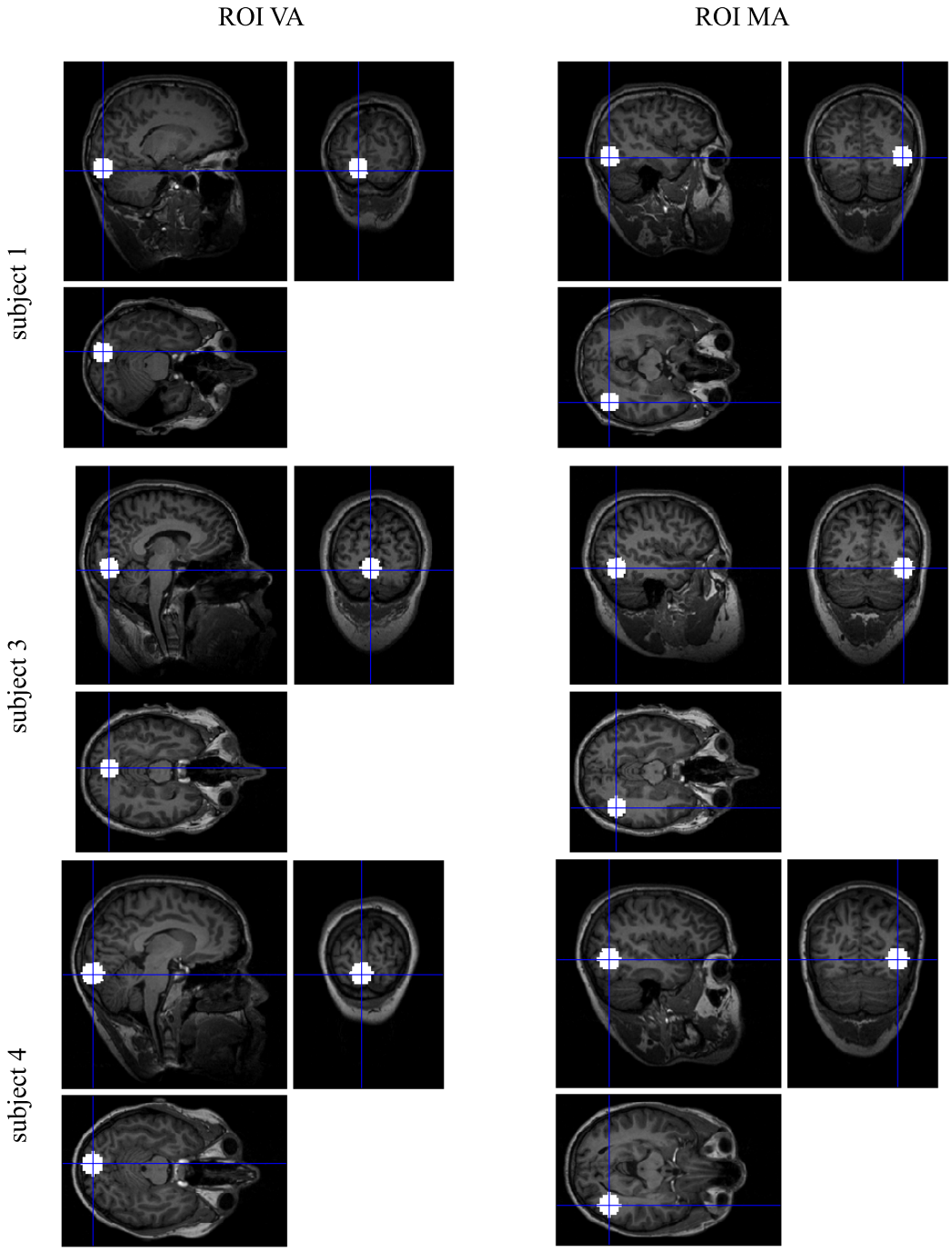

Figure 5.1: ROIs for subjects 1, 3, and 4 for BMS paradigm.

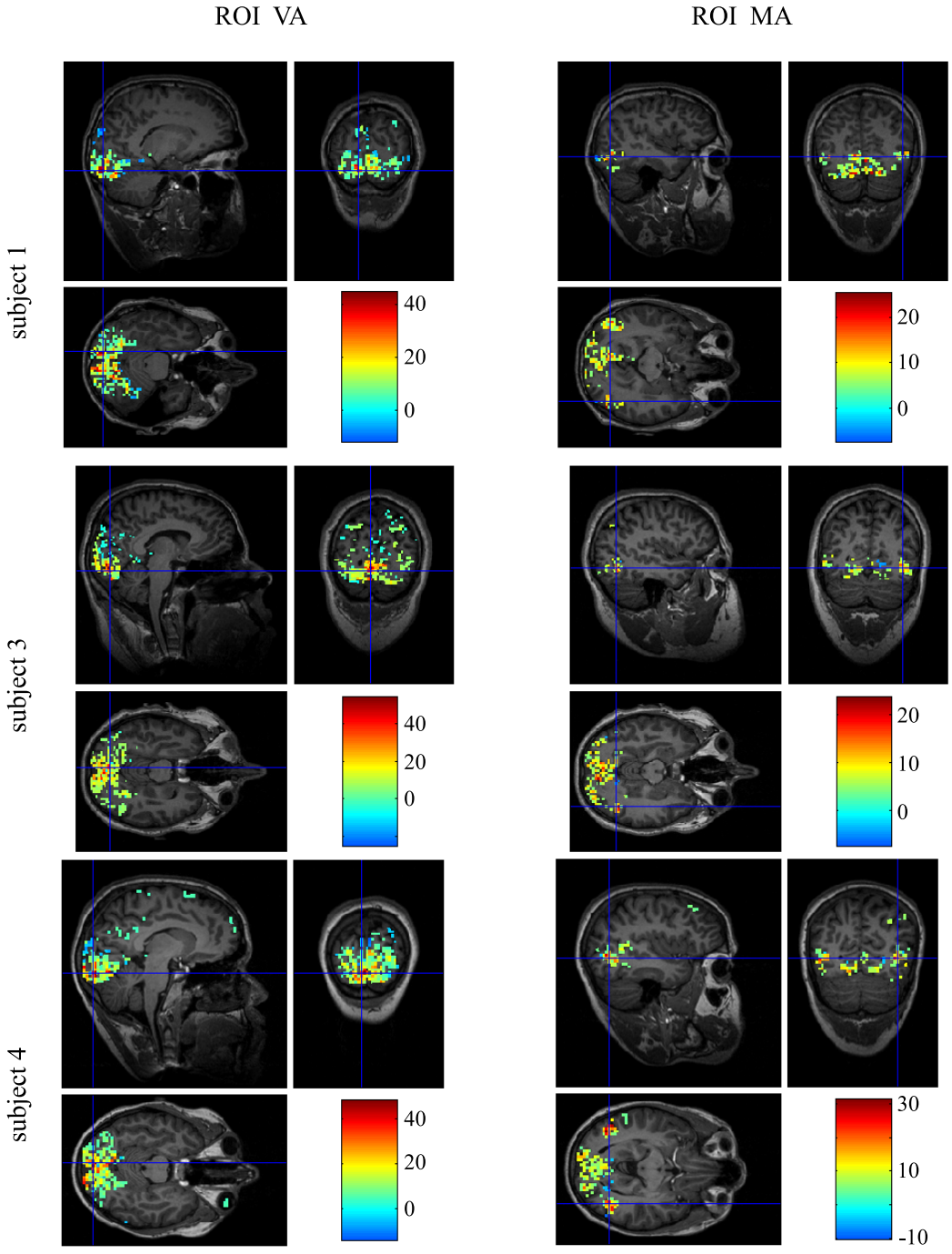

Figure 5.2: GLM visual and motion contrasts for BMS paradigm on raw data.

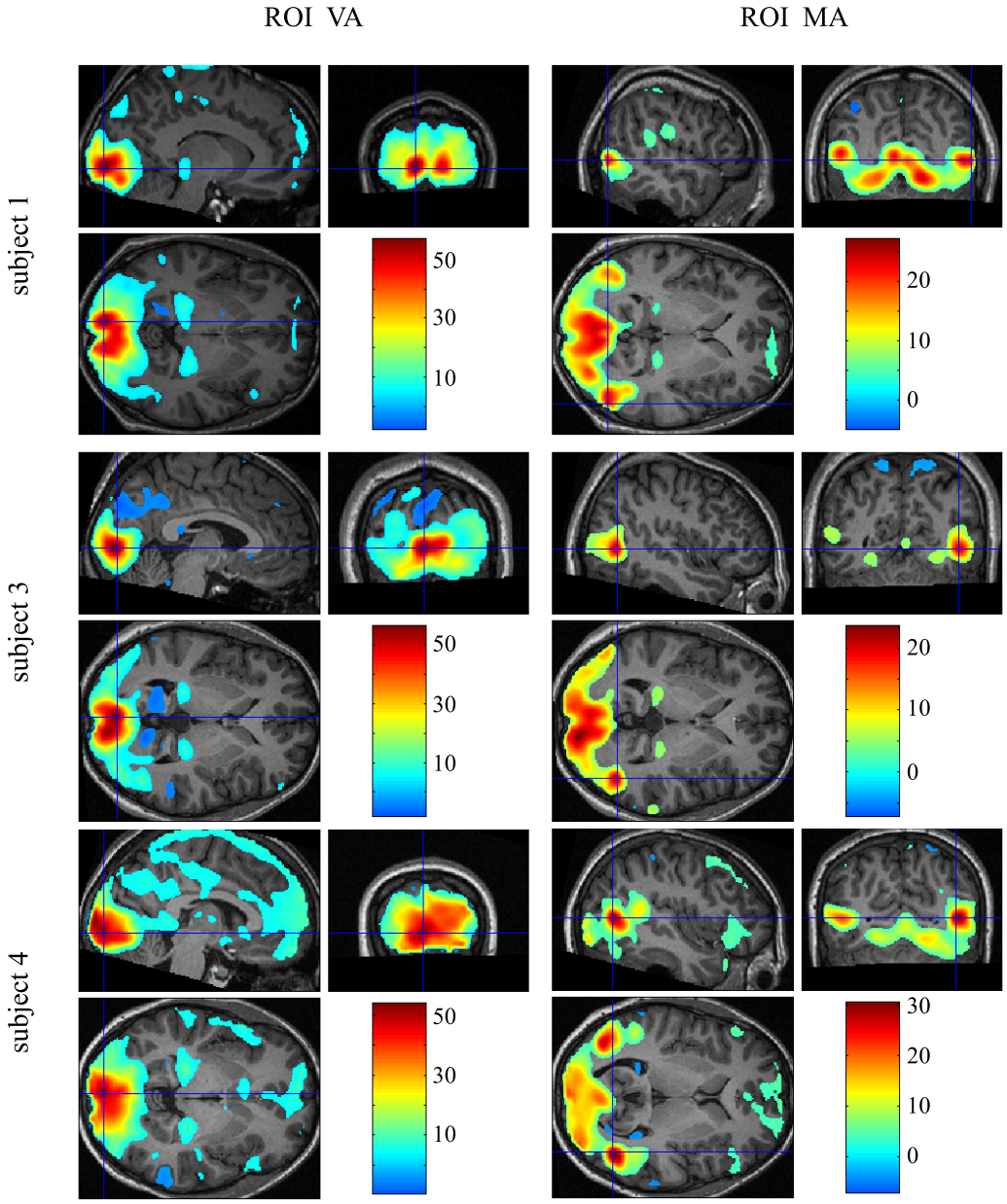

Figure 5.3: GLM visual and motion contrasts for BMS paradigm on smoothed data.

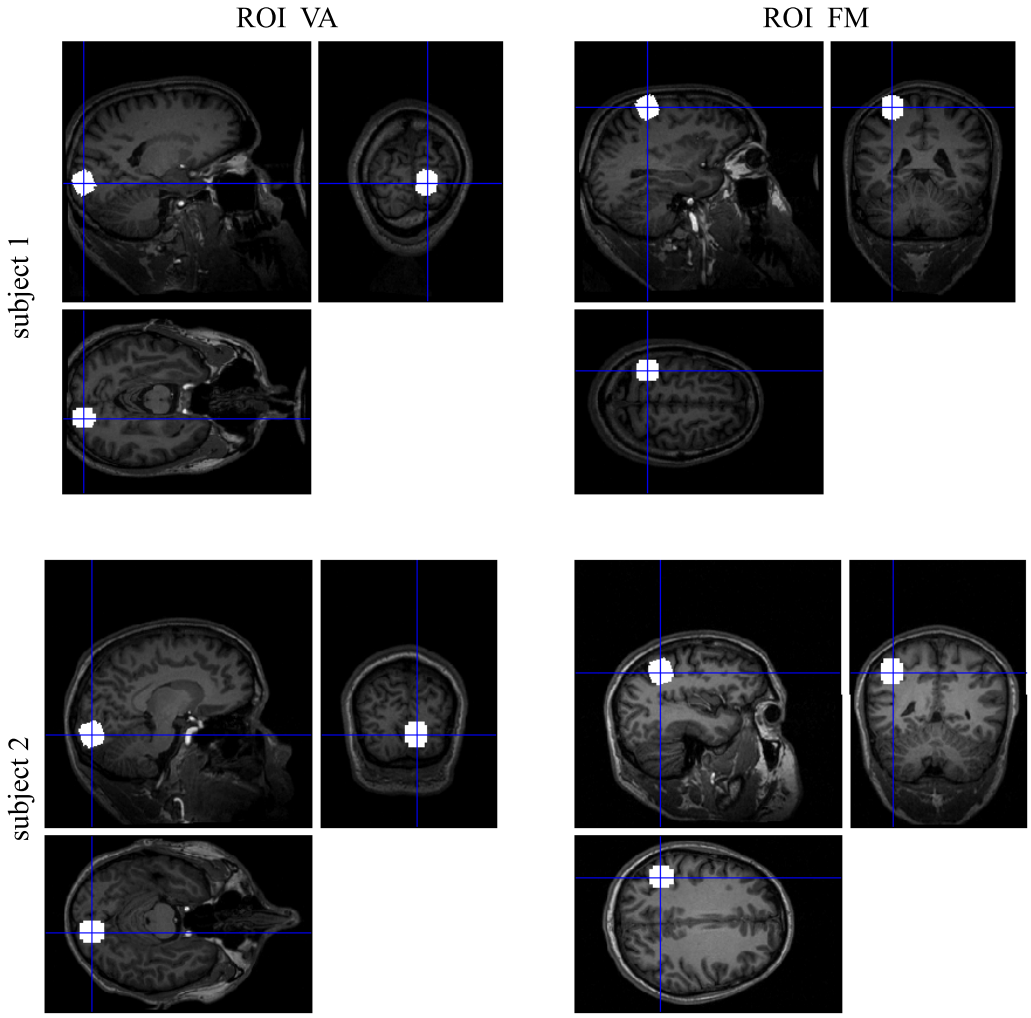

Figure 5.4: ROIs for subjects 1 and 2 for ORIENT paradigm.

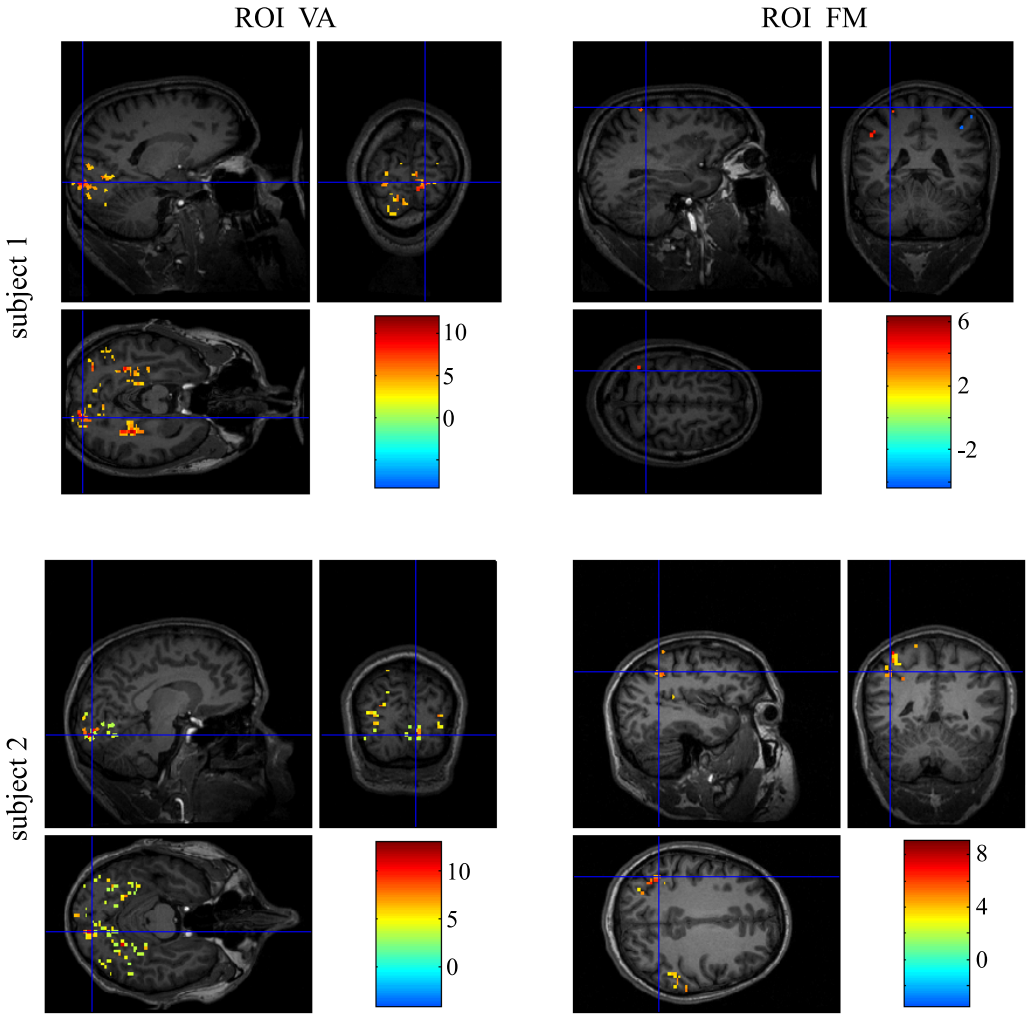

Figure 5.5: GLM visual and motor contrasts ORIENT paradigm on raw data.

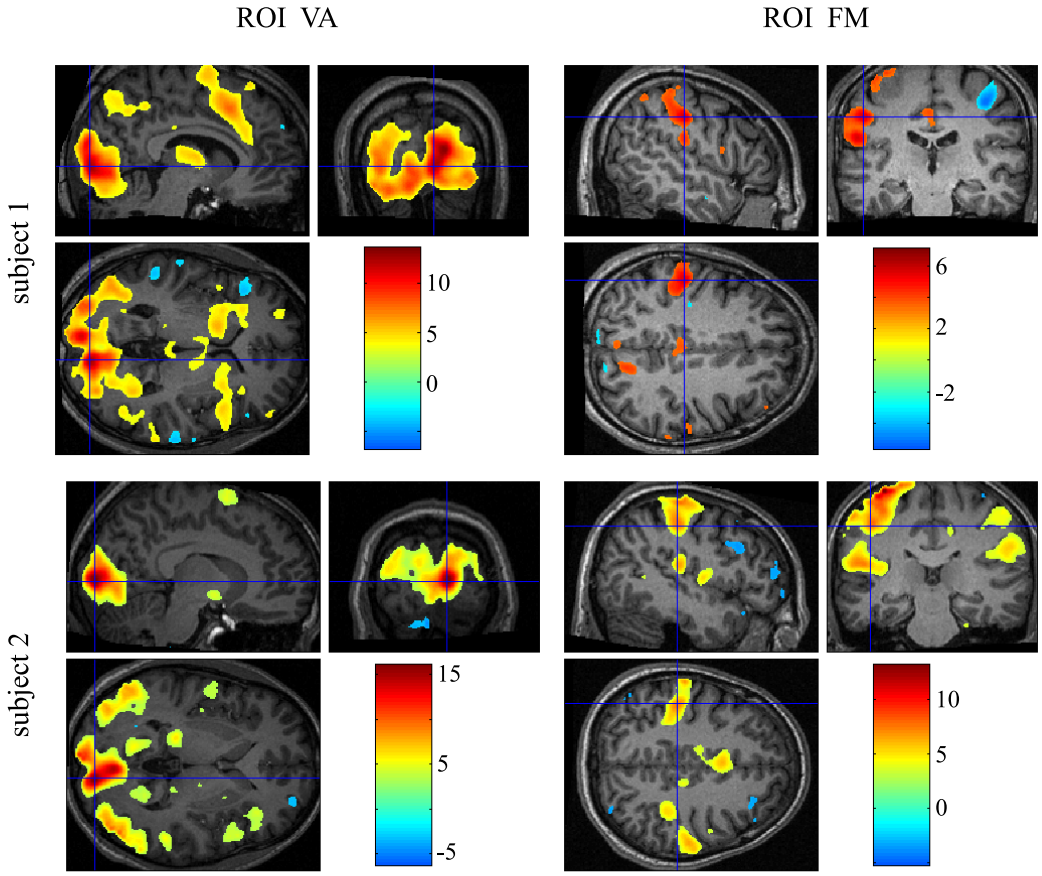

Figure 5.6: GLM visual and motor contrasts ORIENT paradigm on smoothed data.

List of Figures

List of Tables

Index

References

[1] G.K. Aguirre, E. Zarahn, and M. D'Esposito. The variability of human, BOLD hemodynamic responses. *Neuroimage*, 8(4):360–369, 1998.

[2] H. Akaike. A new look at the statistical model identification. *IEEE Trans Automat Contr*, AC-19:716–723, 1974.

[3] P. Allen, K.E. Stephan, A. Mechelli, F. Day, N. Ward, J. Dalton, S.C. Williams, and P. McGuire. Cingulate activity and fronto-temporal connectivity in people with prodromal signs of psychosis. *Neuroimage*, 49(1):947–955, 2010.

[4] R. Almeida and M. Stetter. Modeling the link between functional imaging and neuronal activity: synaptic metabolic demand and spike rates. *Neuroimage*, 17(2):1065–1079, 2002.

[5] A. Anzai, X. Peng, and D.C. Van Essen. Neurons in monkey visual area V2 encode combinations of orientations. *Nat Neurosci*, 10(10):1313–1321, 2007.

[6] D. Attwell and C. Iadecola. The neural basis of functional brain imaging signals. *Trends Neurosci*, 25(12):621–625, 2002.

[7] L.A. Baccalá and K. Sameshima. Partial directed coherence: a new concept in neural structure determination. *Biol Cybern*, 84(6):463–474, 2001.

[8] L. Barnett, A.B. Barrett, and A.K. Seth. Granger causality and transfer entropy are equivalent for Gaussian variables. *Phys Rev Lett*, 103(23):238701, 2009.

[9] M.S. Beauchamp, S. Laconte, and N. Yasar. Distributed representation of single touches in somatosensory and visual cortex. *Hum Brain Mapp*, 30(10):3163–3171, 2009.

[10] J.W. Belliveau, D.N. Jr. Kennedy, R.C. McKinstry, B.R. Buchbinder, R.M. Weisskoff, M.S. Cohen, J.M. Vevea, T.J. Brady, and B.R. Rosen. Functional mapping of the human visual cortex by magnetic resonance imaging. *Science*, 254(5032):716–719, 1991.

[11] A. Belouchrani, K. Abed-Meraim, J.-F. Cardoso, and E. Moulines. Second-order blind separation of temporally correlated sources. *Proc Int Conf Digital Sig Proc*, pages 346–351, 1993.

[12] T. Bitan, J.R. Booth, J. Choy, D.D. Burman, D.R. Gitelman, and M.M. Mesulam. Shifts of effective connectivity within a language network during rhyming and spelling. *J Neurosci*, 25(22):5397–5403, 2005.

[13] G.G. Blasdel. Orientation selectivity, preference, and continuity in monkey striate cortex. *J Neurosci*, 12(8):3139–3161, 1992.

[14] F. Bloch. Nuclear induction. *Phys Rev*, 70:460–474, 1946.

[15] R.T. Born and D.C. Bradley. Structure and function of visual area MT. *Annu Rev Neurosci*, 28:157–189, 2005.

[16] G. Box and N. Draper. Empirical model building and response surfaces. *New York: John Wiley and Sons*, 1987.

[17] G. Brix, U. Lechel, G. Glatting, S.I. Ziegler, W. Münzing, S.P. Müller, and T. Beyer. Radiation exposure of patients undergoing whole-body dual-modality 18F-FDG PET/CT examinations. *J Nucl Med*, 46(4):608–613, 2005.

[18] R.B. Buxton, K. Uludağ, D.J. Dubowitz, and T.T. Liu. Modeling the hemodynamic response to brain activation. *Neuroimage*, 23(Suppl 1):220–233, 2004.

[19] R.B. Buxton, E.C. Wong, and L.R. Frank. Dynamics of blood flow and oxygenation changes during brain activation: The Balloon model. *Magn Reson Med*, 39(6):855–864, 1998.

[20] A.J. Cadotte, T.B. DeMarse, P. He, and M. Ding. Causal measures of structure and plasticity in simulated and living neural networks. *PLoS One*, 3(10):e3355, 2008.

[21] V.D. Calhoun, T. Eichele, and G. Pearlson. Functional brain networks in schizophrenia: a review. *Front Hum Neurosci*, 3(17):1–12, 2009.

[22] V.D. Calhoun, K.A. Kiehl, and G.D. Pearlson. Modulation of temporally coherent brain networks estimated using ICA at rest and during cognitive tasks. *Hum Brain Mapp*, 29(7):928–838, 2008.

[23] V.D. Calhoun, J. Liu, and T. Adali. A review of group ICA for fMRI data and ICA for joint inference of imaging, genetic, and ERP data. *Neuroimage*, 45(Suppl 1):163–172, 2009.

[24] P.T. Callaghan. Principles of nuclear magnetic resonance microscopy. *Oxford University Press*, 1991.

[25] J.-F. Cardoso and A. Souloumiac. Blind beamforming for non Gaussian signals. *IEEE Proc-F*, 140(6):362–370, 1993.

[26] J.-F. Cardoso and A. Souloumiac. Jacobi angles for simultaneous diagonalization. *SIAM J Mat Anal Appl*, 17(1):161–164, 1995.

[27] T.A. Carlson, P. Schrater, and S. He. Patterns of activity in the categorical representations of objects. *J Cogn Neurosci*, 15(5):704–717, 2003.

[28] J.A. Clithero, D.V. Smith, R.M. Carter, and S.A. Huettel. Within- and cross-participant classifiers reveal different neural coding of information. *Neuroimage*, page in press, 2010.

[29] D. Cohen. Magnetoencephalography: evidence of magnetic fields produced by alpha rhythm currents. *Science*, 161:784–786, 1968.

[30] A. Collignon, F. Maes, D. Delaere, D. Vandermeulen, P. Suetens, and G. Marchal. Automated multimodality image registration based on information theory. *Inf Process Med Imaging*, 36:263–274, 1995.

[31] P. Comon. Independent component analysis, a new concept? *Signal Process*, 36:287–314, 1994.

[32] J.W. Cooley and J.W. Tukey. An algorithm for the machine computation of the complex fourier series. *Math Comput*, 19:297–301, 1965.

[33] D.D. Cox and R.L. Savoy. Functional magnetic resonance imaging (fMRI) "brain reading": detecting and classifying distributed patterns of fMRI activity in human visual cortex. *Neuroimage*, 19(2):261–270, 2003.

[34] O. David, S.J. Kiebel, L.M. Harrison, J. Mattout, J.M. Kilner, and K.J. Friston. Dynamic causal modeling of evoked responses in EEG and MEG. *Neuroimage*, 30(4):1255–1272, 2006.

[35] M. Ding, Y. Chen, and S. Bressler. Granger causality: basic theory and application to neuroscience. *Handbook of time series analysis*, pages 438–460, 2006.

[36] P.A.M. Dirac. The quantum theory of the electron. *Proc R Soc Lond A*, 117:610–624, 1928.

[37] P. Duhamel and M. Vetterli. Fast fourier transforms: A tutorial review and a state of the art. *Signal Process*, 19:259–299, 1990.

[38] B. Efron. Bootstrap methods: Another look at the jackknife. *Ann Stat*, 7(1):1–26, 1979.

[39] P. Ehrenfest. Bemerkung über die angenäherte Gültigkeit der klassischen Mechanik innerhalb der Quantenmechanik. *Zeitschrift für Physik A*, 45(7-8):455–457, 1927.

[40] S.B. Eickhoff, S. Heim, K. Zilles, and K. Amunts. A systems perspective on the effective connectivity of overt speech production. *Philos Transact A Math Phys Eng Sci*, 367(1896):2399–2421, 2009.

[41] R.R. Ernst and W.A. Anderson. Application of fourier transform spectroscopy to magnetic resonance. *Rev Sci Instrum*, 37:93–102, 1966.

[42] D.C. Van Essen, J.H.R. Maunsell, and J.L. Bixby. The middle temporal visual area in the macaque: Myeloarchitecture, connections, functional properties and topographic organization. *J Comp Neurol*, 199(3):293–326, 1981.

[43] A.C. Evans, D.L. Collins, S.R. Mills, E.D. Brown, R.L. Kelly, and T.M. Peters. 3D statistical neuroanatomical models from 305 MRI volumes. *Proc IEEE-Nucl Sci Symp Med Imaging Conf*, 37:1813–1817, 1993.

[44] S.L. Fairhall and A. Ishai. Effective connectivity within the distributed cortical network for face perception. *Cereb Cortex*, 17(10):2400–2406, 2007.

[45] D.J. Felleman and D.C. Van Essen. Distributed hierarchical processing in the primate cerebral cortex. *Cereb Cortex*, 1(1):1–47, 1991.

[46] K.J. Friston. Functional and effective connectivity in neuroimaging: A synthesis. *Hum Brain Mapp*, 2(1-2):56–78, 1994.

[47] K.J. Friston. Modalities, modes, and models in functional neuroimaging. *Science*, 326(5951):399–403, 2009.

[48] K.J. Friston, C.D. Frith, P.F. Liddle, and R.S.J. Frackowiak. Functional connectivity: the principal-component analysis of large (PET) data sets. *J Cereb Blood Flow Metab*, 13(1):5–14, 1993.

[49] K.J. Friston, L.M. Harrison, and W.D. Penny. Dynamic causal modelling. *Neuroimage*, 19(4):1273–1302, 2003.

[50] K.J. Friston, A.P. Holmes, K.J. Worsley, J.-P. Poline, C.D. Frith, and R.S.J. Frackowiak. Statistical parametric maps in functional imaging: A general linear approach. *Hum Brain Mapp*, 2(4):189–210, 1995.

[51] W. Gerlach and O. Stern. Das magnetische Moment des Silberatoms. *Zeitschrift für Physik*, 9(1):353–355, 1922.

[52] C.W.J. Granger. Investigating causal relations by econometric models and cross-spectral methods. *Econometrica*, 37:424–438, 1969.

[53] C.W.J. Granger. Testing for causality: A personal viewpoint. *J Econ Dyn Control*, 2:329–352, 1980.

[54] S. Guo, A.K. Seth, K.M. Kendrick, C. Zhou, and J. Feng. Partial granger causality-eliminating exogenous inputs and latent variables. *J Neurosci Methods*, 172(1):79–93, 2008.

[55] E.M. Haacke, R.W. Brown, M.R. Thompson, and R. Venkatesan. Magnetic resonance imaging: principles and sequence design. *New York: Wiley-Liss*, 1999.

[56] C. Habas and E.A. Cabanis. Neural correlates of simple unimanual discrete and continuous movements: a functional imaging study at 3 T. *Neuroradiology*, 50(4):367–375, 2008.

[57] E.L. Hahn. Spin echoes. *Phys Rev*, 80:580–594, 1950.

[58] M. Hampson, B.S. Peterson, P. Skudlarski, J.C. Gatenby, and J.C. Gore. Detection of functional connectivity using temporal correlations in MR images. *Hum Brain Mapp*, 15(4):247–262, 2002.

[59] J.V. Haxby, M.I. Gobbini, M.L. Furey, A. Ishai, J.L. Schouten, and P. Pietrini. Distributed and overlapping representations of faces and objects in ventral temporal cortex. *Science*, 293(5539):2425–2430, 2001.

[60] J.D. Haynes and G. Rees. Predicting the orientation of invisible stimuli from activity in human primary visual cortex. *Nat Neurosci*, 8(5):686–691, 2005.

[61] J.D. Haynes and G. Rees. Predicting the stream of consciousness from activity in human visual cortex. *Curr Biol*, 15:1301–1307, 2005.

[62] J.D. Haynes and G. Rees. Decoding mental states from brain activity in humans. *Nat Rev Neurosci*, 7(7):523–534, 2006.

[63] J.D. Haynes, K. Sakai, G. Rees, S. Gilbert, C. Frith, and R.E. Passingham. Reading hidden intentions in the human brain. *Curr Biol*, 17(4):323–328, 2007.

[64] D.J. Heeger, A.C. Huk, W.S. Geisler, and D.G. Albrecht. Spikes versus BOLD: what does neuroimaging tell us about neuronal activity? *Nat Neurosci*, 3:631–633, 2000.

[65] D.J. Heeger and D. Ress. What does fMRI tell us about neuronal activity? *Nat Rev Neurosci*, 3(2):142–151, 2002.

[66] J. Hegdé and D.C. Van Essen. Selectivity for complex shapes in primate visual area V2. *J Neurosci*, 20(5):1–6, 2000.

[67] J. Hegdé and D.C. Van Essen. Temporal dynamics of shape analysis in macaque visual area V2. *J Neurophysiol*, 92(5):3030–3042, 2004.

[68] F.R. Helmert. Über die Bestimmung des wahrscheinlichen Fehlers aus einer endlichen Anzahl wahrer Beobachtungsfehler. *Z Math Phys*, 20:300–303, 1875.

[69] W.S. Hinshaw, P.A. Bottomley, and G.N. Holland. Radiographic thin-section image of the human wrist by nuclear magnetic resonance. *Z Phys*, 270(5639):722–723, 1977.

[70] J.D. Howard, J. Plailly, M. Grueschow, J.-D. Haynes, and J.A. Gottfried. Odor quality coding and categorization in human posterior piriform cortex. *Nat Neurosci*, 12(7):932–938, 2009.

[71] D.H. Hubel and T.N. Wiesel. Receptive fields and functional architecture of monkey striate cortex. *J Physiol*, 195(1), 1968.

[72] A.C. Huk, R.F. Dougherty, and D.J. Heeger. Retinotopy and functional subdivision of human areas MT and MST. *J Neurosci*, 22(16):7195–7205, 2002.

[73] A. Hyvärinen, J. Karhunen, and E. Oja. Independent component analysis. *John Wiley and Sons*, 2001.

[74] N.P. Issa, A. Rosenberg, and T.R. Husson. Models and measurements of functional maps in V1. *J Neurophysiol*, 99(6):2745–2754, 2008.

[75] R.J. Jaszczak and R.E. Coleman. Single photon emission computed tomography (SPECT). principles and instrumentation. *Invest Radiol*, 20(9):897–910, 1985.

[76] I.T. Jolliffe. Principal component analysis. *Springer Series in Statistics, New York*, 2002.

[77] Y. Kamitani and F. Tong. Decoding the visual and subjective contents of the human brain. *Nat Neurosci*, 8(5):679–685, 2005.

[78] E.R. Kandel, J.H. Schwartz, and T.M. Jessell. Principles of neural science. *McGraw-Hill, New York*, 4th ed., 2000.

[79] R.E. Kass and A.E. Raftery. Bayes factors and model uncertainty. *University of Washington*, Technical Report 254:http://www.stat.washington.edu/tech.reports/tr254.ps, 1993.

[80] R.E. Kass and A.E. Raftery. Bayes factors. *J Am Stat Assoc*, 90(430):773–795, 1995.

[81] M. Kocak, J.L. Ulmer, M. Sahin Ugurel, W. Gaggl, and R.W. Prost. Motor homunculus: passive mapping in healthy volunteers by using functional MR imaging initial results. *Radiology*, 251(2):485–492, 2009.

[82] H. Kolster, R. Peeters, and G.A. Orban. The retinotopic organization of the human middle temporal area MT/V5 and its cortical neighbors. *J Neurosci*, 30(29):9801–9820, 2010.

[83] A. Kumar, D. Welti, and R.R. Ernst. NMR Fourier zeugmatography. *J Magn Reson*, 18(1):69–83, 1975.

[84] K.K. Kwong, J.W. Belliveau, D.A. Chesler, I.E. Goldberg, R.M. Weisskoff, B.P. Poncelet, D.N. Kennedy, B.E. Hoppel, M.S. Cohen, R. Turner, H.-M. Cheng, T.J. Brady, and B.R. Rosen. Dynamic magnetic resonance imaging of human brain activity during primary sensory stimulation. *Proc Natl Acad Sci U S A*, 89(12):5675–5679, 1992.

[85] P.C. Lauterbur. Image formation by induced local interactions: Examples employing nuclear magnetic resonance. *Nature*, 242:190–191, 1973.

[86] P.C. Lauterbur. Magnetic resonance zeugmatography. *Pure Appl Chem*, 40:149–157, 1974.

[87] W.H. Lawton and E.A. Sylvestre. Self modeling curve resolution. *Technometrics*, 13(3):617–633, 1971.

[88] L. Lee, K.J. Friston, and B. Horwitz. Large-scale neural models and dynamic causal modeling. *Neuroimage*, 30(4):1243–1254, 2006.

[89] S.P. Lee, T.Q. Duong, G. Yang, C. Iadecola, and S.G. Kim. Relative changes of cerebral arterial and venous blood volumes during increased cerebral blood flow: implications for BOLD fMRI. *Magn Reson Med*, 45(5):791–800, 2001.

[90] J.W. Lewis and D.C. Van Essen. Corticocortical connections of visual, sensorimotor, and multimodal processing areas in the parietal lobe of the macaque monkey. *J Comp Neurol*, 357(1424):112–137, 2000.

[91] Y.-O. Li, T. Adali, and V.D. Calhoun. Estimating the number of independent components for functional magnetic resonance imaging data. *Hum Brain Mapp*, 28(11):1251–1266, 2007.

[92] B. Libet, E.W. Wright, JR.B. Feinstein, and D.K. Pearl. Subjective referral of the timing for a conscious sensory experience - a functional role for the somatosensory specific projection system in man. *Brain*, 102:193–224, 1979.

[93] N.K. Logothetis. The neural basis of the blood-oxygen-level-dependent functional magnetic resonance imaging signal. *Philos Trans R Soc Lond B Biol Sci*, 357(1424):1003–1037, 2002.

[94] N.K. Logothetis, J. Pauls, M. Augath, T. Trinath, and A. Oeltermann. Neurophysiological investigation of the basis of the fMRI signal. *Nature*, 412(6843):150–157, 2001.

[95] B.Z. Mahon and A. Caramazza. Judging semantic similarity: An event-related fMRI study with auditory word stimuli. *Neurosci*, 169(1):279–286, 2010.

[96] S. Mangia, F. Giove, I. Tkác, N.K. Logothetis, P.-G. Henry, C.A. Olman, B. Maraviglia, F.D. Salle, and Kamil Uğurbil. Metabolic and hemodynamic events following changes in neuronal activity: current hypotheses, theoretical predictions and in vivo NMR experimental findings. *J Cereb Blood Flow Metab*, 29(3):441–463, 2009.

[97] P. Mansfield. Multi-planar image formation using NMR spin echoes. *J Phys C: Sol State Phys*, 10(3):55–58, 1977.

[98] P. Mansfield and A.A. Maudsley. Planar spin imaging by NMR. *J Phys C: Sol State Phys*, 9(15):101–119, 1976.

[99] J.L. Marchini and B.D. Ripley. A new statistical approach to detecting significant activation in functional MRI. *Neuroimage*, 12(4):366–380, 2000.

[100] J.C. Mazziotta, A.W. Toga, A. Evans, P. Fox, and J. Lancaster. A probabilistic atlas of the human brain: Theory and rationale for its development : The international consortium for brain mapping (ICBM). *Neuroimage*, 2(2):89–101, 1995.

[101] D.J. McGonigle, A.M. Howseman, B.S. Athwal, K.J. Friston, R.S.J. Frackowiak, and A.P. Holmes. Variability in fMRI: An examination of intersession differences. *Neuroimage*, 11(6):708–734, 2000.

[102] A.R. McIntosh and F. Gonzalez-Lima. Structural equation modeling and its application to network analysis in functional brain imaging. *Hum Brain Mapp*, 2(1-2):2–22, 1994.

[103] M.J. McKeown, L.K. Hansen, and T.J. Sejnowsk. Independent component analysis of functional MRI: what is signal and what is noise? *Curr Opin Neurobiol*, 13(5):620–629, 2003.

[104] F.M. Miezin, L. Maccotta, J.M. Ollinger, S.E. Petersen, and R.L. Buckner. Characterizing the hemodynamic response: effects of presentation rate, sampling procedure, and the possibility of ordering brain activity based on relative timing. *Neuroimage*, 11(6):735–759, 2000.

[105] D. Milea, E. Lobel, S. Lehericy, C. Pierrot-Deseilligny, and A. Berthoz. Cortical mechanisms of saccade generation from execution to decision. *Ann N Y Acad Sci*, 1039:232–238, 2005.

[106] J.M. Miranda, A.L.W. Bokde, C. Born, H.H., and M. Stetter. Classifying brain states and determining the discriminating activation patterns: Support vector machine on functional MRI data. *Neuroimage*, 28(4):980–995, 2005.

[107] R. Moddemeijer. On estimation of entropy and mutual information of continuous distributions. *Signal Process*, 16(3):233–248, 1989.

[108] K.A. Norman, S.M. Polyn, G.J. Detre, and J.V. Haxby. Beyond mind-reading: multi-voxel pattern analysis of fMRI data. *Trends Cogn Sci*, 10(9):424–430, 2006.

[109] S. Ogawa, T.M. Lee, A.R. Kay, and D.W. Tank. Brain magnetic resonance imaging with contrast dependent on blood oxygenation. *Proc NatI Acad Sci U S A*, 87(24):9868–9872, 1990.

[110] S. Ogawa, T.M. Lee, A.S. Nayak, and P. Glynn. Oxygenation-sensitive contrast in magnetic resonance image of rodent brain at high magnetic fields. *Magn Reson Med*, 14(1):68–78, 1990.

[111] P. Paatero and U. Tapper. Positive matrix factorization: A non-negative factor model with optimal utilization of error estimates of data values. *Environmetrics*, 5(2):111–126, 1994.

[112] A. Papoulis. Probability, random variables, and stochastic processes. *New York: McGraw Hill*, 1984.

[113] M.A. Paradiso. A theory for the use of visual orientation information which exploits the columnar structure of striate cortex. *Biol Cybern*, 58(1):35–49, 1988.

[114] L.M. Parkes, J.B. Marsman, D.C. Oxley, J.Y. Goulermas, and S.M. Wuerger. Multivoxel fMRI analysis of color tuning in human primary visual cortex. *J Vis*, 9(1):1–13, 2009.

[115] W. Pauli. Zur Quantenmechanik des magnetischen Elektrons. *Z Phy A Hadr Nucl*, 43(9-10):601–623, 1927.

[116] W. Pauli and M. Fierz. Zur Theorie der Emission langwelliger Lichtquanten. *Il Nuovo Cimento*, 15(3):167–188, 1937.

[117] L. Pauling and C.D. Coryell. The magnetic properties and structure of hemoglobin, oxyhemoglobin and carbonmonoxyhemoglobin. *Proc Natl Acad Sci U S A*, 22(4):210–216, 1936.

[118] K. Pearson. On lines and planes of closest fit to systems of points in space. *Philos Mag*, 2(6):559–572, 1901.

[119] D.P. Pelvig, H. Pakkenberg, A.K. Stark, and B. Pakkenberg. Neocortical glial cell numbers in human brains. *Neurobiol Aging*, 29(11):1754–1762, 2008.

[120] W. Penfield and E. Boldrey. Somatic motor and sensory representation in the cerebral cortex of man as studied by electrical stimulation. *Brain*, 60:389–443, 1937.

[121] W.D. Penny, K.E. Stephan, A. Mechelli, and K.J. Friston. Comparing dynamic causal models. *Neuroimage*, 22(3):1157–1172, 2004.

[122] W.D. Penny, K.E. Stephan, A. Mechelli, and K.J. Friston. Modelling functional integration: a comparison of structural equation and dynamic causal models. *Neuroimage*, 23(1):264–274, 2004.

[123] C. Pierrot-Deseilligny, D. Milea, and R.M. Müri. Eye movement control by the cerebral cortex. *Curr Opin Neurol*, 17(1):17–25, 2004.

[124] A. Pouget, P. Dayan, and R. Zemel. Information processing with population codes. *Nat Rev Neurosci*, 1(2):125–132, 2000.

[125] V.V. Pravdich-Neminsky. Ein Versuch der Registrierung der elektrischen Gehirnerscheinungen. *Zbl Physiol*, 27:951–960, 1913.

[126] E.M. Purcell. Nuclear magnetism in relation to problems of the liquid and solid states. *Science*, 107(2783):433–440, 1948.

[127] Z. Qi, Xx Wu, Z. Wang, N. Zhang, H. Dong, L. Yao, and K. Li. Impairment and compensation coexist in amnestic MCI default mode network. *Neuroimage*, 50(1):48–55, 2010.

[128] I.I. Rabi, J.R. Zacharias, S. Millman, and P. Kusch. A new method of measuring nuclear magnetic moment. *Phys Rev*, 53:318–318, 1938.

[129] A.E. Raftery. Bayesian model selection in social research. *Sociol Methodol*, 25:111–163, 1995.

[130] N. Ramnani, T.E. Behrens, W.D. Penny, and P.M. Matthews. New approaches for exploring anatomical and functional connectivity in the human brain. *Biol Psychiatry*, 56(9):613–619, 2004.

[131] S.M. Rao, P.A. Bandettini, J.R. Binder, J.A. Bobholz, T.A. Hammeke, E.A. Stein, and J.S. Hyde. Relationship between finger movement rate and functional magnetic resonance signal change in human primary motor cortex. *J Cereb Blood Flow Metab*, 16:1250–1254, 1996.

[132] J. Rissanen. Stochastic complexity and the mdl principle. *Econ Rev*, 6(1):85–102, 1890.

[133] M. Rotte, M. Kanowski, and H.J. Heinze. Functional magnetic resonance imaging for the evaluation of the motor system: primary and secondary brain areas in different motor tasks. *Stereotact Funct Neurosurg*, 78(1):3–16, 2002.

[134] J.B. Rowe, H. Siebner, S.R. Filipovic, C. Cordivari, W. Gerschlager, J. Rothwell, and R. Frackowiak. Aging is associated with contrasting changes in local and distant cortical connectivity in the human motor system. *Neuroimage*, 32(2):747–760, 2006.

[135] C.S. Roy and C.S. Sherrington. On the regulation of the blood-supply of the brain. *J Physiol*, 11(1-2):85–108, 1890.

[136] Z.S. Saad, K.M. Ropella, R.W. Cox, and E.A. DeYoe. Analysis and use of fMRI response delays. *Hum Brain Mapp*, 13(2):74–93, 2001.

[137] R. Salvador, J. Suckling, C. Schwarzbauer, and E. Bullmore. Undirected graphs of frequency-dependent functional connectivity in whole brain networks. *Phil Trans R Soc B*, 360(1457):937–946, 2005.

[138] J.R. Sato, D.Y. Takahashi, S.M. Arcuri, K. Sameshima, P.A. Morettin, and L.A. Baccala. Frequency domain connectivity identification: An application of partial directed coherence in fMRI. *Hum Brain Mapp*, 30(2):452–461, 2009.

[139] T. Schanze. Sinc interpolation of discrete periodic signals. *IEEE Trans Signal Process*, 43(6):1502–1503, 1995.

[140] H. Scheffe. The analysis of variance. *New York: Wiley*, 1959.

[141] V. Schöpf, C.H. Kasess, R. Lanzenberger, F. Fischmeister, C. Windischberger, and E. Moser. Fully exploratory network ICA (FENICA) on resting-state fMRI data. *J Neurosci Methods*, 192(2), 2010.

[142] V. Schöpf, C. Windischberger, C.H. Kasess, R. Lanzenberger, and E. Moser. Group ICA of resting-state data: a comparison. *MAGMA*, in press, 2010.

[143] G. Schwarz. Estimating the dimension of a model. *Ann Stat*, 6(2):461–464, 1978.

[144] A.K. Seth. A matlab toolbox for Granger causal connectivity analysis. *J Neurosci Methods*, 2009.

[145] C.S. Soon, M. Brass, H.J. Heinze, and J.D. Haynes. Unconscious determinants of free decisions in the human brain. *Nat Neurosci*, 11(5):543–545, 2008.

[146] G.J. Stanisz, E.E Odrobina, J. Pun, M. Escaravage, S.J. Graham, and M.J. Bronskill R.M. Henkelman. T1, T2 relaxation and magnetization transfer in tissue at 3T. *Magn Reson Med*, 54(3):507–512, 2005.

[147] T. Starck, J. Remes, J. Nikkinen, O. Tervonen, and Vesa Kiviniemi. Correction of low-frequency physiological noise from the resting state BOLD fMRI-effect on ICA default mode analysis at 1.5 T. *J Neurosci Methods*, 186(2):179–185, 2010.

[148] D.D. Stark and W. Bradley. Magnetic resonance imaging. *St Louis, MO: Mosby*, 1999.

[149] K.E. Stephan, T. Baldeweg, and K.J. Friston. Synaptic plasticity and dysconnection in schizophrenia. *Biol Psychiatry*, 59(10):929–939, 2006.

[150] K.E. Stephan, J.C. Marshall, W.D. Penny, K.J. Friston, and G.R. Fink. Interhemispheric integration of visual processing during task-driven lateralization. *J Neurosci*, 27(13):3512–3522, 2007.

[151] K.E. Stephan and W.D. Penny. Dynamic causal models and bayesian selection. *Statistical parametric mapping: the analysis of functional brain images*, (Amsterdam: Elsevier.):577–585, 2006.

[152] K.E. Stephan, W.D. Penny, J. Daunizeau, R.J. Moran, and K.J. Friston. Bayesian model selection for group studies. *Neuroimage*, 46(4):1004–1017, 2009.

[153] K.E. Stephan, N. Weiskopf, P.M. Drysdale, P.A. Robinson, and K.J. Friston. Comparing hemodynamic models with DCM. *Neuroimage*, 38(3):387–401, 2007.

[154] C.M. Stinear, J.P. Coxon, and W.D. Byblow. Primary motor cortex and movement prevention: Where stop meets go. *Neurosci Biobehav Rev*, 33(5):662–673, 2009.

[155] J.V. Stone, J. Porrill, N.R. Porter, and I.D. Wilkinson. Spatiotemporal independent component analysis of event-related fMRI data using skewed probability density functions. *Neuroimage*, 15(2):407–421, 2002.

[156] C. Studholme, D.L.G. Hill, and D.J. Hawkes. An overlap invariant entropy measure of 3D medical image alignment. *Pattern Recognit*, 32(1):71–86, 1999.

[157] F.T. Sun, L.M. Miller, and M D'Esposito. Measuring interregional functional connectivity using coherence and partial coherence analyses of fMRI data. *Neuroimage*, 21(2):647–658, 2004.

[158] M.M. Ter-Pogossian, M.E. Phelps, E.J. Hoffman, and N.A. Mullani. Positron-emission transaxial tomograph for nuclear imaging (PET). *Radiology*, 114(1):89–98, 1975.

[159] F.J. Theis, P. Gruber, I.R. Keck, and E.W. Lang. A robust model for spatiotemporal dependencies. *Neurocomputing*, 71(10-12):2209–2216, 2008.

[160] K.R. Thulborn, J.C. Waterton, P.M. Matthews, and G.G. Radda. Oxygenation dependence of the transverse relaxation time of water protons in whole blood at high field. *Biochim Biophys Acta*, 714(2):165–270, 1982.

[161] F. Tong. Primary visual cortex and visual awareness. *Nat Rev Neurosci*, 4(3):219–229, 2003.

[162] R.B.H. Tootell, A.M. Dale, M.I. Sereno, and R. Malach. New images from human visual cortex. *Trends Neurosci*, 19(11):481–489, 1996.

[163] R.B.H. Tootell and J.B. Taylor. Anatomical evidence for MT and additional cortical visual areas in humans. *Cereb Cortex*, 5(1):39–55, 1995.

[164] A. Tosoni, G. Galati, G.L. Romani, and M. Corbetta. Sensory-motor mechanisms in human parietal cortex underlie arbitrary visual decisions. *Nat Neurosci*, 11(12):1446–1453, 2008.

[165] A. Tusche, S. Bode, and J.D. Haynes. Neural responses to unattended products predict later consumer choices. *J Neurosci*, 30(23):8024–8031, 2010.

[166] W. Vanduffel, R.B.H. Tootell, A.A. Schoups, and G.A. Orban. The organization of orientation selectivity throughout macaque visual cortex. *Cereb Cortex*, 12(6):647–662, 2002.

[167] G. Varoquaux, S. Sadaghiani, P. Pinel, A. Kleinschmidt, J.B. Poline, and B. Thirion. A group model for stable multi-subject ICA on fMRI datasets. *Neuroimage*, 51(1):288–299, 2010.

[168] O. Yamashita, N. Sadato, T. Okada, and T. Ozaki. Evaluating frequency-wise directed connectivity of BOLD signals applying relative power contribution with the linear multivariate time-series models. *Neuroimage*, 25(2):478–490, 2005.

[169] B.B. Zandbelt, T.E. Gladwin, M. Raemaekers, and M. van Buuren. Within-subject variation in BOLD-fMRI signal changes across repeated measurements: Quantification and implications for sample size. *Neuroimage*, 42(1):196–206, 2008.

[170] S.M. Zeki. Functional organization of a visual area in the posterior bank of the superior temporal sulcus of the rhesus monkey. *J Physiol*, 236(3):549–573, 1974.

[171] Z. Zhang, G. Lu, Y. Zhong, Q. Tan, Z. Yang, W. Liao, Z. Chen, J. Shi, and Y. Liu. Impaired attention network in temporal lobe epilepsy: A resting fMRI study. *Neurosci Lett*, 458(3), 2009.

[172] Y. Zhong, H. Wang, G. Lu, Z. Zhang, Q. Jiao, and Y. Liu. Detecting functional connectivity in fMRI using PCA and regression analysis. *Brain Topogr*, 22(2):134–144, 2009.